

Negative Linear Compressibility:
Beyond the Wine-Rack Model and Towards Engineering Applications

Submitted by David Lewis Barnes to the University of Exeter
as a thesis for the degree of
Doctor of Philosophy in Engineering
In February 2017

This thesis is available for Library use on the understanding that it is copyright material and that no quotation from the thesis may be published without proper acknowledgement.

I certify that all material in this thesis which is not my own work has been identified and that no material has previously been submitted and approved for the award of a degree by this or any other University.

Signature:

Abstract

Negative Linear Compressibility (NLC), where a material expands in a given direction when subjected to hydrostatic compression, is a rare elastic property that has received much attention recently, but has yet to be used in practical applications. What are the mechanisms responsible for this property in crystals and man-made structures? Are all mechanisms somehow related to the wine-rack model? Can we find an even simpler and more fundamental elucidation of NLC? Following this mechanistic approach, can we then identify “engineering” materials with NLC? To answer these questions, I have used a combination of analytical modelling based on beam theory and finite element analysis, to investigate several structures. At first, I examine in great detail the standard wine-rack in 2D and equivalents in 3D and identify the aspect ratio (close to two) at which NLC is maximum. By adding spacers I demonstrate that a cross is not a necessary condition, and that simpler angle changes in chains are sufficient to generate NLC. Looking for materials with intersecting straight chains, “zig-zag” chains or quasi-helical structures, I find that carbon fibre mats, some extruded polymers and some woods exhibit NLC. Finally, I show that elliptical voids in 2D sheets can also generate NLC in a way related to the wine-rack.

This thesis improves the understanding of the mechanism(s) responsible for NLC by proving that a wine-rack is not necessary. Perhaps more importantly it suggests that the property can be exploited in several relatively common materials.

Contents

Chapter 1	Introduction	1
Chapter 2	Background and Literature Review	4
2.1	Introduction	4
2.2	Definitions and Elasticity Theory	5
2.2.1	Compressibility Definitions	5
2.2.2	Tensor Form of Linear Compressibility	6
2.2.3	Negative values of Linear Compressibility	6
2.2.4	Compressibility from Elastic Constants.....	7
2.2.5	Normalised Linear Compressibility	9
2.2.6	Compressibility Capacity	10
2.2.7	Coincident Occurrence of NLC and Stretch Densification	10
2.3	NLC Materials Research	11
2.3.1	Introduction	11
2.3.2	Biological Systems.....	12
2.3.3	Macro Structures	13
2.3.4	Crystalline Systems	15
2.4	Negative Poisson’s Ratio Research	23
2.4.1	Introduction	23
2.4.2	Description of Negative Poisson’s Ratio	24
2.4.3	Negative Poisson’s Ratio Materials and Mechanisms	25
2.4.4	Favourable Properties and Applications	27
2.5	Conclusions	30
Chapter 3	Two-Dimensional “wine-rack” Structures and Newly Identified NLC materials.....	32
3.1	Introduction	32
3.1.1	Background	32
3.1.2	Scope.....	32
3.2	Modelling Assumptions.....	33
3.3	Two-Dimensional Elastic Symmetries	33
3.3.1	Preamble	33
3.3.2	Square	34
3.3.3	Rectangular	34
3.4	Modelled Structure and Input Parameters.....	35
3.5	Analytical Modelling of 2D Type II Beam Structure	36

3.5.1	Introduction	36
3.5.2	Analytical Derivation	37
3.5.3	Results	41
3.6	Finite Element Modelling of 2D Type II Beam Structure.....	46
3.6.1	Preamble	46
3.6.2	Methodology.....	46
3.6.3	Results.....	48
3.7	Conclusions from analysis of 2D “wine-rack”	49
3.8	NLC in Common Engineering Materials	50
3.8.1	Introduction	50
3.8.2	Guidance for Identifying NLC materials	50
3.8.3	Materials Identified.....	51
3.8.4	Conclusions	57
Chapter 4	Three-Dimensional NLC Structures	58
4.1	Introduction	58
4.2	Symmetries Explored	58
4.3	Methodology.....	59
4.4	Tetragonal Structures	59
4.4.1	Lattice Parameters and Compliance Matrix.....	59
4.4.2	Unit-Cell	60
4.4.3	Results.....	62
4.5	Orthorhombic Structures.....	67
4.5.1	Lattice Parameters and Compliance Matrix.....	67
4.5.2	Unit-Cell	68
4.5.3	Results.....	69
4.6	Conclusions	71
Chapter 5	“Spaced” Two- and Three-Dimensional Structures	72
5.1	Introduction	72
5.2	Addition of “Spacers”	72
5.2.1	Preamble	72
5.2.2	Two-Dimensional Rectangular	72
5.2.3	Three-Dimensional Tetragonal	76
5.3	Conclusions	81
Chapter 6	Large Strain Effects in 2D Structures.....	82

6.1	Introduction	82
6.2	2D Hinging Model	83
6.2.1	Modelling	83
6.2.2	Results	84
6.3	2D Beam Flexure Model.....	85
6.3.1	Preamble	85
6.3.2	Modelling	86
6.3.3	Results.....	87
6.4	Results Summary.....	91
6.5	Conclusions and Further Work.....	94
Chapter 7	Elliptical Voids	95
7.1	Introduction	95
7.2	Methodology.....	96
7.2.1	Calculation of Linear Compressibility.....	96
7.2.2	FE Methodology	96
7.3	Analysis	98
7.3.1	Increasing Ellipse Aspect Ratio.....	98
7.3.2	Alternative Arrangement of Elliptical Voids.....	101
7.4	Conclusions	104
Chapter 8	Conclusions	106
8.1	Introduction	106
8.2	Key Findings	106
8.2.1	NLC Mechanisms.....	106
8.2.2	Engineering Materials	107
8.3	Further Work.....	108
8.3.1	NLC Mechanisms.....	108
8.3.2	Engineering Materials	108
8.4	Applications.....	109
Appendix A	Derivation of Analytical Formulae for 2D Beam Structure with Spacer	110
Appendix B	Derivation of Analytical Formulae for 3D Beam Structure	112
B1	Introduction	112
B2	Derivation.....	112
B3	Spacer Modification	116
Appendix C	Method for Calculating Linear Compressibility in Orthorhombic Networks	118

C1	Introduction	118
C2	Analytical Methodology	118
C2.1	Preamble	118
C2.2	Derivation.....	118
Appendix D Current NLC materials.....		123
Bibliography		126

List of Figures

Figure 2.1	Illustration of (a) conventional material, (b) material with NAC and (c) material with NLC. Blue represents the undeformed material and green represents the deformed material.	6
Figure 2.2	Representation of Baughman’s “wine-rack” mechanism shown in (a) the unloaded state and (b) the loaded state	13
Figure 2.3	Schematic of the unit-cell reported to produce NVC when submitted to a penetrating hydrostatic pressure (Gatt and Grima, 2008).....	14
Figure 2.4	Atomic structure of CsH_2PO_4 (Praver et al., 1985)	17
Figure 2.5	Representations of: (a) a generic helical chain structure lengthening under hydrostatic load; and (b) the crystallographic wireframe of trigonal selenium.....	18
Figure 2.6	“Spring-and-gear NLC mechanism” (a) Projection along the c axis of the $\text{YFe}(\text{CN})_6$ structure, showing the distortion of the structure under pressure. This twisting of the rigid gear-like $\text{Fe}(\text{CN})_6$ units is accompanied by rotation of the torsional spring-like YNO units. Y atoms are shown in green, Fe in orange, C in black and N in blue.....	20
Figure 2.7	NLC mechanism within UTSA-16 (Binns et al., 2016)	22
Figure 2.8	Conventional and re-entrant honeycomb structures	25
Figure 2.9	Representation of the auxetic mechanism in drawn PTFE.....	26
Figure 2.10	Bending response of: (a) a non-auxetic honeycomb; and (b) an auxetic honeycomb (Lakes and Witt, 2002).....	28
Figure 2.11	The response of (a) non-auxetic and (b) auxetic materials to localised indentation (Alderson, 1999)	29
Figure 3.1	Repeatable unit-cell of rectangular symmetry with suggested beam types labelled.....	35
Figure 3.2	Repeatable unit-cell of the two-dimensional type II beam structure (dashed lines represent the boundary of the unit-cell and solid lines denote the beams)	36
Figure 3.3	Type II primitive unit-cell and boundary conditions where the nodes have been labelled	36
Figure 3.4	Repeatable (a) and primitive (b) unit-cells of the two-dimensional type II beam structure	37
Figure 3.5	Illustration of pressure loading on (a) bulk material, (b) primitive unit-cell and (c) resulting forces on primitive unit-cell	38
Figure 3.6	Type II primitive unit-cell, boundary conditions and node labels.....	38
Figure 3.7	Forces resolved to local beam axes.....	39
Figure 3.8	Illustration of (a) axial and (b) transverse deflections.....	40
Figure 3.9	Deflection resolved to global coordinate system.....	40
Figure 3.10	Absolute linear compressibility, in the x and y directions, of the two-dimensional type II beam structure	42
Figure 3.11	Absolute linear compressibility, in the x and y directions, of the two-dimensional type II beam structure (vertical scale modified to assist reading of negative values)	43
Figure 3.12	Minimum normalised linear compressibility in a two-dimensional type II beam structure	44
Figure 3.13	Minimum absolute linear compressibility of a type II beam structure in a rectangular symmetry for different values of L/r where $\theta = 25.9^\circ$	45
Figure 3.14	Illustration of boundary conditions used in FE modelling of beam structures	46

Figure 3.15	Sensitivity of the calculated elastic compliances and linear compressibility to mesh density of a two-dimensional type II beam model where $\theta = 15^\circ$	47
Figure 3.16	Elastic compliances of the two-dimensional type II beam structure for different values of θ	48
Figure 3.17	NLC visualised by rotation of a rigid beam as a (a) single unit-cell, and a (b) 3×3 array	49
Figure 3.18	Elastic compliance and calculated linear compressibility of drawn polyethylene for different values of draw ratio (data from Chan et al., 1978)	52
Figure 3.19	Linear compressibility of CFRP panels of varying layer alignment calculated using plate program	53
Figure 3.20	Section diagram illustrating the structure of hardwood (Clifford, 2016).....	55
Figure 4.1	Tetragonal lattice parameters.....	59
Figure 4.2	Type I beam arrangement within a tetragonal symmetry	61
Figure 4.3	Type II beam arrangement within a tetragonal symmetry	61
Figure 4.4	Type III beam arrangement within a tetragonal symmetry	61
Figure 4.5	Repeatable (a) and primitive (b and c) unit-cells for a 3D tetragonal beam structure	62
Figure 4.6	Absolute linear compressibility for a type III beam structure in a tetragonal symmetry	64
Figure 4.7	Absolute linear compressibility for a type III beam structure in a tetragonal symmetry (vertical scale modified to assist reading of negative values).....	64
Figure 4.8	Absolute linear compressibility for a type III beam structure in a tetragonal symmetry (vertical scale modified to assist reading of negative values and the horizontal axis changed to show the aspect ratio of the unit-cell)	65
Figure 4.9	Direction of NLC in a tetragonal beam structure for unit-cell aspect ratios below 1 (left) and above 1 (right)	66
Figure 4.10	Minimum normalised linear compressibility of a type III beam structure in a tetragonal symmetry.....	67
Figure 4.11	Orthorhombic lattice parameters	67
Figure 4.12	(a) Type III beam arrangement in an orthorhombic symmetry (repeatable unit-cell) (b) Type III beam arrangement in an orthorhombic symmetry (primitive unit-cell) (c) Primitive unit-cell showing the angle θ as a projection of the beam on to the zx plane.....	69
Figure 4.13	Minimum absolute linear compressibility of a type III beam structure in orthorhombic symmetry. (a)Surface plot of minimum absolute linear compressibility as a function of θ and α . (b)Line plot of minimum absolute linear compressibility for a type III beam structure in a tetragonal symmetry where θ is varied and $\alpha = 45^\circ$. Note: both plots include a contour plot to aid visualisation where magnitudes are denoted by shades of blue (low) to red (high).....	70
Figure 4.14	Minimum normalised linear compressibility of a type III beam structure in an orthorhombic symmetry. (a)Surface plot of minimum normalised linear compressibility as a function of θ and α . (b)Line plot of minimum normalised linear compressibility for a type III beam structure in a tetragonal symmetry where θ is varied and $\alpha = 45^\circ$	71
Figure 5.1	Repeatable (a) and primitive (b) unit-cells for the two-dimensional rectangular model with inclusion of spacer.....	73
Figure 5.2	Minimum absolute linear compressibilities of a type II beam structure in a rectangular symmetry with spacers of differing lengths.....	74

Figure 5.3	(a)Unit-cell parameters of spaced rectangular structure without spacer (b)Unit-cell parameters of spaced rectangular structure with spacer	74
Figure 5.4	(a)-(d) Plots of terms 1-4, respectively, from Equations 5.1-5.2 for different values of γ_A (e) β_x plotted using Equation A1 for different values of γ_A	75
Figure 5.5	Minimum normalised linear compressibilities of a type II beam structure in a rectangular symmetry with spacers of differing lengths.	76
Figure 5.6	(a) Repeatable unit-cell of type III beam structure with spacer in a tetragonal symmetry (b) Primitive unit-cell of type III beam structure with spacer in a tetragonal symmetry. 77	
Figure 5.7	Minimum absolute linear compressibility of a type III beam structure in a tetragonal symmetry for three different values of γ_C	78
Figure 5.8	Minimum normalised linear compressibility of a type III beam structure in a tetragonal symmetry for three different values of γ_C	78
Figure 5.9	Minimum normalised linear compressibility of a type III beam structure in a tetragonal symmetry plotted against the aspect ratio of the unit-cell for three different values of γ_C	79
Figure 5.10	Minimum absolute linear compressibility of a type III beam structure in a tetragonal symmetry for three different values of γ_A	80
Figure 5.11	Minimum normalised linear compressibility of a type III beam structure in a tetragonal symmetry for three different values of γ_A	80
Figure 6.1	Hinging deformation of cross and spaced-cross structures	83
Figure 6.2	(a) Minimum linear compressibility of the hinging cross and spaced-cross structures plotted against strain on the x-axis arising from hydrostatic pressure (b) Maximum linear compressibility of the hinging cross and spaced-cross structures plotted against strain on the x-axis arising from hydrostatic pressure (c) Minimum normalised linear compressibility of the hinging cross and spaced-cross structures plotted against strain on the x-axis arising from hydrostatic pressure	85
Figure 6.3	Flexing deformation of cross and spaced-cross structures.....	86
Figure 6.4	(a) Minimum linear compressibility of the cross structure using FE beam modelling where different plots are shown for different values of θ_0 (b) Maximum linear compressibility of the cross structure using FE beam modelling where different plots are shown for different values of θ_0 (c) Minimum normalised linear compressibility of the cross structure using FE beam modelling where different plots are shown for different values of θ_0	88
Figure 6.5	Initial and deformed cross geometry of a single repeatable unit-cell where $\theta_0 = 40^\circ$...	88
Figure 6.6	(a) Hinging cross where β_x is a minimum ($\theta = 26^\circ$) (b) Beam flexure model where β_x is a minimum (equivalent internal angle is 32° based on unit-cell aspect ratio) and the initial internal angle is 40°	89
Figure 6.7	Final displaced geometry of cross configuration where $\theta_0 = 40^\circ$	89
Figure 6.8	(a) Minimum linear compressibility of the spaced-cross structure using FE beam modelling where different plots are shown for different values of θ_0 (b) Maximum linear compressibility of the spaced-cross structure using FE beam modelling where different plots are shown for different values of θ_0 (c) Minimum normalised linear compressibility of the spaced-cross structure using FE beam modelling where different plots are shown for different values of θ_0	90

Figure 6.9	Initial and deformed spaced-cross geometry of a single repeatable unit-cell where $\theta_0 = 50^\circ$	91
Figure 6.10	Comparison of results using the derived analytical formulae and FEA for the cross model where $\theta_0 = 40^\circ$. (a) minimum linear compressibility (b) maximum linear compressibility (c) minimum normalised linear compressibility.....	92
Figure 6.11	Comparison of results using the derived analytical formulae and FEA for the spaced-cross model where $\theta_0 = 50^\circ$. (a) minimum linear compressibility (b) maximum linear compressibility (c) minimum normalised linear compressibility	93
Figure 7.1	Lengthening of a hollow ellipse under hydrostatic pressure	95
Figure 7.2	Boundary conditions applied to all models for (a) strain applied in the x direction, and (b) strain applied in the y direction.....	97
Figure 7.3	Boundary conditions applied to 5×5 unit-cell model for (a) strain applied in the x direction, and (b) strain applied in the y direction.....	97
Figure 7.4	Layout of the model used to alter the ellipse aspect ratio	98
Figure 7.5	Meshes used in convergence study for regularly arranged elliptical voids; (a) 95 elements, (b) 905 elements and (c) 2250 elements.....	99
Figure 7.6	Sensitivity of the calculated elastic compliance and linear compressibility to mesh density where ellipse aspect ratio is 6.25	99
Figure 7.7	Elastic compliance and minimum linear compressibility for increasing elliptical void aspect ratio.....	100
Figure 7.8	Von Mises (a) and σ_{yy} (b) stress contour plots showing four unit-cells of uniformly packed elliptical voids with an aspect ratio of 4 where a strain in the x direction has been applied.....	101
Figure 7.9	Hexagonally arranged elliptical voids.....	101
Figure 7.10	Plot of hexagon fitted to ellipse	102
Figure 7.11	Patterned elliptical void (void-ratio = 0.750)	102
Figure 7.12	Examples of meshes used in convergence study for hexagonally arranged elliptical voids; (a) 408 elements, (b) 960 elements and (c) 2664 elements.....	103
Figure 7.13	Sensitivity of the calculated elastic compliances and linear compressibility to mesh density where an ellipse aspect ratio is 6.25 is applied and the hexagonal spacing is a minimum	103
Figure 7.14	Elastic compliance and linear compressibility for various void ratios. S_{22} is plotted in (a) and has been removed in (b) to aid visualisation of the other values.	104
Figure A1	Repeatable (a) and primitive (b) unit-cells for a 2D rectangular cross structure with spacer	110
Figure B1	Repeatable (a) and primitive (b) unit-cells for 3D tetragonal structure	112
Figure B2	(a) Pressure loading on primitive unit-cell (a) Resulting forces acting on primitive unit-cell	113
Figure B3	(a) Orthographic illustration of forces acting on beam (b) Illustration of forces acting on beam in plane indicated in (a).....	114
Figure B4	Repeatable (a) and primitive (b) unit-cells of 3D tetragonal beam model with spacer	116

Figure C1	Repeatable (a) and primitive (b) unit-cells for a type III beam structure arranged within an orthorhombic symmetry	119
Figure C2	Beam loading and forces resolved to local beam axes	120

Chapter 1

Introduction

At first glance, negative linear compressibility (NLC) is a distinctly odd property. Those rare materials or structures that exhibit it expand in some, but not all directions when subjected to hydrostatic pressure: how unusual! However, on closer inspection, this behaviour becomes less surprising, especially when considering the canonical “wine-rack” mechanism where compliant hinges easily accommodate compression in one direction and expansion in another (Baughman et al., 1998a).

Although this is not immediately apparent, NLC is equivalent to stretch densification, where a material or structure becomes denser when subjected to a tensile load in the elastic regime (which is unusual, as conventional isotropic materials with a Poisson’s ratio of around 0.3 actually become less dense when elastically stretched). Stretch densification has been exploited in a few niche applications, for instance, cable grippers or surgical finger pullers, but to the best of my knowledge, NLC per se has not been applied yet.

The earliest known reference to NLC dates from 1922, in an experimental study of the trigonal crystal of tellurium by Bridgman (Bridgman, 1922). In 1932, Bridgman also observed NLC in arsenic (Bridgman, 1933). The property was not completely ignored, and Nye mentions in passing that tellurium exhibits it in his popular book “Physical Properties of Crystals” (Nye, 1964), but nothing much seems to have happened around it until it was picked again by Baughman in an article published in *Science* in 1998 (Baughman et al., 1998a). To some extent NLC remained rather obscure, and definitely in the shadow of its more famous cousin negative Poisson’s ratio (NPR). Things changed dramatically when NLC was observed by Goodwin in $\text{Ag}_3[\text{Co}(\text{CN})_6]$ (Prussian blue) (Goodwin et al., 2008), which led to a string of articles published in prestigious journals, often with amusing titles featuring increasingly ambitious adjectives such as “large”, “giant”, and my personal favourite “colossal”!

This PhD forms part of EPSRC grant No. EP/ G064601/1 “Modelling Negative Linear Compressibility: from crystals to scaffolds”. The objectives of the project were to improve the understanding of the mechanisms that cause NLC and to identify additional materials and structures/frameworks with NLC, as well as to explore applications. The specific aims of my PhD research were to carry out a bibliographic meta-analysis of published elastic data to discover crystals and materials with NLC, and to investigate NLC in macroscopic frameworks, using a mixture of analytical modelling and finite element analysis (FEA). In addition, I was particularly interested in finding NLC materials that could be produced in large enough quantities for real applications.

The thesis is organised as follows: Chapter 2 starts with a brief outline of the principles and notations of elasticity theory and I then review the existing literature on NLC. I have omitted a “Methodology” chapter as, for thematically linked chapters, it made more sense to introduce methodological considerations where appropriate. Chapter 3 considers NLC in structures made up of intersecting beams within a 2D plane. The conclusions made from this study are then used to guide the search for common NLC materials and a number of common engineering materials are shown to have NLC.

Chapter 3 and 4 then document additional studies relating to similar structures and in particular look at 3D “wine-racks” and what happens when a “spacer” is added to the structure. The tools used in these three chapters are a combination of analytical modelling based on beam theory and simulations with FEA. Some of the work reported in these chapters regarding NLC in two- and three-dimensional frameworks has been published in 2012 in “Mechanics of Materials” and has been cited 27 times as of December 2016 (Barnes et al., 2012). Chapter 6 documents further investigations into some of the structures considered in Chapter 3-5. Specifically their behaviour, when large strains are applied, is analysed. This analysis is used to determine the strain-dependant linear compressibility and is also used to predict the total strain the material can exhibit along NLC axes. A new method of instigating NLC within any parent material by patterning it with elliptical features (in this case voids) is presented in

Chapter 7. Finally, Chapter 8 concludes this study with a synopsis of the key findings presented in this thesis and suggestions for further work are recommended.

Chapter 2

Background and Literature Review

2.1 Introduction

This review begins by defining what elastic compressibility is, how it is represented in tensor form and what negative compressibility means. NLC is then expressed in terms of isotropic elastic constants and the method used to determine NLC from elastic compliances (that describe anisotropic materials) is shown. These expressions show that NLC and similarly, negative area compressibility (NAC), are a theoretical possibility. Two additional quantities are then discussed; the normalised linear compressibility and the compressibility capacity. These quantities provide additional information to help describe the “overall” NLC effect.

The materials currently known to exhibit NLC are reported in Section 2.3 which comprises a number of sub-sections; biological systems, macro structures and crystalline systems. The crystalline systems sub-section includes further sub-divisions to distinguish between NLC manifested via a phase change and NLC caused directly by the elastic properties of the framework. In addition, due to the large number of articles published on the subject, a sub-section has been dedicated to metal-organic-frameworks (MOFs) that exhibit NLC. Importantly, efforts have been made to highlight the method used in each reported case to help judge the validity of the reported data and to help conclude whether further substantiation would be required.

Due to the relative infancy of NLC research, this chapter also provides a brief review of the scholarship relevant to a similarly bizarre subset of materials, those with a negative Poisson’s ratio (auxetic materials). Auxetic material research is in a far more advanced state than that of NLC research and many more efforts have been made to develop mechanisms that can be exploited in the production of engineering applications. Knowledge of these

mechanisms should therefore be used to help direct future efforts of NLC research. Auxetic behaviour is defined in Section 2.5 and a number of fabricated auxetic materials are discussed. A selection of the analytical methods used to model auxetic behaviour are then reviewed and the impact this abnormal property has on other material properties is reported alongside a number of suggested applications.

2.2 Definitions and Elasticity Theory

2.2.1 Compressibility Definitions

In order to be consistent with the convention adopted by the current literature, the term “hydrostatic pressure” is used throughout this thesis to define a pressure that is exerted equally across the three orthogonal directions. This type of pressure is sometimes referred to as “isotropic pressure” in more engineering biased fields of study although the former term shall be used here. The linear compressibility of a material, β_L , is defined as the unit change in length along a given axis as a consequence of a change in hydrostatic pressure, ΔP . Similarly, β_A and β_V , the area and volume compressibilities respectively, denote the change in area across a given plane and the change in volume as a result of a change in hydrostatic pressure (Baughman et al., 1998a). These constants are defined symbolically as,

$$\frac{\Delta L}{L_0} = \beta_L \Delta P \quad 2.1$$

$$\frac{\Delta A}{A_0} = \beta_A \Delta P \quad 2.2$$

and

$$\frac{\Delta V}{V_0} = \beta_V \Delta P \quad 2.3$$

where L_0 , A_0 and V_0 represent the initial length, area and volume respectively, ΔL , ΔA and ΔV represent the change in length, area and volume respectively and ΔP denotes the change in hydrostatic pressure. Typical values of volume compressibility can range from $\sim 15 \text{TPa}^{-1}$ for steel to $\sim 300 \text{TPa}^{-1}$ for more compliant materials like polystyrene. As the linear and area compressibilities are dependent upon the axis or plane on which they are being

measured/calculated, a large range of values can be reported within a single material. For this reason, maximum and minimum values of these constants are often presented.

2.2.2 Tensor Form of Linear Compressibility

Nye (Nye, 1964) describes compressibility as a second rank tensor as

$$\boldsymbol{\beta} = \frac{\partial}{\partial p} \begin{bmatrix} \varepsilon_{11} & \varepsilon_{12} & \varepsilon_{13} \\ \varepsilon_{21} & \varepsilon_{22} & \varepsilon_{23} \\ \varepsilon_{31} & \varepsilon_{32} & \varepsilon_{33} \end{bmatrix} \quad 2.4$$

where, ε_{ij} , denotes the strain experienced by the face perpendicular to the i -axis and in the direction of the j -axis. These strains are a function of the partial differential of the hydrostatic pressure $\frac{\partial}{\partial p}$. The three eigenvalues of this matrix represent the three principal compressibilities of the system and can therefore describe the compressibility of the material. Should any one of the principal values be negative, the material described will exhibit NLC.

2.2.3 Negative values of Linear Compressibility

A negative value of linear or area compressibility indicate that the material will expand on a given axis or across a given plane when there is an increase in the applied hydrostatic pressure (see Figure 2.1).

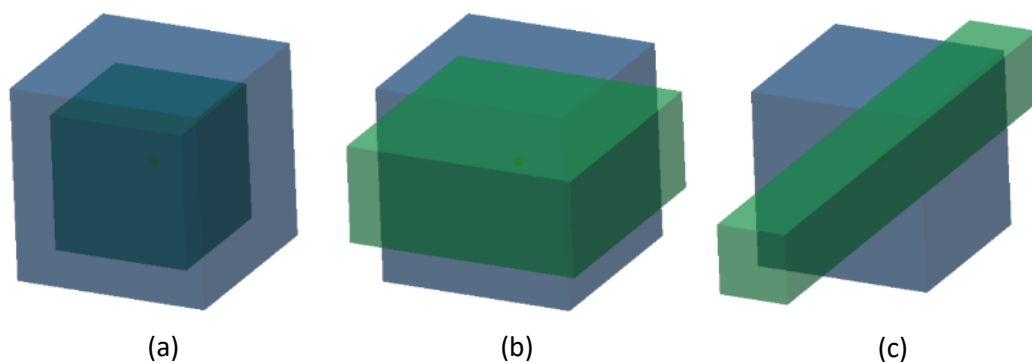


Figure 2.1 Illustration of (a) conventional material, (b) material with NAC and (c) material with NLC. Blue represents the undeformed material and green represents the deformed material.

Negative values of linear and area compressibility are known to be thermodynamically possible in purely elastic phases. It is not possible for a negative volume compressibility (NVC) to exist in a purely elastic phase and values of volume compressibility are predictably confined to positive values (Nye, 1964). Some evidence shows the existence of negative volume stiffness in some foams manufactured using specialist techniques, where the expansion is initiated by the elastic instability of the foam ribs (Lakes and Drugan, 2002). It should be noted that, as this is a high strain effect, the laws of thermodynamics are not violated. Furthermore, a specific arrangement of bi-material beams has been theorised that could produce a negative volume compressibility (NVC) (Gatt et al., 2009). The findings in this study are technically possible as the hydrostatic pressure applied is penetrative i.e. is exerted upon all exterior and interior faces and is therefore not a true hydrostatic pressure as defined by Nye (Nye, 1964).

The first reference to NLC in the literature was almost a century ago when tellurium was first found to exhibit the property (Bridgman, 1922). The compressibility of a number of materials was measured at high pressures and it was reported that tellurium, which atomically, is composed of a helical-like chain structure, had NLC. At this early stage, little was known of the abnormal property and the authors proposed, incorrectly, that the property was linked to a negative Poisson's ratio. The first modern review paper published on the subject of NLC identified 13 crystalline materials that exhibited the property (Baughman et al., 1998a) and is responsible for the subsequent interest in the subject on which numerous papers have now been published.

2.2.4 Compressibility from Elastic Constants

2.2.4.1 Compressibility calculated from Isotropic and Anisotropic Elastic Properties

The volume compressibility of an isotropic material can be calculated from the Poisson's ratio, ν , and Young's Modulus, E , using

$$\beta_V = \frac{3(1 - 2\nu)}{E} \quad 2.5$$

The area and linear compressibilities of that material are calculated as $\beta_A = \frac{2\beta_V}{3}$ and $\beta_L = \frac{\beta_V}{3}$ respectively although isotropic materials cannot have NLC. The behaviour of anisotropic materials cannot be defined as easily, and it is only possible to derive the compressibility properties by analysing the stiffness or compliance tensor of the material in question (Nye, 1985). The established method of using Voigt notation to form a 6×6 matrix of elastic compliances is adopted throughout this thesis to aid visualisation. The maximum number of independent constants used to define a material is 21, where only 15 of these can affect the linear compressibility as compliances relating to shear are not required. Hence for materials with low symmetry, the compressibility can vary greatly across the three orthogonal directions.

2.2.4.2 Two-dimensional Elastic Compliance Matrix

NLC can be calculated using the compliance matrix of the material. In a simplified two-dimensional system, there is a maximum of 6 unique elastic compliances as follows;

$$\begin{bmatrix} S_{11} & S_{12} & S_{13} \\ S_{12} & S_{22} & S_{23} \\ S_{13} & S_{23} & S_{33} \end{bmatrix} \quad 2.6$$

Noting that Voigt notation is being used, in this two-dimensional case S_{33} has become the shear term referring to S_{1212} in tensor notation. When considering this two-dimensional system, linear compressibility on a given axis can be calculated by summing the components of the relevant elastic compliances that act on the given axis,

$$\beta_L = S_{11} + S_{12} - (S_{11} - S_{22})L_y + S_{23}L_yL_x \quad 2.7$$

where L_y and L_x are the components of a unit vector aligned to the axis of interest. From this equation, it is possible to determine the linear compressibility in the x and y directions which are defined as

$$\beta_x = S_{11} + S_{12} \quad 2.8$$

and

$$\beta_y = S_{22} + S_{12} \quad 2.9$$

respectively.

2.2.4.3 Three-dimensional Elastic Compliance Matrix

The compliance matrix that describes materials in three dimensions, is a 6×6 array of constants

$$\begin{bmatrix} S_{11} & S_{12} & S_{13} & S_{14} & S_{15} & S_{16} \\ S_{12} & S_{22} & S_{23} & S_{24} & S_{25} & S_{26} \\ S_{13} & S_{23} & S_{33} & S_{34} & S_{35} & S_{36} \\ S_{14} & S_{24} & S_{34} & S_{44} & S_{45} & S_{46} \\ S_{15} & S_{25} & S_{35} & S_{45} & S_{55} & S_{56} \\ S_{16} & S_{26} & S_{36} & S_{46} & S_{56} & S_{66} \end{bmatrix} \quad 2.10$$

For structures conforming to the lowest symmetry group, triclinic, 21 unique compliances are required to define the behaviour of the material, although only 15 of these are used to define compressibility, as compliances relating to shear do not affect the linear compressibility. For such materials it is necessary to calculate the principal directions of the linear compressibility as they are not restricted to lying on the axes of the coordinate system used to define the material. The linear compressibility of the material can be calculated in any direction using

$$\begin{aligned} \beta_L = & (S_{11} + S_{12} + S_{13})L_x + (S_{21} + S_{22} + S_{23})L_y + (S_{31} + S_{32} + S_{33})L_z \\ & + (S_{41} + S_{42} + S_{43})L_xL_y + (S_{51} + S_{52} + S_{53})L_xL_z \\ & + (S_{61} + S_{62} + S_{63})L_yL_z \end{aligned} \quad 2.11$$

where L_x, L_y and L_z are the components of the unit vector aligned to the axis in which linear compressibility is being calculated.

2.2.5 Normalised Linear Compressibility

NLC is always coupled with a larger positive linear compressibility (PLC) acting in another principal direction in order for the material volume to reduce. In addition, the minimum absolute compressibility shows the minimum value that is achieved in a given direction, but

can be misleading as it does not discriminate between a large NLC in a given direction or simply a material that is rather compliant. Therefore, to gain a better appreciation of the “overall” NLC effect, it is useful to normalise the absolute value of NLC with respect to the other strains the material is undergoing. The normalised NLC should therefore be considered in parallel with this property when assessing the NLC nature of a material. The normalised linear compressibility, β_{LN} , is defined as the ratio between absolute linear compressibility and the volume compressibility ($\beta_{LN} = \frac{\beta_L}{\beta_V}$).

2.2.6 Compressibility Capacity

The term “linear compressibility” refers to the compressibility of a given material across a specific axis. The term does not imply the property need be linear in nature and can, for instance, vary with the observed strain of a material on a given axis. The linear compressibility can therefore change across a given pressure range.

Compressibility capacity, $\chi_{\beta L}$, (Cairns and Goodwin, 2015) is defined as the integral of the linear compressibility across the pressure range over which it acts and is expressed as

$$\chi_{\beta L} = - \int_{p_1}^{p_2} \beta_L(p) dp \quad 2.12$$

where p_1 and p_2 are the minimum and maximum pressures over which the linear compressibility is being assessed. This quantity is a measure of the maximum strain that could be encountered by the material over a given pressure range. Knowledge of the pressure range over which the NLC is active is however, not always reported. This property, along with the absolute and normalised compressibility, should be analysed in parallel when assessing a material.

2.2.7 Coincident Occurrence of NLC and Stretch Densification

By manipulating Equation 2.8, the linear compressibility of a two-dimensional system can be deduced in terms of the Poisson’s ratio and Young’s Modulus

$$\beta_i = \frac{1 - \nu_{ij}}{E_i} \quad 2.13$$

where i and j are an arbitrary set of orthogonal axes in two -dimensional space. This shows that for β_i to be negative, $\nu_{ij} > 1.0$, which implies the material densifies under tensile loading on the i -axis. Similarly for a three-dimensional system, the equation for linear compressibility on a given axis, i , can be calculated using

$$\beta_i = \frac{1 - \nu_{ij} - \nu_{ik}}{E_i} \quad 2.14$$

where i, j and k are an arbitrary set of orthogonal axes in three -dimensional space. Therefore for β_i to be negative, $\nu_{ij} + \nu_{ik} > 1$ either or both of the Poisson's ratios must be greater than 0.5. This means the material must undergo stretch densification when loaded on the i -axis. Therefore any axis of NLC must also be an axis on which stretch densification is present. The equivalency of these two properties could make it easier to prove the presence of NLC within material specimens on which the application of a hydrostatic load is not viable.

It should also be noted that because an area compressibility in the plane, ij , is equal to $\beta_i + \beta_j$, this rule also applies to materials with NAC. However, the material densifies when loaded bi-axially on the plane of NAC.

2.3 NLC Materials Research

2.3.1 Introduction

This section presents an overview of the materials currently known to exhibit NLC. These materials have been split into biological systems, macro structures and crystalline structures. Further sub-divisions have been included under crystalline structures to distinguish between NLC manifested via a phase change and NLC caused directly by the elastic properties of the framework. In addition to this, due to the large number of articles published on the subject, a sub-section has been dedicated to metal-organic-frameworks (MOFs) that exhibit NLC. Importantly, efforts have been made to highlight the method used in each

reported case to help judge the validity of the reported data and to help conclude whether further substantiation would be required.

2.3.2 Biological Systems

Initial research into abnormal material properties has often found that there are some instances of the property within nature. This gives some encouragement to the possibility of applications, as the process of evolution has selected the property suggesting it offers advantages. NLC is no exception as some instances of biological materials exhibiting NLC have been reported and as the research is still at an early stage, it is probable that others will also surface.

Of particular interest is a study looking at the muscular structure of caecilians, a class of limbless amphibians which live underground and have impressive burrowing capabilities (O'Reilly et al., 1997). The chest cavity in these creatures is surrounded by an array of interconnected helical tendons that run the length of the body of the animal. This structure can be likened, albeit rather simply, to that of a Chinese finger trap. This structure undergoes stretch densification when loaded axially, meaning the axial strains are smaller than the lateral strains. In the case of the caecilian, the forces applied by the muscles onto the helical tendons act radially. The helical structure converts this radial force into an axial force and increases its magnitude. Muscles in the creature were found to contract the helices over a portion of the length of the body pressurising the chest cavity, which in turn drove the head forward. The study concluded that this method of locomotion was fundamental to the unique burrowing ability of this class of creature. Further to this, when compared to other species of limbless tetrapod, which are composed of a more longitudinally aligned muscular and tendon system, the caecilians produced twice the forward driving force. These types of biological structure are also referred to as muscular hydrostats. A muscular hydrostat is a biological system in which a fluid is encased within a helical array of tendons or muscles. The contraction of these tendons and/or muscles causes the system to extend. Examples of muscular hydrostats

include elephant trunks, tongues, octopus limbs and squid tentacles (Kier.W, 1985). The structure is regarded as being highly efficient.

Another biological structure found to exhibit NLC is the lipid bilayer, which is composed of two chains of lipid molecules and constitutes much of the membrane of a biological cell. Interestingly, when submitted to a hydrostatic pressure, the thickness of this layer increases and it therefore has NLC (White and King, 1985, Macdonald and Fraser, 1999). Results concluding a 3.75% increase in the thickness of a lipid bilayer when the hydrostatic pressure was increased from ambient pressure to 1.9kbar have been documented (Braganza L.F., 1986).

2.3.3 Macro Structures

The so-called “wine-rack” mechanism was the first attempt at explaining the occurrence of NLC in crystalline materials. This mechanism was proposed by Baughman in the initial review of NLC materials published almost two decades ago (Baughman et al., 1998a). A simple diagram of the mechanism is shown in Figure 2.2.

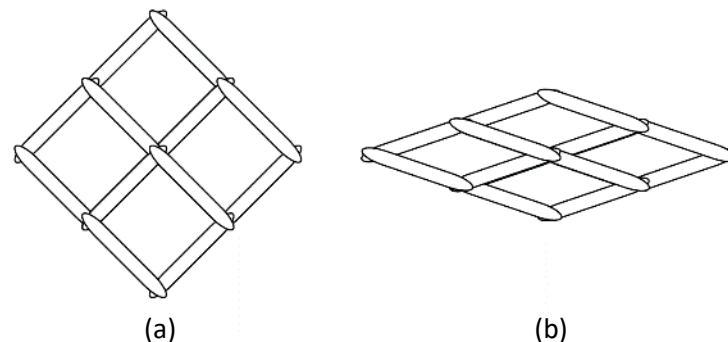


Figure 2.2 Representation of Baughman’s “wine-rack” mechanism shown in (a) the unloaded state and (b) the loaded state

The mechanism is a pin joined frame that undergoes significant contraction when extended along a single axis as shown in Figure 2.2. Baughman referred to this structure as an analogy and did not include any further analysis of it.

Research theorising a macro structure that exhibits NVC, has been produced using a finite element (FE) code (Gatt and Grima, 2008). The hydrostatic pressure was however penetrative, i.e. was applied on both internal and external surfaces and hence the reported results do not violate the laws of thermodynamics, although the hydrostatic pressure is not consistent with the widely recognised definition published by Nye (Nye, 1964). The unit-cell of the structure proposed is shown in Figure 2.3. The structure is made up of bi-material strips and uses a similar principle to that which has been used to create structures with a negative coefficient of thermal expansion in a previous study (Lakes, 2007). Negative thermal expansion is achieved in this instance due to a mismatch between the coefficients of thermal expansion in the two materials. The directions in which the strips bend on heating can be controlled such that overall volume of the structure increases. Similarly where a different stiffness is applied to each material on a bi-material strip, the direction of bending of each beam under penetrative hydrostatic loading can be controlled. Hence if the direction of bending can be controlled on each ligament, the square blocks shown in Figure 2.3 can be designed in such a way that the structure can expand.

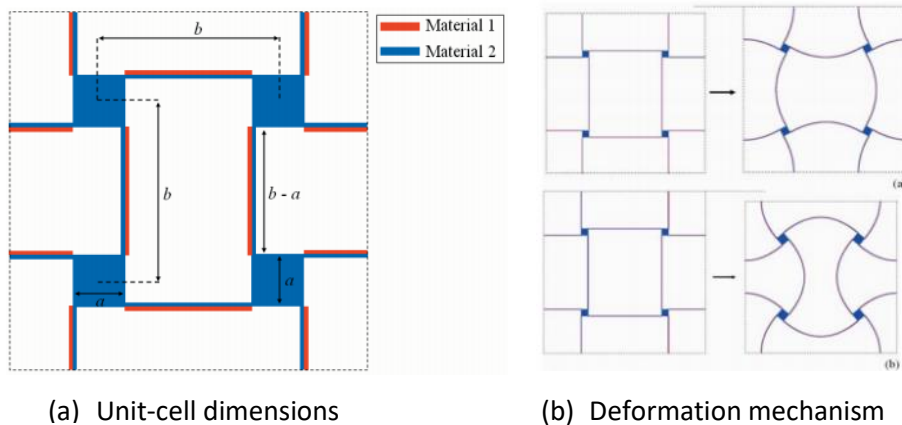


Figure 2.3 Schematic of the unit-cell reported to produce NVC when submitted to a penetrating hydrostatic pressure (Gatt and Grima, 2008)

Analytical calculations by the same authors have also been carried out on two- and three-dimensional truss networks composed of rigid rods connected by pin joints (Grima J.N Attard D., 2008). NLC was also reported as being tailorable both in magnitude and direction

and the researchers again claimed that NVC is possible. Experimental results would be required to substantiate these conclusions.

NLC within two- and three-dimensional composites has been postulated via the use of FE simulations (Weng et al., 2008). Both the two- and three-dimensional models were composed of a stiff material that ran across the diagonals of each unit-cell and a second material that occupied the remaining unit-cell area or volume. The aspect ratio of the unit-cell was modified and the linear compressibilities were calculated via analysis of the elastic properties. The maximum normalised values of NLC were found to occur at unit-cell aspect ratios approaching one for the two-dimensional model and two for the three-dimensional model. No further discussion of the mechanism was presented.

2.3.4 Crystalline Systems

2.3.4.1 Preamble

Where appropriate, materials documented in this section of the literature review are also listed in Appendix D alongside key information. 13 of the materials listed in the appendix originate from Baughman's review article (Baughman et al., 1998a), where an analysis of published elastic constant data from the Landolt-Borstein database (Every and McCurdy, 1993) had been surveyed. However, on independent review of this data, a number of NLC materials were identified that were missed by Baughman and these are also listed. Additional data has also been found relating to some of the previously discovered NLC materials, which are mentioned later in this literature review.

2.3.4.2 NLC via the Molecular Framework

This sub-section reviews a number of the articles in the literature concerning the analysis of molecular structures that have been proven to show NLC via experimentation or are predicted to exhibit NLC through the use of different modelling methodologies.

Density function theorem (DFT) calculations have been carried out on 121 different siliceous zeolite polymorphs (Coudert, 2013). The study found that 16 of these structures had

NLC. It is therefore theorised that NLC is not a rare property in this class of material, although no experimental data has been collected which support these predictions. The structure of the zeolites that potentially exhibit NLC is likened to that of a “wine-rack”, hence it is postulated that this is the source of the NLC mechanism. The maximum values of NLC range from -0.2 TPa^{-1} to -13.7 TPa^{-1} and are relevant to the GIS (gismondine) topology, which is deemed to be a suitable candidate for fabrication due to its calculated stability.

Three other zeolite materials, natrolite, mesolite and scolecite, have been observed via diamond anvil tests to undergo a pronounced volume expansion between pressures of 0.8 and 1.5 GPa (Lee et al., 2002). This is due to sorption of hydrogen molecules from the pressure-transmitting fluid, in this case water, and hence the volume increase does not violate thermodynamics.

Ultrasonic velocity measurements have been taken to determine the elastic stiffness matrix of Caesium dihydrogen phosphate (CsH_2PO_4) (Praver et al., 1985). The material was subsequently found to have NLC of -260 TPa^{-1} on an axis close to the c-axis of the monoclinic unit-cell. It is postulated in the literature that the NLC is instigated by a “wine-rack-like” topology originating from the rotation of the PO_4 tetrahedron caused by the weak bonding between the layers producing a large PLC. The atomic structure of caesium dihydrogen phosphate is displayed in Figure 2.4.

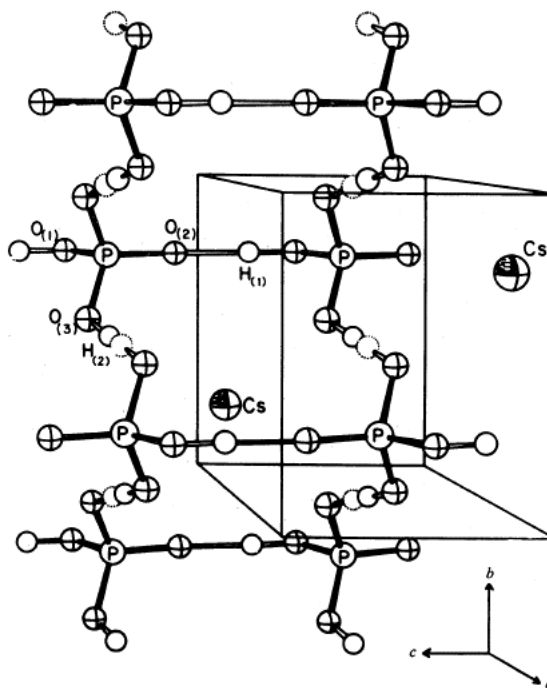


Figure 2.4 Atomic structure of CsH_2PO_4 (Prawer et al., 1985)

The structure of the trigonal polymorph of selenium is of interest as it has a helical chain structure that can be referred to as being the molecular equivalent of those helical structures found within the burrowing creatures referred to in Section 2.3.2 (see Figure 2.5). The helical chain structure is shown to have NLC along the c -axis (vertical axis) of the unit-cell. The response of the structure to increasing pressure was measured using both x-ray neutron diffraction and neutron time of flight diffraction (McCann et al., 1972). When pressurised, the structure was observed to expand along the c -axis of the lattice and this expansion was accompanied by a much larger contraction along the a -axis (radial axis). Intra-helical bond lengths remained constant and the pitch angle of the helix was reported to widen, hence creating a lengthening of the unit-cell. This was accompanied by a reduction in the inter-helical bond length which corresponded to a large PLC along the a -axis. This is largely because the bonds joining the selenium atoms within the helical chains are covalent and are much stronger than the weaker van der Waal bonds acting between the helical chains. The opposite of this response has also been reported when the structure has been submitted to increases in temperature (Munn, 1972, Straumanis, 1949), hence the structure also exhibits

negative thermal expansion on the axis of the maximum NLC. Similar results regarding NLC have also been reported for trigonal tellurium which has a very similar structure to that of trigonal selenium (Jamieson and McWhan, 1965).

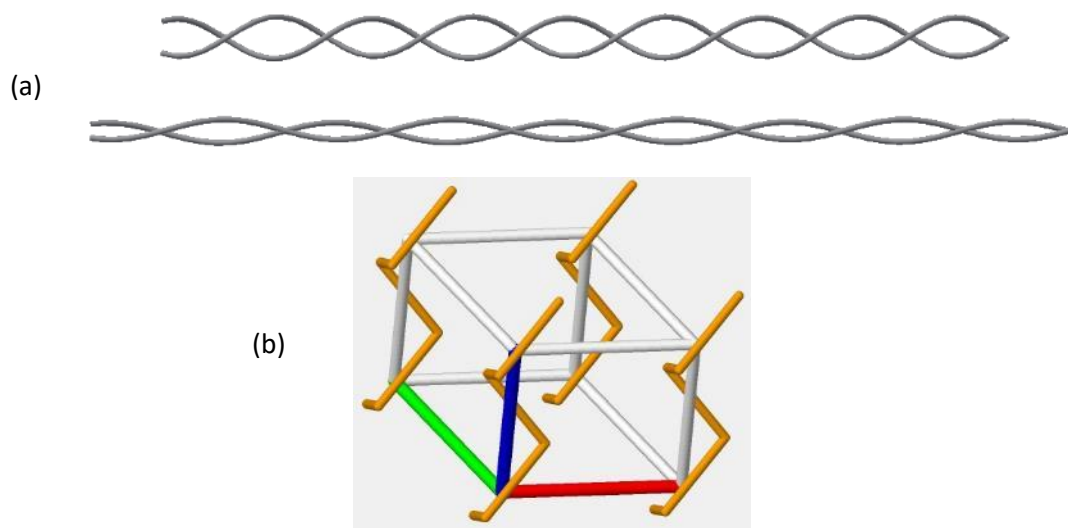


Figure 2.5 Representations of: (a) a generic helical chain structure lengthening under hydrostatic load; and (b) the crystallographic wireframe of trigonal selenium.

Further investigation into the structural response of both tellurium and selenium to increased hydrostatic pressure has been carried out using experimental Raman spectroscopy and has been complemented by density function calculations (Hsueh H.C., 2000). Good agreement is reported between the two methodologies confirming much of the previous research concerning the NLC mechanism within the specific polymorphs of these elements. Additional experimental results coupled with analytical DFT calculations also showed that helical selenium chains, when confined to channels within $\text{AlPO}_4\text{-5}$ single crystals, still retain NLC. (Ren W., 2009).

Other molecular structures have been shown, via the use of experimental methods, to have a “wine-rack”-like structure that instigates NLC. A neutron diffraction study showed that $\text{Ag}_3[\text{Co}(\text{CN})_6]$ had a maximum NLC of $-76(9) \text{ TPa}^{-1}$, but at a pressure of 0.19 GPa, the structure underwent a phase change, after which the magnitude of the NLC was greatly reduced (Goodwin et al., 2008). The group that authored this research later modified this fabricated structure by adding counter-ions within the voids to keep the structure stable at

higher pressures (Cairns et al., 2012). The new material, $\text{KMn}[\text{Ag}(\text{CN})_2]_3$, was found, via the use of neutron powder diffraction experiments, to have a maximum NLC of $-12.0(8) \text{ TPa}^{-1}$ which was active up to a pressure of 2.2GPa.

NAC is considered to occur more rarely than NLC and only a few materials have been identified that exhibit this property, all of which also exhibit negative thermal expansion. In all cases so-called Lifshitz modes, previously associated with negative thermal expansion (Lifshitz, 1952), have been responsible for the NAC. These materials are composed of layers that are weakly bonded in the stacking direction, while being fairly strongly bonded in-plane i.e. $C_{12}, C_{13} > C_{33}$. When heated these structures expand in-plane and contract in the stacking direction and hence exhibit negative thermal expansion. Similarly, when submitted to hydrostatic loading these materials expand in the stacking direction and shrink in-plane. The materials found to exhibit NAC are sodium vanadate (Loa et al., 1999) (Nakao et al., 1997), TiGaSe_2 (Seyidov and Suleymanov, 2010) and silver tricyanomethanide (Hodgson et al., 2014).

The development of carbon nano-tube sheets, often referred to as buckypaper, has led to the discovery that their structure can be modified to produce a negative Poisson's ratio (Hall et al., 2008, Coluci et al., 2008). Further to this, other researchers have produced carbon nano-tube sheets, intended for the creation of artificial muscles, that conversely have very high Poisson's ratios (Aliev et al., 2009). The Poisson's ratio of these carbon nano-tube sheets is dependent on the construction of the sheet and is hence tailorable. More recently, force-field based simulations have been used to predict NLC in specific arrays of hexagonally arranged carbon atoms (Formosa et al., 2015).

A combination of DFT calculations and experimental data has shown that $\text{LnFe}(\text{CN})_6$ (where Ln=Ho, Lu or Y) has NLC along the c-axis of the crystal and is active between 0.5 and 2.5GPa after a period of PLC on all axes between ambient and 0.5GPa (Duyker et al., 2016). The mechanism proposed, which is caused by the "molecular gears and torsion springs" in the structure, is quite different to the wine-rack. Figure 4.6(a) shows a c-axis projection of the structure for increasing deformation (left to right), and illustrates a period of PLC followed by

NLC. The image shows that the pressure-induced rotation of the torsional YN_0 units, caused by the rigid rotation of the FeC_6 , causes shrinkage and then elongation of the unit-cell along the c -axis. Rotation of the YN_0 units initially causes the unit to become “out of line” with the unit-cells above and below and hence the distances between different neighbouring molecules increases allowing the structure to shrink along the c -axis. Continued rotation of the YN_0 units causes these distance to get smaller therefore creating a repulsive force causing the unit-cell to elongate. This mechanism is likened to that of a rotating cam, as is shown in Figure 4.6(b) and explains the positive and negative regions of linear compressibility in a simple analogy.

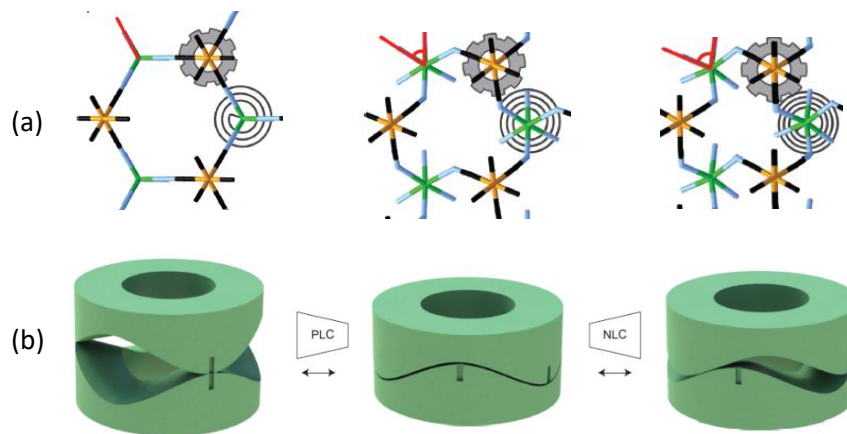


Figure 2.6 “Spring-and-gear NLC mechanism” (a) Projection along the c axis of the $YFe(CN)_6$ structure, showing the distortion of the structure under pressure. This twisting of the rigid gear-like $Fe(CN)_6$ units is accompanied by rotation of the torsional spring-like YN_0 units. Y atoms are shown in green, Fe in orange, C in black and N in blue. (b) Illustration of the cam-like behaviour of the YN_6 unit. As the YN_6 unit rotates it causes a PLC followed by NLC along the c -axis (Duyker et al., 2016).

Interestingly, a number of superconducting materials have been reported as having NLC. This is probably related to the behaviour these materials exhibit when cooled, which results in rapid contraction in one or more directions. Such materials have included uranium cobalt germanium (Adamska et al., 2010), europium iron arsenide (Uhoya et al., 2010) and $TiGaSe_2$ (Seyidov and Suleymanov, 2010).

2.3.4.3 Metal Organic Frameworks (MOFs)

Metal organic framework structures (MOFs) are hybrid single-phase materials made up of metallic and organic elements (Tan and Cheetham, 2011). A very large amount of research has been carried out on MOFs with more than 20,000 papers being published on the subject, as well as 170 review articles (Coudert and Fuchs, 2016). The material is often structured such that there are clusters of stiffly bonded metallic molecules connected via more compliant inorganic links (Zhou et al., 2008). MIL-53 is a family of materials within the MOF group that closely resembles a “wine-rack” structure (Serra-Crespo et al., 2015). Quantum calculations have predicted the occurrence of NLC in some of the MIL-53 materials (Ortiz et al., 2013, Ortiz et al., 2012), and the material has more recently been proven to have NLC via the use of powder x-ray diffraction in conjunction with diamond anvil tests (Serra-Crespo et al., 2015). MIL-53(Al) was shown to have a maximum NLC of -28 TPa^{-1} that is active between 0 and 3GPa. A second MOF was also investigated in this study, NH₂-MIL-53(Al). This MOF exhibited a maximum NLC of -27 TPa^{-1} between 0 and 2GPa. The origin of NLC in both of these materials is the proportionally weak rotational resistance with respect to the axial resistance of the dicarboxylate linkers which connect the metallic clusters. This allows the structure to pivot very much like a “wine-rack”. Other examples of MOFs exhibiting NLC are present in the literature, where the mechanism can be attributed to being similar to the one described here.

A tetragonal MOF, specifically UTSA-16, has been shown experimentally to have NLC (Binns et al., 2016). Interestingly, it is proposed that the behaviour in this case is not due to a “wine-rack” topology. It is instead claimed that the behaviour is caused by a rotation of the rigid Co₄O₄ units that causes contraction along the a- and b-axes but instigates a lengthening along the c-axis because the cobalt(II) tetrahedral linkers must consequently lengthen as illustrated in Figure 2.7.

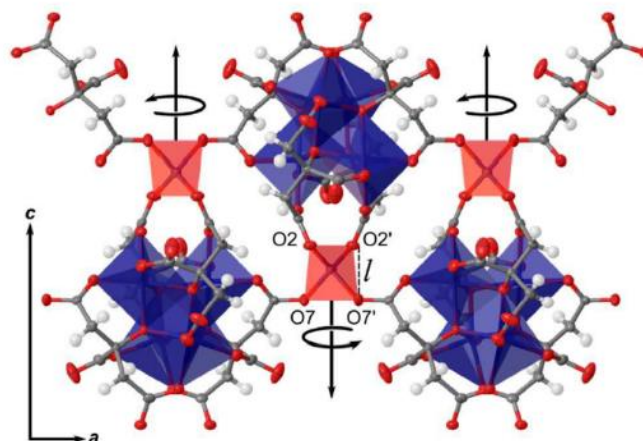


Figure 2.7 NLC mechanism within UTSA-16 (Binns et al., 2016)

NLC has been predicted in the MIL-140 MOF via the use of DFT calculations (Ryder et al., 2016). Four different polymorphs were investigated, two of which had NLC. The mechanism causing this behaviour was established as being the wine-rack. This class of MOF was concluded to have an envelope of stiffness properties that spanned those of metals, ceramics, polymers and foams. This, along with the MOF having a very high calculated stability, could make it the subject of further research, particularly if engineering applications are to be sought.

NLC has also been identified in the zinc alkyl gate class of MOFs, specifically ZAG-4 and ZAG-6 via the use of x-ray crystal diffraction techniques (Gagnon et al., 2013). The driving mechanism was found to be so-called “proton-jumping” (Ortiz et al., 2014). Such pressure-induced transitions are quite rare in the literature and have not been reported in MOFs before. As such, little is currently known about the postulated NLC mechanism.

2.3.4.4 NLC triggered by a Phase Change

A phase change occurs when the internal molecular structure of a material is no longer stable and the crystal rapidly transitions to another more stable structure. This change can also alter the symmetry group of the material. Changes in the phase of a material can be initiated by changes in pressure, temperature or the magnetic or electric field. Of relevance to

this literature review are materials that undergo a pressure-induced phase transition that also results in “spontaneous strain”. This is where the volume of the unit-cell is conserved. However, the dimensions of the unit-cell can change dramatically, instigating an expansion along one or two axes allowing NLC to be observed. It is also permitted thermodynamically for a material to increase in volume when undergoing a pressure induced phase change, although no real materials have been identified which exhibit this behaviour.

Recent research shows that hydrocarbon chains will succumb to a very pronounced “escape transition” phase change under high hydrostatic loading, where the polymer chains suddenly become aligned (Skvortsov A.M., 2007, Dimitrov et al., 2009). It has also been suggested that NLC in PtS could also have been triggered by a phase change, however this is yet to be fully substantiated experimentally (Marmier et al., 2010b). Paratellurite has also been shown to exhibit NLC via a pressure-induced phase change (Skelton E.F., 1976). The symmetry of the structure changed from tetragonal to orthorhombic at 8kbar, where the structure was observed to expand linearly on one axis. Also, during the high pressure orthorhombic phase, a small NLC was observed between 8 and 90kbars.

Experimental methods involving Raman beam scatter measurements and a diamond anvil cell have shown sodium amidoborane to have NLC (Magos-Palasyuk et al., 2016). DFT calculations performed by the authors confirm that the NLC is not driven by a structural wine-rack but by the formation of new hydrogen bonds that cause a very pronounced sudden increase in length on the c-axis of the crystal at $\approx 9\text{GPa}$.

2.4 Negative Poisson’s Ratio Research

2.4.1 Introduction

Research into NLC materials has only recently been of major interest to the scientific community; however the more general field of “negative materials” has existed for much longer. Materials with a negative Poisson’s ratio, also referred to as auxetic materials, were one of the first “negative materials” to be subject to a great deal of scientific interest. The property has been found to exist in numerous crystalline materials and has also been

manifested in a number of fabricated structures via a number of different mechanisms. As research into auxetic materials is in a more advanced state than that into NLC, a variety of mechanisms have been discovered and suitable applications have been considered. As knowledge of these mechanisms could provide a useful perspective from which to perform further NLC research, a partial review of auxetic materials.

2.4.2 Description of Negative Poisson's Ratio

The Poisson's ratio, ν , is the ratio between the longitudinal strain ϵ_{lat} and the axial strain, ϵ_{axi} ,

$$\nu = \frac{-\epsilon_{lat}}{\epsilon_{axi}} \quad 2.15$$

Materials that have a negative Poisson's ratio expand laterally when loaded in tension or conversely contract laterally when loaded compressively along a single axis. The well-established theoretical range of values the Poisson's ratio can take within an isotropic material are $-1 \leq \nu \leq 0.5$ (Gere and Timoshenko, 1996).

Although a negative Poisson's ratio is considered to be an abnormal property, a number of publications over the last century have reported some very well-known materials as being auxetic. Amongst these materials are; iron pyrites (Love, 1944), bone (Williams and Lewis, 1982), cat skin (Veronda and Westmann, 1970) and rock (Gregory, 1976). However the manufacture of an auxetic material did not take place until much later (Lakes, 1987).

Further research found that the unusual property was widespread in crystalline structures. This is evidenced by the finding that 69% of cubic metals (Baughman et al., 1998b) and 25% of monoclinic crystals (Rovati, 2004) were found to exhibit a negative Poisson's ratio. Further research (Ting and Chen, 2005) analysing the presence of negative Poisson's ratios in cubic materials has shown that the direction of the negative Poisson's ratio can change for different combinations of the three elastic constants. This shows that there is a rich elastic complexity in the "lowly" cubic symmetry.

2.4.3 Negative Poisson's Ratio Materials and Mechanisms

A foam exhibiting auxetic behaviour was created by tri-axially compressing and heating conventional foams within a cast (Lakes, 1987). This process created an isotropic “re-entrant” foam structure that could then expand laterally when loaded in tension much like the re-entrant honeycomb structure depicted in Figure 2.8(b). Analysis of this re-entrant structure showed it is possible to attain a Poisson's ratio close to -1 by altering the internal angle of the rib, while values of $\nu = -0.8$ have been measured experimentally (Choi and Lakes, 1995). The fabrication method adopted was later refined with greater thought being applied to the heating temperatures and hold times. This ensured that the specimens had a higher degree of homogeneity (Chan and Evans, 1997). Honeycombs have also been developed that make use of this re-entrant structure to create an auxetic effect (Lee et al., 1996). This re-entrant structure is displayed in Figure 2.8. The Poisson's ratio for both re-entrant and conventional honeycombs can be calculated using

$$\nu_{xy} = \frac{\cos^2 \theta}{(h/l + \sin \theta) \sin \theta} \quad 2.16$$

(Gibson and Ashby, 1999)

where h , l and θ are defined in Figure 2.8.

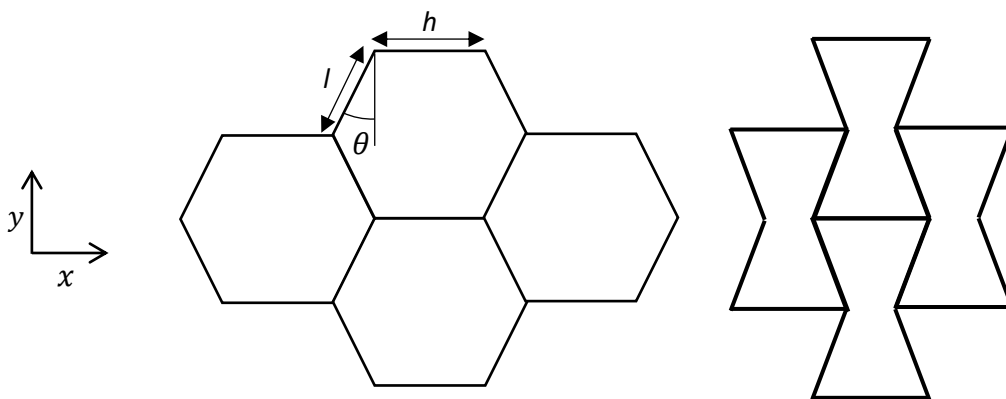


Figure 2.8 Conventional and re-entrant honeycomb structures

Drawn PTFE has been shown to have a negative Poisson's ratio when loaded in the direction it was drawn (Caddock and Evans, 1989). The mechanisms that cause the auxetic effect within PTFE are shown in Figure 2.9.

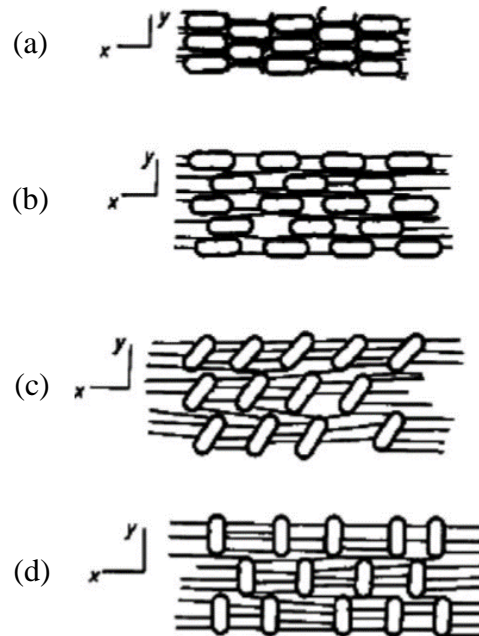


Figure 2.9 Representation of the auxetic mechanism in drawn PTFE

Figure 2.9(a) shows the tightly packed array of nodules (ovular shapes) and fibrils (fibres running parallel to one another in the x direction). When a positive strain is applied to the structure in the x direction, the fibrils initially become taut and allow the nodules to separate (Figure 2.9 (b)). This creates a positive strain in the y direction. Following this, the further application of strain in the x direction causes the nodules to rotate (Figure 2.9(c) and (d)), thus creating a second auxetic mechanism as further expansion in the y direction is observed. This research was also accompanied by an analytical calculation that provided impressive agreement with the experimental results (Evans and Caddock, 1989). A maximum negative Poisson's ratio of -11 was found by the authors during experimentation although the negative Poisson's ratio is strain-dependent and is only attainable when the strain is applied along the axis of drawing.

2.4.4 Favourable Properties and Applications

The elastic behaviour of an isotropic material can be generally described using four parameters;

- Young's Modulus, E
- Bulk Modulus, K
- Shear Modulus, G
- Poisson's Ratio, ν

These elastic properties are derived from the compliance tensor of the material which implies that these elastic properties are linked. The four elastic constants listed above are related via

$$E = \frac{9KG}{(3K + G)} \quad 2.17$$

$$K = \frac{E}{3(1 - 2\nu)} \quad 2.18$$

$$G = \frac{E}{2(1 + \nu)} \quad 2.19$$

and

$$\nu = \frac{1}{2} \left(\frac{3K - 2G}{3K + G} \right) \quad 2.20$$

Conventional isotropic materials have a Young's modulus larger than the shear modulus, however for materials with a Poisson's ratio < -0.5 , Equation 2.19 shows that the shear modulus will become larger than the Young's modulus (Choi & Lakes, 1992). Conversely, if the Poisson's ratio approaches 0.5, Equation 2.18 shows that the bulk modulus will greatly exceed the shear modulus. Such materials are referred to as being incompressible. These equations are only applicable to isotropic materials and the relationships for anisotropic materials become far more complicated. However, specific shear moduli within highly anisotropic materials have been shown to be elevated where the materials has been altered to have a large negative Poisson's ratio (Ju and Summers, 2011).

When a sheet made from a conventional material is loaded in bending, the sheet responds to the tensile force on the surface of the sheet by attempting to contract laterally, this causes a saddle shaped surface (anticlastic curvature) to be formed as illustrated in Figure 2.10. Conversely, when a sheet composed of an auxetic material is loaded in bending, the sheet will expand laterally on the surface in tension, causing a dome like or synclastic curvature to form. This property allows more natural contours to be formed and could be advantageous in the construction of body armour; a tighter match to the human body could be achieved.

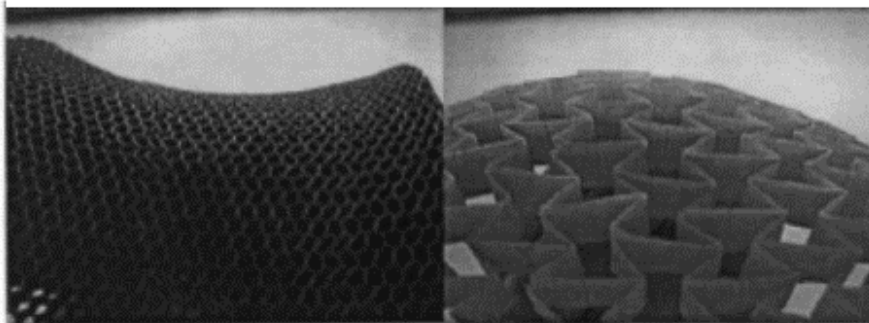


Figure 2.10 Bending response of: (a) a non-auxetic honeycomb; and (b) an auxetic honeycomb (Lakes and Witt, 2002)

Classical elastic theory shows that the indentation resistance (hardness) of an isotropic material is governed by

$$H \propto \left[\frac{E}{(1 - \nu^2)} \right]^\kappa \quad \begin{array}{l} 2.21 \\ \text{(Timoshenko and} \\ \text{Goodier, 1970)} \end{array}$$

where $\kappa = 1$ is applicable for a uniform pressure distribution and $\kappa = \frac{2}{3}$ is used for Hertzian contact. The equation shows that hardness is inversely proportional to $1 - \nu^2$. Hence large negative Poisson's ratios will incite large values of indentation resistance (Evans and Alderson, 2000).

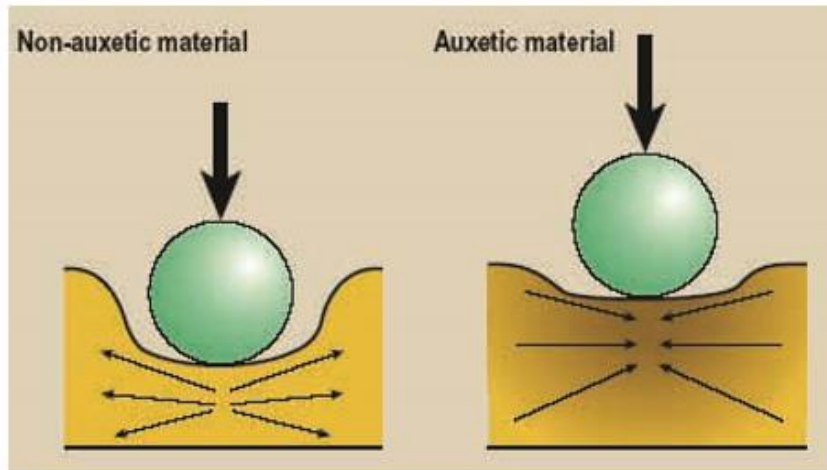


Figure 2.11 The response of (a) non-auxetic and (b) auxetic materials to localised indentation (Alderson, 1999)

An explanation of this would be that non-auxetic material will spread away from a site of localised indentation, and conversely, auxetic materials will contract in directions perpendicular to the direction in which the load is being applied. This will cause the loaded region to densify and resist further indentation (Smith, et al, 1999) as illustrated in Figure 2.11.

Improved hardness in materials altered to be auxetic has been reported in a number of fabricated polymeric (Chan and Evans, 1997) and metallic (Lakes and Elms, 1993) auxetic foams, carbon fibre composite laminates (Alderson et al., 2005c) and microporous polymers (Alderson et al., 2000a). Impressively, an increase in the hardness of auxetic polyethylene over conventional polyethylene of a factor of two has been reported (Alderson et al., 1994). Of particular significance in this study was that for low loading (10~100N), the hardness was increased by a factor of 8 where the Poisson's ratio had been changed from 0 to -0.8 . The potential for a material bearing this property has been identified in the design of foam mattresses which would provide more support and comfort. In addition, it has been postulated that the design of artificial blood vessels could make use of auxetic materials. In the event of increased blood pressure in the cavity a conventional material would undergo a reduction in wall thickness while an auxetic material would densify in the loaded region, thus reducing the likelihood of wall rupture.

Auxetic foams have been shown to have improved acoustic damping properties when compared to their conventional counterparts (Scarpa et al., 2004). Altering the pore size within auxetic foams has been shown to make the material more effective at attenuating sounds of different frequencies (Howell et al., 1994). Altering this parameter within ultra-high-molecular-weight polyethylene (UHMWP) increased the maximum ultrasonic sound attenuation value by 1.5 times that of conventional UHMWP (Alderson et al., 1997, Alderson et al., 2000b).

Tuneable filters made from auxetic material could allow greater control of the size of the molecules that are allowed to pass through by loading the filter appropriately (Alderson et al., 2005b, Alderson et al., 2005a, Davis and Lobo, 1992). Auxetic materials could be used in pressure sensors as the reduced bulk modulus makes them more sensitive to hydrostatic pressure (Avellaneda and Swart, 1998).

Further to this, a number of different simple geometries have been identified that can have auxetic properties, these have included chirals (Grima et al., 2008), rotating units with squares (Grima and Evans, 2000), triangles (Grima and Evans, 2006), and tetrahedra (Alderson and Evans, 2001). This has created more possibilities for the manufacture of auxetic materials.

2.5 Conclusions

In last decade, many articles have been published that document the discovery of NLC materials. Most of these materials have their abnormal behaviour attributed to a manifestation of the “wine-rack” mechanism, and a much smaller proportion have NLC triggered via adsorption, phase change or another mechanism. A compendium of these materials is included in Appendix D, where key information is listed about each material where possible

It is possible to see from the brief overview of auxetic materials that this bizarre and novel property has created a number of useful applications that are continually being developed. The success of auxetic materials research is encouraging when considering the potential of other similarly unconventional material properties.

The literature focused around NLC does not currently show any inclination toward producing an eventual industrial application and although referenced numerous times, no in-depth examination of the “wine-rack” mechanism has been documented. Furthermore, no engineering materials have been identified as having NLC. These are gaps in the literature that this thesis attempts to address in the following chapters.

Chapter 3

Two-Dimensional “wine-rack” Structures and Newly Identified NLC materials

3.1 Introduction

3.1.1 Background

The “wine-rack” analogy (Baughman et al., 1998a) has dominated discussion of the NLC mechanism since being published almost two decades ago and almost all currently identified NLC materials are assumed to exhibit NLC via this mechanism. However, to date, no studies have looked into how altering simple parameters within the “wine-rack” could vary the normalised and absolute values of NLC. The work on two-dimensional structures presented in this chapter has been published in 2012 (Barnes et al., 2012). In addition, there are no common engineering materials within the literature that have been shown to have NLC.

3.1.2 Scope

A two-dimensional form of the “wine-rack” mechanism is analysed in this chapter by representing it using two-dimensional scale-independent structures in which interconnecting Euler beams are modelled between nodal points. Conclusions made using this method can hence be used to help deduce the source of NLC behaviour at any length scale. Atomic interactions can be simplified, albeit rather crudely, to act like an array of nodes connected via beams. Such a methodology has been previously applied to explore the auxetic possibilities within a cubic symmetry (Hughes et al., 2010). The methodology simulates both the axial and rotational components of stiffness as the beam’s resistance to bending, $\frac{L^3}{EI}$, and the beam’s resistance to axial compression, $\frac{L}{E\phi}$ respectively (where L is the beam length, E is the constituent material’s Young’s modulus, I is the second moment or area of the beam and ϕ is

the cross-sectional area of the beam). Similarly, the results from these framework models can also be used to help inform the manufacture of NLC materials at any length scale. Both FE simulations using a commercially available code (DASSAULT, 2009) and analytical derivations are used in parallel as a means of substantiating the results.

Initially, the assumptions relevant to both FE and analytical methodologies are stated in Section 3.2 and the two-dimensional symmetries explored in this chapter are explained in Section 3.3. The proposed structure is then shown in Section 3.4 and the derivation of the analytical formulae and the results for the analytical modelling are presented in Section 3.5 and the results from the FE modelling are shown in Section 3.6. Conclusions arising from this study are given in Section 3.7. Informed by the conclusions of this study, Section 3.8 goes on to document the search for new NLC materials and discuss the materials identified.

3.2 Modelling Assumptions

The modelling within this chapter considers only linear elastic behaviour at small strains. No attention is given to the effect of plasticity, plastic hinging or non-linear geometry. The beam sections are assumed to be circular and to remain circular when loaded, the constituent material properties are also assumed to be both homogenous and isotropic. Displacements and strains are considered to be very small and to occur quasi-statically, and therefore the possibility of beam buckling is not investigated. Beams modelled within the chapter are slender, hence analytical derivations consider only Euler beam theory as opposed to Timoshenko beam theory as no allowance for internal shear deformation is required.

3.3 Two-Dimensional Elastic Symmetries

3.3.1 Preamble

In order to proceed it is necessary to determine the elastic symmetry of the structures that are to be analysed and hence the formulae required. This section suggests two possible two-dimensional symmetries; square and rectangular.

3.3.2 Square

In two dimensions a material can require up to a maximum of six unique elastic compliances to define its behaviour. The compliance matrix for a two-dimensional square symmetry is shown in Equation 3.1 and contains three unique values. The linear compressibility of a square symmetry is isotropic and calculated as $\beta_L = S_{11} + S_{12}$. The linear compressibility is therefore isotropic and as such cannot take a zero or negative value as this would imply an overall increase in the area of the two-dimensional model in the presence of a hydrostatic pressure. The requirement for further investigation into square symmetries can therefore be discounted.

$$\begin{bmatrix} S_{11} & S_{12} & - \\ S_{12} & S_{11} & - \\ - & - & S_{33} \end{bmatrix} \quad 3.1$$

3.3.3 Rectangular

The compliance matrix for a two-dimensional rectangular symmetry is shown in Equation 3.2. For this two-dimensional rectangular case there are 4 unique elastic compliances.

$$\begin{bmatrix} S_{11} & S_{12} & - \\ S_{12} & S_{22} & - \\ - & - & S_{33} \end{bmatrix} \quad 3.2$$

When considering this two-dimensional rectangular system, the linear compressibility upon a given axis can be calculated using

$$\beta_L = S_{11} + S_{12} - (S_{11} - S_{22})L_y \quad 3.3$$

where L_y is the y component of the unit vector aligned with the axis on which linear compressibility is to be calculated. It follows from this equation that the maximum and minimum values of linear compressibility will be present on the principal axes, where $\beta_x = S_{11} + S_{12}$ and $\beta_y = S_{22} + S_{12}$. This implies the possibility of NLC within a two-dimensional rectangular symmetry as $\beta_x \neq \beta_y$, therefore one of the values can be negative.

3.4 Modelled Structure and Input Parameters

To propose structures that conform to rectangular symmetry and exhibit NLC, a number of beam types are considered that correspond to nearest and second nearest neighbour nodal interactions, where nodes are placed at the four corners of the unit-cell, this is illustrated in Figure 3.1. Three classes of beams are suggested; type Ia beams, aligned in the y direction, type Ib beams, aligned in the x direction and type II beams that run diagonally across the unit-cell.

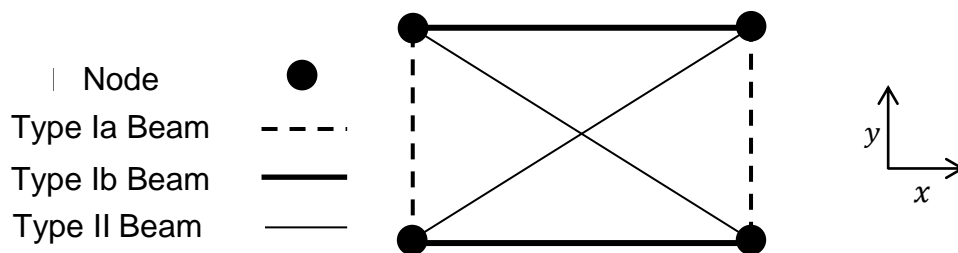


Figure 3.1 Repeatable unit-cell of rectangular symmetry with suggested beam types labelled

Considering the beam types simultaneously and altering their relative stiffness may allow for fine tuning of the elastic properties of the structure. However for this study, the beam types will be investigated in isolation as it is the origin of NLC behaviour that is of interest. From initial conceptual analysis, it is possible to discount both type I beam types from further consideration. Due to their orientation, these beams can only respond to hydrostatic loading by compressing on their own axes. This causes contraction of the unit-cell and only PLC will be observed.

The repeatable unit-cell of the type II beam structure investigated is shown in Figure 3.2 and contains two defining variables; the constituent beam length, L , and the internal angle, θ . Although not illustrated, the radius of the beam, r , is a third variable and determines I , the section moment of area of the beam and ϕ , the cross sectional area of the beam section equal to $\frac{\pi r^4}{4}$ and πr^2 respectively.

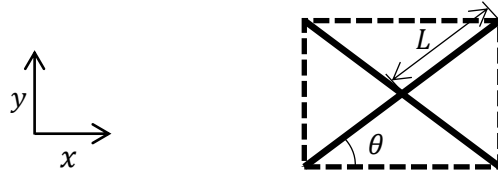


Figure 3.2 Repeating unit-cell of the two-dimensional type II beam structure (dashed lines represent the boundary of the unit-cell and solid lines denote the beams)

For both the analytical and FE studies, the following parameters are kept constant and are assigned the values shown;

- $E = 10\text{MPa}$ (Young's modulus)
- $L = 0.1\text{m}$ (length of beam)
- $r = 0.005\text{m}$ (radius of beam section)

3.5 Analytical Modelling of 2D Type II Beam Structure

3.5.1 Introduction

An analytical model for linear compressibility is determined by simulating a hydrostatic load and not by calculating the elastic compliances separately. By exploiting the symmetry of the structure and loads it is possible to reduce the model to a quarter so that only a single beam requires modelling. To simulate the beam in a large array, the beam is modelled with a cantilever boundary condition at Node J and a guided end boundary condition at Node K as illustrated in Figure 3.3. This guided end boundary condition applied at node K is used because, in a large array, the beam would be mirrored across the x and y axes delivering an equal and opposite moment, hence no rotation would be observed.



Figure 3.3 Type II primitive unit-cell and boundary conditions where the nodes have been labelled

To determine the linear compressibilities of the system a hydrostatic force is applied and the subsequent strains on the structure calculated. This is carried out using the following steps;

- Forces acting in the x and y directions are deduced by relating them to the x and y dimensions of the primitive unit-cell (as a pressure is being simulated)
- Forces acting axially and transversely to the beam are resolved
- Bending and axial deflections are calculated
- These deflections are converted into x and y displacements
- Linear compressibilities in the x and y directions are equal to $\frac{dx}{dP}$ and $\frac{dy}{dP}$ respectively

3.5.2 Analytical Derivation

Primitive Unit-Cell and Dimensions

The two-dimensional model comprises a structure of crosses of variable length, L , and internal angle, θ (see Figure). The repeatable unit-cell is shown in Figure 3.4Figure (a) while Figure 3.4Figure (b) illustrates the primitive unit-cell after consideration of symmetry.

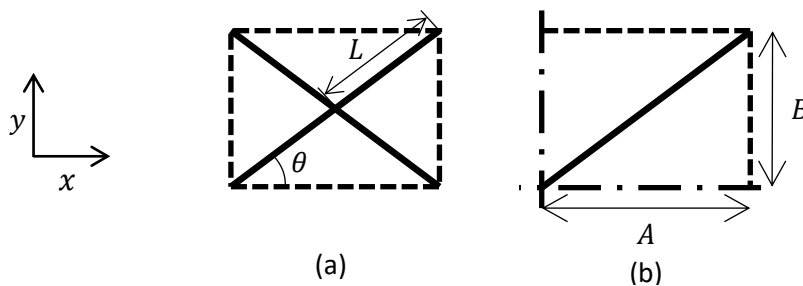


Figure 3.4 Repeating (a) and primitive (b) unit-cells of the two-dimensional type II beam structure

The dimensions of the primitive unit-cell, A and B , shown in Figure 3.4(b) are calculated using

$$A = \cos(\theta) L \tag{3.4}$$

and

$$B = \sin(\theta) L$$

3.5

Pressure Forces and Boundary Conditions

The beam is assumed to be within a large array that is undergoing hydrostatic loading as illustrated in Figure 3.5(a). The forces acting on the beam can therefore be assumed to be proportional to the length of the unit-cell (see Figure 3.5(b)) and act on the nodes of the beam that border the repeatable unit-cell. The forces acting on the primitive unit-cell are shown in Figure 3.5(c).

The beam is modelled with a cantilever boundary condition at node J and a guided end boundary condition at node K as indicated in Figure 3.6.

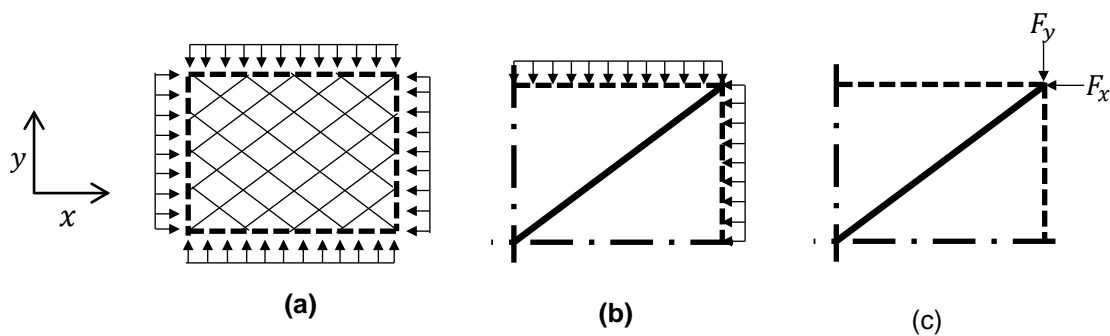


Figure 3.5 Illustration of pressure loading on (a) bulk material, (b) primitive unit-cell and (c) resulting forces on primitive unit-cell

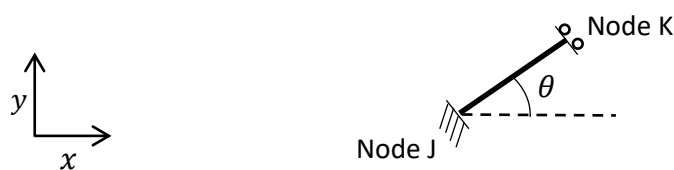


Figure 3.6 Type II primitive unit-cell, boundary conditions and node labels

F_x and F_y , the forces acting in the x and y directions respectively, are shown in Figure 3.5(c), and are calculated from the applied pressure, P , and the dimensions of the primitive unit-cell, previously defined. F_x and F_y are equal to

$$F_x = PB \quad 3.6$$

and

$$F_y = PA \quad 3.7$$

respectively.

Forces Resolved to Beam Axes

The forces acting axially upon and transversely to the beam, F_a and F_T respectively, shown in Figure 3.7, are resolved from F_x and F_y and are calculated using

$$F_a = F_y \sin(\theta) + F_x \cos(\theta) \quad 3.8$$

and

$$F_T = F_y \cos(\theta) - F_x \sin(\theta) \quad 3.9$$

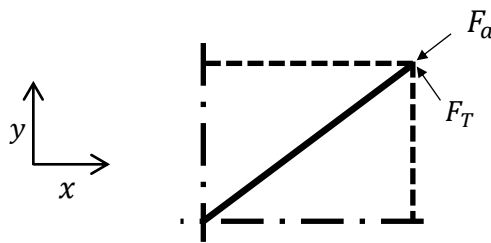


Figure 3.7 Forces resolved to local beam axes

Local Beam Deflections

Standard formulae and Euler beam theory are used to calculate the axial and transverse deflections of the beam, δ_A and δ_T respectively, which are shown in Figure 3.8. The deflections are calculated using

$$\delta_a = \frac{F_a L}{E\phi} \quad 3.10$$

and

$$\delta_T = \frac{F_T L^3}{12EI} \quad 3.11$$

where E is the material Young's Modulus, ϕ is the cross sectional area of the beam and I is the second moment of area of the beam.

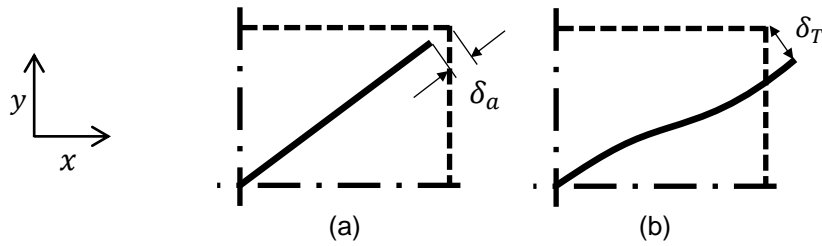


Figure 3.8 Illustration of (a) axial and (b) transverse deflections

Deflections Resolved to Global Coordinate System

Deflections appropriate to the global x and y axes, δ_x and δ_y , shown in Figure 3.9, are resolved as

$$\delta_x = [\delta_T \sin(\theta) - \delta_a \cos(\theta)] \quad 3.12$$

and

$$\delta_y = -[\delta_T \cos(\theta) + \delta_a \sin(\theta)] \quad 3.13$$

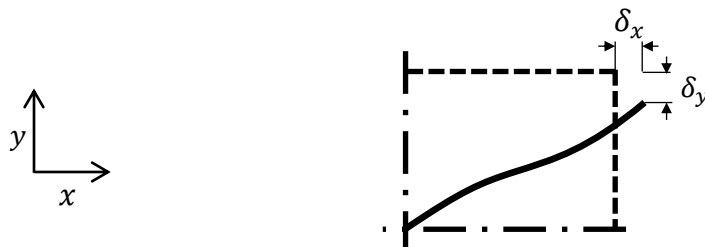


Figure 3.9 Deflection resolved to global coordinate system

Strains

Strains on the primitive unit-cell in the x and y directions, ϵ_x and ϵ_y , are calculated from the displacements and original dimensions of the unit-cell, previously defined, and are equal to

$$\epsilon_x = \frac{\delta_x}{A} \quad 3.14$$

and

$$\varepsilon_y = \frac{\delta_Y}{B} \quad 3.15$$

Linear Compressibility

Linear compressibility is calculated as previously defined using

$$\beta_x = \frac{\varepsilon_y}{P} \quad 3.16$$

and

$$\beta_y = \frac{\varepsilon_x}{P} \quad 3.17$$

Finally, by rearranging Equations 3.4-3.17, expressions for linear compressibility are found to be

$$\beta_x = \left[\frac{L^3 \tan(\theta) [1 - 2 \sin^2(\theta)]}{12EI} - \frac{L \sin(2\theta)}{E\phi} \right] \quad 3.18$$

and

$$\beta_y = - \left[\frac{L^3 \cot(\theta) [1 - 2 \sin^2(\theta)]}{12EI} + \frac{L \sin(2\theta)}{E\phi} \right] \quad 3.19$$

There are two terms in each case, the first term defines linear compressibility as a function of beam flexure and the second term defines linear compressibility as a function of axial compression.

3.5.3 Results

3.5.3.1 Modification of internal Angle θ

3.5.3.1.1 Absolute Linear Compressibility

The absolute linear compressibilities in the x and y directions (β_x and β_y respectively) from this model are plotted in Figure 3.10. It is predictable that the behaviour of the model is symmetric about 45° because the x and y dimensions swap over at this point. The negative values of compressibility are also coupled with a very large PLC in the perpendicular direction.

The maximum values of linear compressibility are observed when θ approaches 0° and 90° . This is because the beam is becoming aligned with one of the axes and the force acting to bend the beam becomes very large in comparison to the force acting to compress the beam axially. Also, because the beam is so aligned to a single axis, a small bending displacement represents a very large strain in the perpendicular axis, hence the compressibility becomes very large until $\theta=0^\circ$ or 90° where both compressibilities become very close to zero.

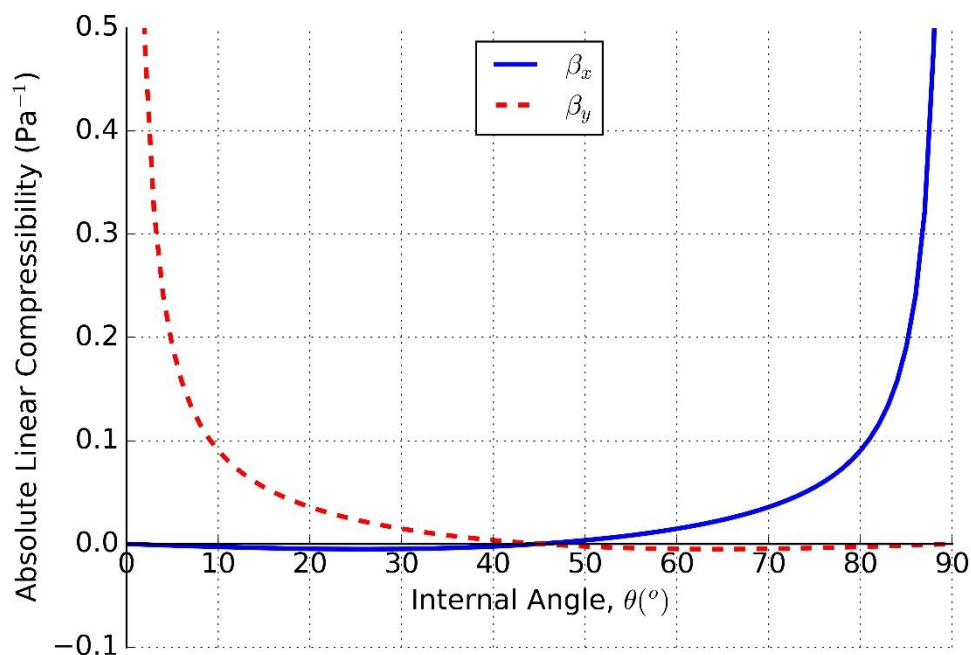


Figure 3.10 Absolute linear compressibility, in the x and y directions, of the two-dimensional type II beam structure

To improve readability of the negative values, the absolute linear compressibility of the two-dimensional rectangular symmetry has been re-plotted onto Figure 3.11 with the vertical scale altered. The maximum absolute NLC occurs when θ is equal to 25.9° and the equivalent angle 64.1° . This maximum value of NLC occurs at this angle, which is deemed to be a “sweet spot” due to two competing effects. As θ approaches 0, the component of hydrostatic force acting to bend the beam approaches a maximum and the bending deflection in the x direction approaches zero. When θ approaches 45° the proportion of the bending deflection that is creating positive strain on the x -axis approaches a maximum, however bending forces

approach zero. Therefore the maximum NLC will be observed when these two competing effects generate a maximum and that is when $\theta = 25.9^\circ$.

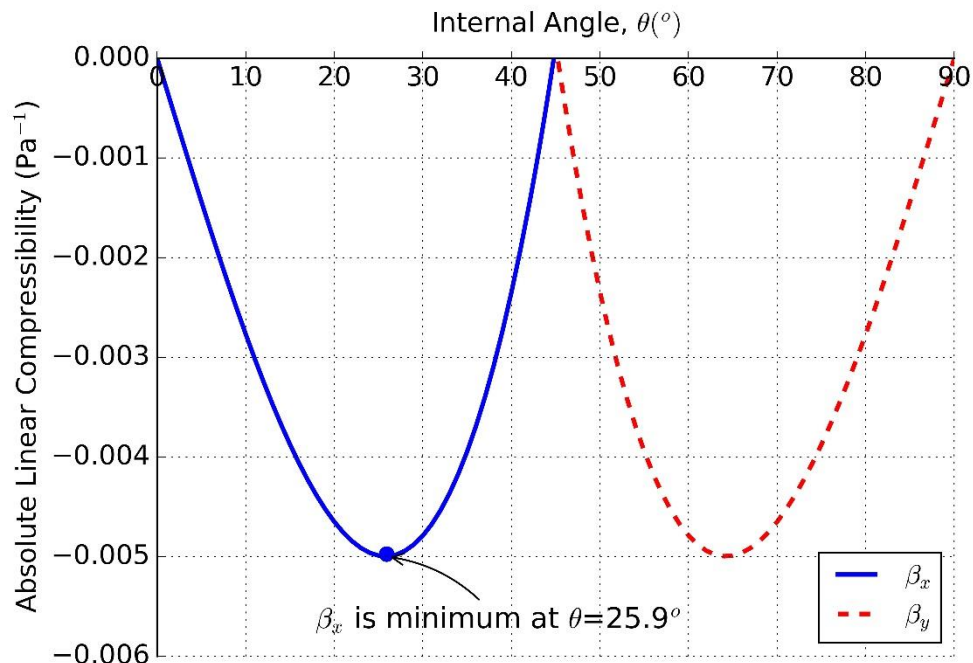


Figure 3.11 Absolute linear compressibility, in the x and y directions, of the two-dimensional type II beam structure (vertical scale modified to assist reading of negative values)

As stated previously, the methodology does not include an allowance for shear deformation within the beam as the beams are slender and deformation caused by shear is comparatively low. The inclusion of a shear term in formulae 3.18-3.19 would however act to diminish the magnitude of the NLC and if less slender beams were considered it would be necessary to make an allowance for the shear deformation.

3.5.3.1.2 Normalised Linear Compressibility

Normalised values for the two-dimensional rectangular structure are illustrated in Figure 3.12, which shows that peak values of the normalised linear compressibility occur when θ approaches 45° . When $\theta = 45^\circ$ the structure is square and isotropic, the compressibilities are positive and very small in magnitude and $\beta_{LN} = 0.5$. The large negative values of normalised compressibility occur because a large proportion of the applied force is acting

axially, hence deflections become very small and the absolute compressibilities, in both directions, reduce in value. The minimum normalised linear compressibility is defined as $\beta_{LNmin} = \frac{\beta_{min}}{\beta_x + \beta_y}$, and becomes $\beta_{Nmin} = \frac{\beta_x}{\beta_x + \beta_y}$ when $\theta < 45^\circ$. As θ approaches 45° , β_x remains negative but reduces in magnitude and β_y is small and positive hence $\beta_x > \beta_x + \beta_y$, which causes values of normalised compressibility to become very large. These very large values do however coincide with relatively small values of absolute linear compressibility and hence these large values of normalised linear compressibility could be difficult to recreate in reality. It is also noted that the maximum absolute linear compressibility that occurs at 25.9° coincides with a normalised compressibility of ≈ -0.3 .

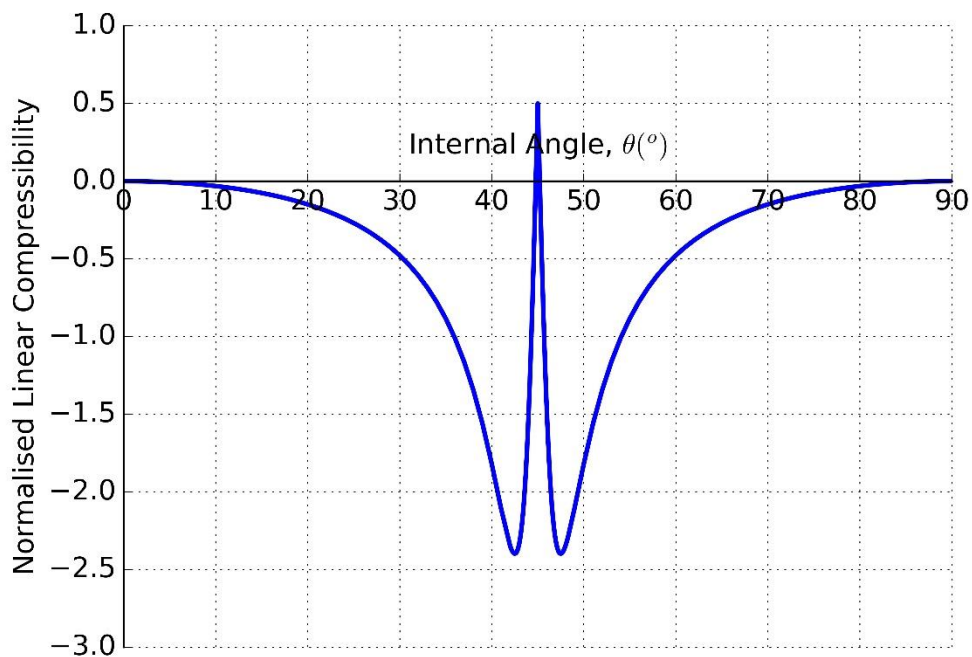


Figure 3.12 Minimum normalised linear compressibility in a two-dimensional type II beam structure

3.5.3.2 Modification of the Constituent Beam Aspect Ratio

3.5.3.2.1 Preamble

The magnitude of NLC is dependent upon the tendency of the beams to deform through flexure rather than axial compression. Therefore by decreasing the ratio between bending resistance, $\frac{L^3}{12EI}$, and the resistance to axial deformation, $\frac{L}{EA}$, by altering the ratio

between the radius and length of the constituent beams, the deformation of the beam can be altered so that it can be dominated by either flexure or axial compression.

Analyses presented in Section 3.5.3.1 set the beam aspect ratio (length/radius) to 20 in order to fix the ratio between the axial rigidity and the bending resistance. Results are presented in this section where the beam aspect ratio has been modified. This is carried out by altering the values of L, E and A in the analytical formulae defined in Section 3.5.

3.5.3.2.2 Results

Figure 3.13 shows the minimum absolute linear compressibility for a type II rectangular beam structure. It is evident from the figure that the magnitude of the absolute NLC increases as the radius reduces. The angle of θ on which the maximum NLC is observed does not change from 25.9° and it is as at this angle that values of compressibility are plotted. The results shown are for a fixed length of 0.1m and it is also noteworthy that values of normalised linear compressibility change only in detail as the ratio between β_x and β_y is not affected by this alteration within the structure.

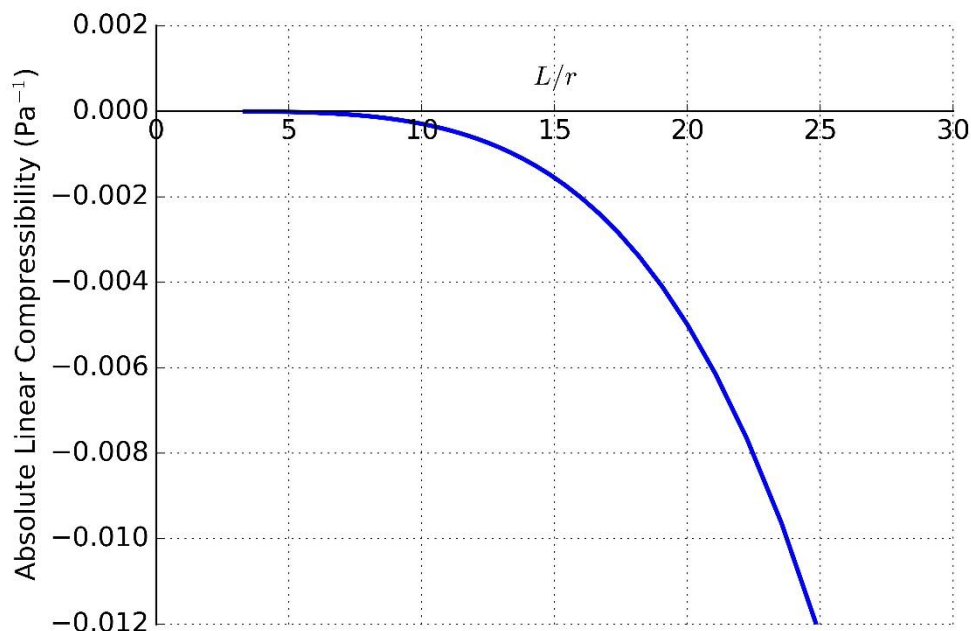


Figure 3.13 Minimum absolute linear compressibility of a type II beam structure in a rectangular symmetry for different values of L/r where $\theta = 25.9^\circ$

3.6 Finite Element Modelling of 2D Type II Beam Structure

3.6.1 Preamble

This section presents the use of FE modelling as an alternative method for determining the properties of the two-dimensional type II beam structure described in Section 3.4. This method determines the linear compressibility by calculation of extracted elastic compliances of the beam structures analysed.

3.6.2 Methodology

3.6.2.1 Geometry / Boundary Conditions / Loading Conditions

Modelling of crystal networks usually requires the use of periodic boundary conditions to simulate a very large array of the unit-cell. The FE code used does not have the capability to enforce such a boundary condition therefore a 11×11 array of the unit-cell shown in Figure 3.2 is modelled. An array of this size has been selected in order to suitably minimize edge effects while also allowing the model to be computationally viable (Horrigan et al., 2009).

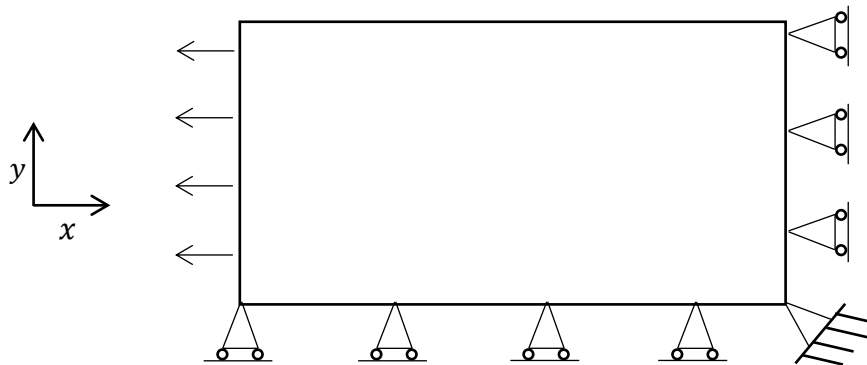


Figure 3.14 Illustration of boundary conditions used in FE modelling of beam structures

Figure 3.14 shows the boundary conditions imposed on the two-dimensional framework structure. The displacements of the nodes on the edges of the structure are restricted such that they can only move in the axial direction of that edge. The node in the bottom right corner of the array is fixed in both the x and y directions. A displacement causing a strain of 0.001% is applied in the direction indicated in the figure. The resulting

displacements are then extracted from the central unit-cell so as to mitigate any edge effects. Each model is also loaded in the y direction in order for all the necessary elastic compliances to be extracted. No efforts have been made to determine the shear compliances as they are not required to calculate compressibility.

3.6.2.2 Mesh Convergence

The structure is modelled using B22 (beam elements that are two-dimensional and are second-order .i.e have a mid-point polynomial node) finite elements. The dependency of the calculated elastic compliances and linear compressibility on mesh density for the two-dimensional type II beam structure where $\theta = 15^\circ$ are shown in Figure 3.15. Because it is only small scale elastic bending that is being modelled, suitable results can be gained by using a single element per beam as Figure 3.15 shows that the calculated elastic compliances are not sensitive to the number of elements used. Previous studies (Ghosh and Kumar, 1997) have also used a single element when modelling individual members within civil frame structures. However, for the duration of this study each beam is divided into 20 elements as this is not computationally limiting.

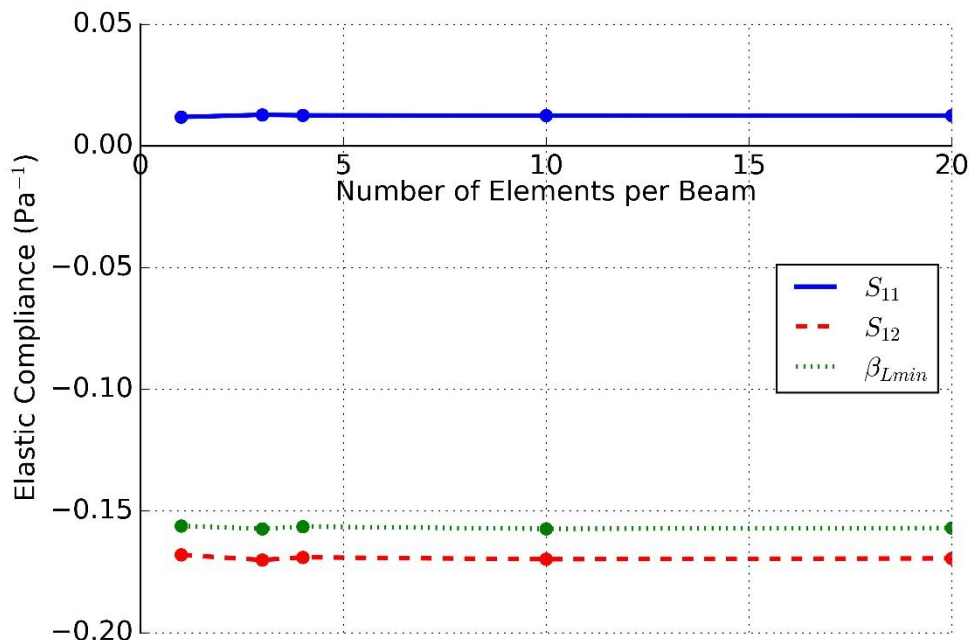


Figure 3.15 Sensitivity of the calculated elastic compliances and linear compressibility to mesh density of a two-dimensional type II beam model where $\theta = 15^\circ$

3.6.2.3 Python Scripting

Due to the high number of actions necessary within ABAQUS to assemble the geometries required, an automated system was implemented using the python scripting language. A script was written that would create, rotate and place the beams in the correct orientation dependent upon user defined requirements. Models were created and run for a user defined variation in the angle, θ , and the displacements from the loaded unit-cell were written to an output file for manual post processing.

3.6.3 Results

Results gained using this method are within 0.01% of those calculated using the analytical methodology. This methodology does however calculate the required elastic compliances of the unit-cell separately. These values are plotted in Figure 3.16. $S_{11} - S_{12}$ is also plotted as this is equal to the linear compressibility in the x direction. The method shows that the maximum NLC occurs at 25.9° as this is the point at which there is the largest absolute difference between S_{11} and S_{12} and hence agrees fully with the analytical methodology.

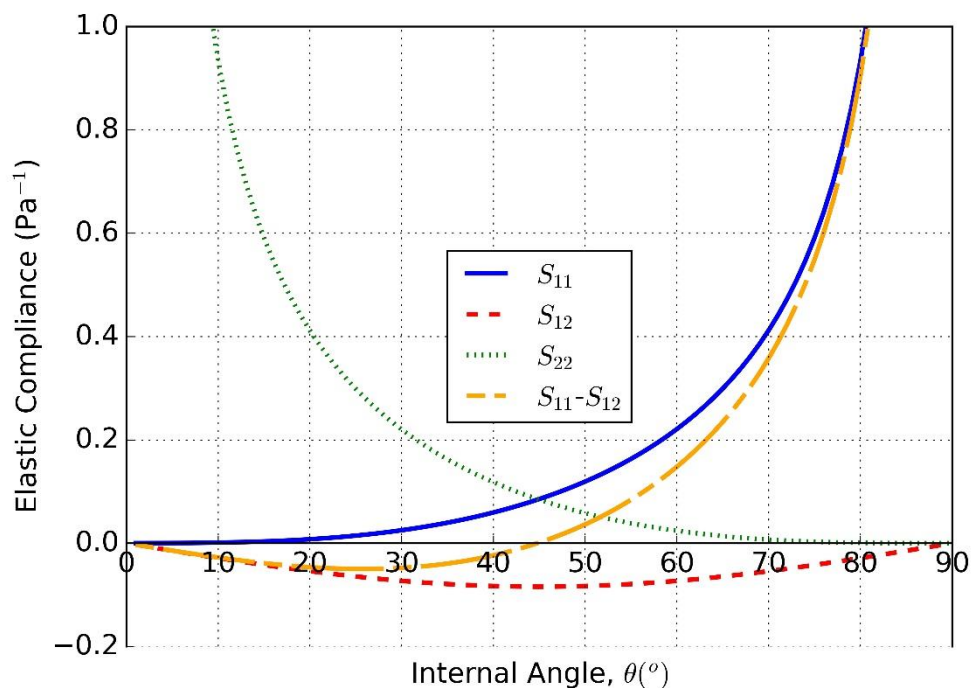


Figure 3.16 Elastic compliances of the two-dimensional type II beam structure for different values of θ

3.7 Conclusions from analysis of 2D “wine-rack”

This study shows that NLC is evident within two-dimensional beam structures where only type II beams are present. The absolute value of NLC can also be tailored in these structures by altering the angle θ which defines the unit-cell. Due to competing effects maximum values of NLC occur when $\theta = 25.9^\circ$ and normalised values of NLC become a maximum when θ approaches 45° . The magnitude of NLC can also be increased by increasing the L/r ratio of the constituent beam. Doing this, increases the ratio between the resistance to axial deformation and the bending resistance and therefore increases the tendency of the beam to bend rather than axially compress. This conclusion is also relevant to the exploration of further NLC crystalline systems, as chemical bonds that have greater axial stiffness with respect to rotational stiffness could be more likely to exhibit NLC, assuming the geometry is also suitable for NLC to present. It is important to note that the structures analysed in this chapter are heavily idealised and are not intended to imitate directly the deformation of real materials. The models do however show the origin of the NLC mechanism and also show how the absolute and normalised NLC values are sensitive to the internal angle. It is also concluded that the most basic way of representing an NLC mechanism is not necessarily the wine rack, but a beam rotating rigidly under some kind of resistance. This is illustrated in Figure 3.17, which shows that for an arbitrary rotation of a beam $\delta_y > \delta_x$.

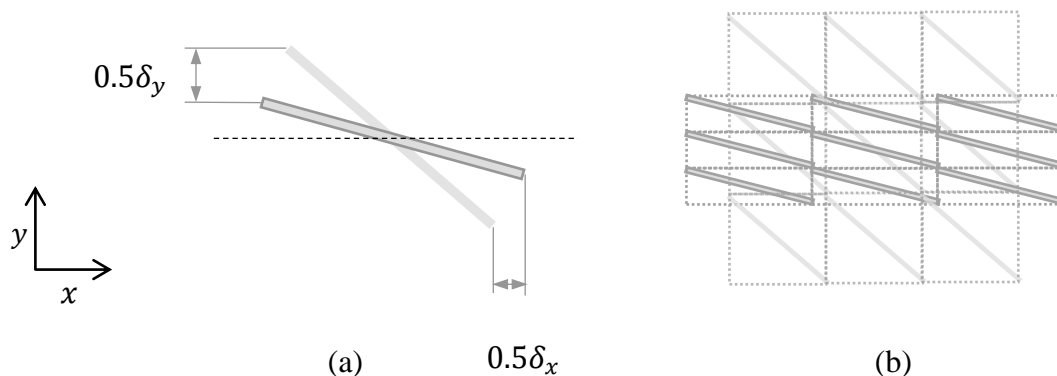


Figure 3.17 NLC visualised by rotation of a rigid beam as a (a) single unit-cell, and a (b) 3×3 array

With respect to discovering real materials, it can also be concluded that materials that have any bias toward deforming in this way are possible candidates for having NLC.

3.8 NLC in Common Engineering Materials

3.8.1 Introduction

The articles published on the subject of NLC to date are mainly concerned with molecular structures and theoretical frameworks while very little attention has been given to common engineering materials. This section documents the discovery of NLC in a number of common engineering materials. Based on the work reported in previous section of this chapter regarding 2D framework structures, Section 3.8.2 proposes three conditions that a potential NLC material must fulfil before further analysis is carried out. The new NLC materials discovered using this guidance are then reported in Section 3.8.3 along with a description of the NLC mechanism. The conclusions of this study are stated in Section 3.8.4 and the key data related to these materials is also listed in Appendix D where appropriate. This chapter considerably expands on an article published in 2015 (Miller et al., 2015)

3.8.2 Guidance for Identifying NLC materials

After careful consideration of the idealised framework structures analysed in Chapters 3-5, it has been recognised that for a material to have NLC, as a consequence of the “wine-rack” mechanism, the following conditions must be fulfilled.

- The material must be partially composed of strand-/chain-like structures
- A degree of alignment must exist between the strands/chains (although complete alignment will not lead to NLC)
- A form of crosslinking/interaction between the strands/chains must be present.

Using these three conditions as a guide, it is possible to conduct a focussed literature search with the purpose of identifying engineering materials that exhibit NLC. The criteria suggest that materials types that contains fibres or aligned molecules could have NLC.

3.8.3 Materials Identified

3.8.3.1 Drawn Polymers

Polymers comprise long molecular chains that interact with one another. The process of drawing or extruding the polymer imparts a degree of directionality onto the material by aligning the polymer chains. This process changes the material from an isotropic material described by only three elastic compliances, to a tetragonal structure requiring five elastic compliances. The elastic compliance matrix describing such a drawn structure is

$$\begin{bmatrix} S_{11} & S_{12} & S_{13} & - & - & - \\ S_{12} & S_{11} & S_{13} & - & - & - \\ S_{13} & S_{13} & S_{33} & - & - & - \\ - & - & - & S_{44} & - & - \\ - & - & - & - & S_{44} & - \\ - & - & - & - & - & S_{66} \end{bmatrix} \quad 3.20$$

Noting that in this case, S_{33} represents the compliance relating strain to stress in the drawn direction. The material is also assumed to be isotropic across the plane perpendicular to the drawn direction i.e. that $S_{11} = S_{22}$ and $S_{23} = S_{13}$.

Drawn polyvinyl chloride and polypropylene have been identified as having NLC on the axis of drawing via analysis of their published elastic constants. In both cases the elastic constants were deduced using ultrasonic wave velocity measurements and the article dedicated to polypropylene (Chan et al., 1978) has also included elastic compliances for different drawing ratios (see Figure 3.18).

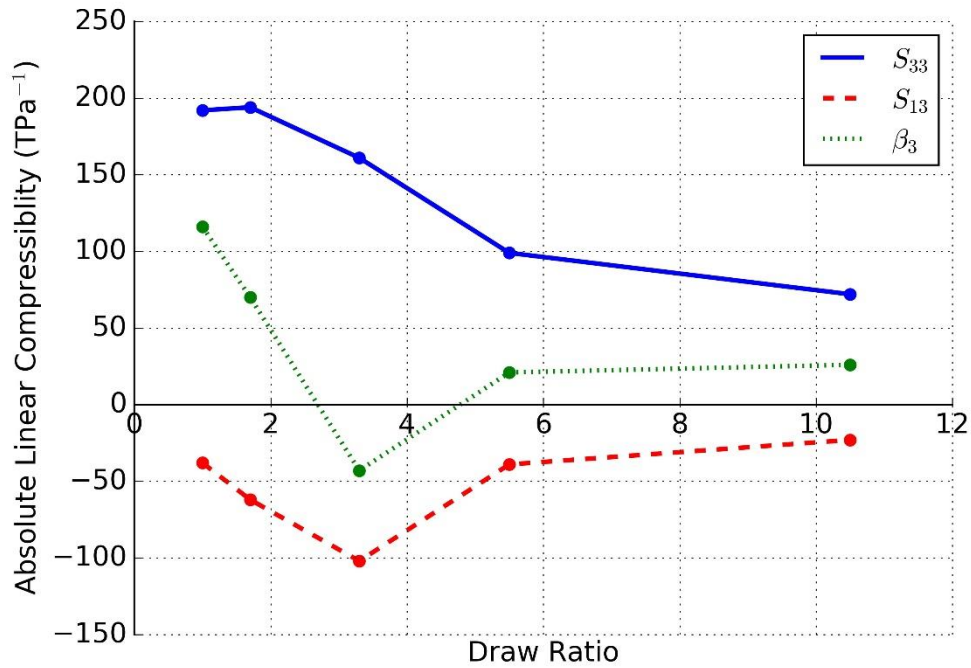


Figure 3.18 Elastic compliance and calculated linear compressibility of drawn polyethylene for different values of draw ratio (data from Chan et al., 1978)

NLC is only observed for a draw ratio of 3.3. For larger draw ratios the linear compressibility returns to positive values. This is due either to inaccuracies in the elastic constant measurement or to the fact that for larger draw ratios, the degree of alignment is too great and has passed the optimum for the purposes of achieving a large NLC. This would make sense as the beam model analysed in Chapter 2 concluded that the maximum magnitude NLC occurs when the misalignment between beams is approximately 26° and greater levels of alignment diminished the absolute magnitude of the NLC. Results showing NLC in drawn polyvinyl chloride have also been published, although results are not as detailed as those for polyethylene. Elastic constants have only been reported for a draw ratio of 3.3 (Rawson and Rider, 1974). The NLC mechanism in this structure occurs on the nano-scale and is dependent upon the degree of alignment and attraction between chains, therefore opening up this field for additional research.

3.8.3.2 Carbon Fibre Laminate

The results for carbon fibre have been obtained using a published computational program that calculates the bulk material properties of a carbon fibre lamina lay-up (Roylance, 1996). The program takes the properties of each layer as input and calculates bulk material properties based on specified stack orientations.

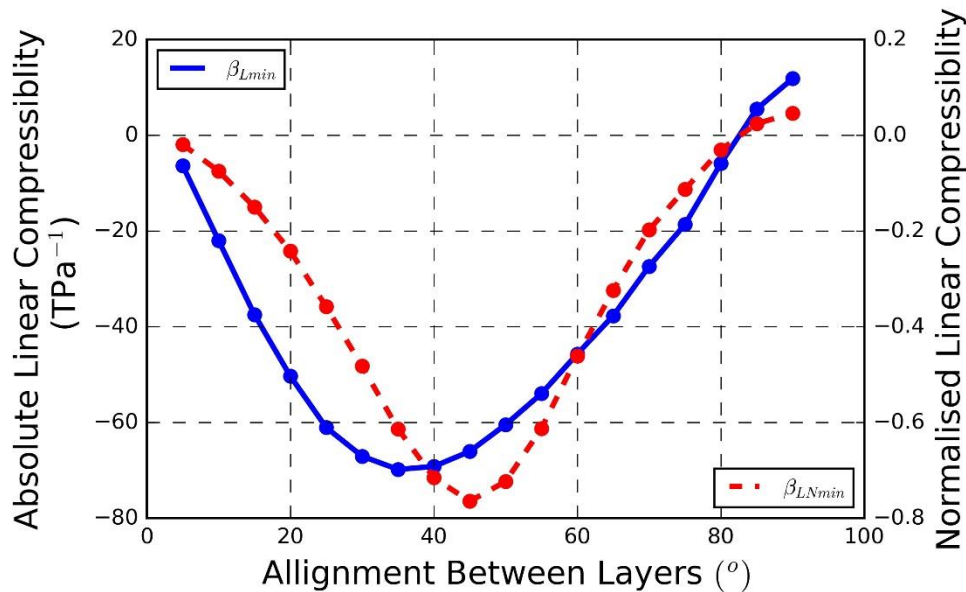


Figure 3.19 Linear compressibility of CFRP panels of varying layer alignment calculated using plate program

The three conditions listed in section 6.2 are fulfilled by the presence of highly directional laminae that interact with one another via the friction between the layers. The material properties of the constituent laminae were chosen as follows:

- $E_x = 230GPa$
- $E_y = 6.6GPa$
- $\nu_{xy} = 0.25$
- $G_{xz} = G_{yz} = 6.6 GPa$

where E_x is the stiffness of the lamina in the fibre direction, E_y is the stiffness of the lamina in the transverse direction, ν_{xy} is the Poisson's ratio of the lamina and G represents the xz and yz components of shear modulus. Note that x is the fibre axis, y is the transverse axis and z is the stack axis.

The resulting absolute and normalised values of linear compressibility are illustrated in Figure 3.19 for different lamina alignments. The peak in absolute NLC is at 35° and does not coincide with that from the theoretical calculations presented in Chapters 3-4 at ~26°. This is likely due to the interaction between the layers not being as simple as the analytical analysis presented in Chapters 3-4 assume. The fibres in a real material are not joined to one another at regular intervals and the points at which they are joined are not infinitely stiff. This means the fibres may move relative to each other. The amount by which they can move relative to each other compared to how much they deform locally (the rigidity of the interactions between the neighbouring fibres) will affect the internal angle at which a “sweet spot” is observed. The resulting normalised NLC peaks at 45° similarly to the models presented in Chapters 3-4 as a degree of relative incompressibility is being approached. However, because the out-of-plane stiffness is not a user-defined variable in these analyses and is instead calculated internally by the program, these models have an extra degree of complexity involved that is not considered in Chapters 3-4. For this reason, further analysis should be conducted as well as some experimental testing to substantiate these findings.

3.8.3.3 Wood

Different species of wood are selected for some structural applications on the basis of their favourable stiffness per unit mass. A basic representation of the structure that most hardwoods conform to is shown in Figure 3.20. The axis system present in Figure 3.20 is based on that of a tree where the axial direction is aligned with the direction of tree growth or the axis of the trunk.

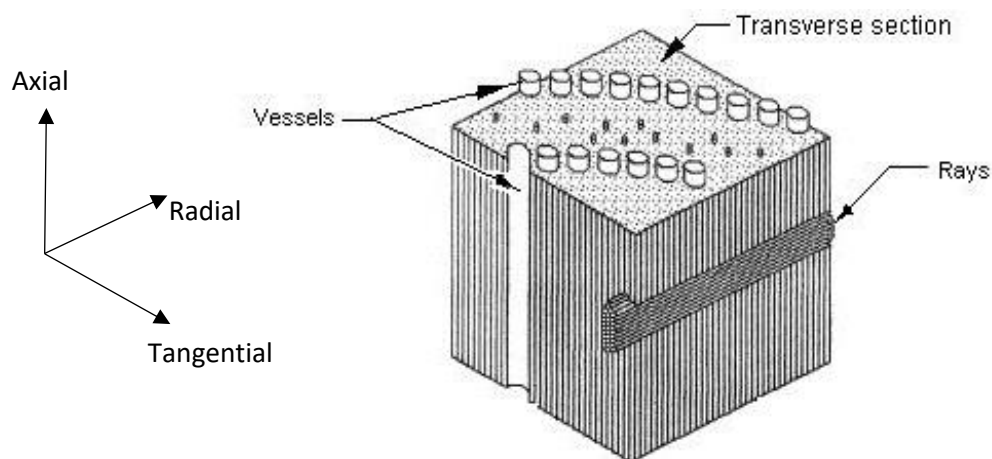


Figure 3.20 Section diagram illustrating the structure of hardwood (Clifford, 2016)

The structure is made up of vessels and rays which transport nutrition axially and radially. Fibres running parallel to the vessels that provide rigidity to the structure are not shown. The structure fulfils all of the conditions previously stated for it to be considered as a potential NLC material, as the fibres create a degree of alignment and the presence of the rays causes them to be imperfectly aligned and to have points about which they can pivot. A literature search of the published elastic constant data for 76 different wood samples has been conducted. The maximum and minimum linear compressibilities have been determined using Elam (Marmier et al., 2010a) and data from the four species of wood determined to have NLC are listed in Table 3-1, along with calculated minimum and maximum linear compressibilities. All elastic constant data assume that the woods conform to orthorhombic symmetry, where the 1, 2 and 3 directions represent the radial, transverse and axial axes of the wood as shown in Figure 3.20.

Wood Species	Components of Compliance Matrix using Voight Notation (TPa ⁻¹)									Linear Compressibility (TPa ⁻¹)	
	S ₁₁	S ₂₂	S ₃₃	S ₄₄	S ₅₅	S ₆₆	S ₁₂	S ₁₃	S ₂₃	β _{Lmin}	β _{Lmax}
Ash ^(Earmon, 1948)	609.8	1030.9	66.7	1639.3	1162.8	4000	-402.4	-35.3	-43.3	-11.9	585.2
Aspen ^(Bodig, 1973)	1345.4	3786.9	127.4	2238.2	1663.3	12036	-1711.7	-58.4	-25.7	-424.7	2049.5
Oak ^(Guitard, 1987)	478.5	869.6	57.1	1492.5	1000	4545.5	-324.7	-23	-39.2	-5.1	505.7
Walnut ^(Earmon, 1948)	840.3	1587.3	89.3	1428.6	1041.7	4347.8	-605	-43.8	-56.3	-10.8	926

Table 3-1 Material Properties of wood taken from various data sources with calculated linear compressibilities

Results should however be treated with some caution as the elastic properties of wood can vary not only between different specimens but also between samples from the same specimen. Variability of the elastic properties can be caused by: the drying process used, the environment in which tree is grown, residual stresses caused by wind loading, the grain pattern of the sample, knots within the sample and the radial position within the tree from which the sample was taken.

3.8.3.4 Machine Paper

Broadly speaking, paper is manufactured from wood via a pulping and pressing process which allows the individual wood fibres to remain partially intact. The pressing/rolling part of the process then imparts a degree of alignment between the fibres therefore allowing paper to satisfy all requirements for it to be worthy of further investigation.

There is predictably little consistency in the material properties of paper as there is a large dependency on the raw material used, the methodology applied and the specific set-up of the manufacturing equipment on any particular day. Literature which fully describes the compliance matrix of the material does not appear often, although compliances have been reported for paper where ultrasonic methods have been used on a sample of milk carton stock (Mann et al., 1979). From the published data it is calculated that the minimum and maximum values of linear compressibility are $\sim -175\text{TPa}^{-1}$ and $\sim 1520\text{TPa}^{-1}$ respectively.

3.8.4 Conclusions

After analysis of the 2D “wine-rack” from which key findings are presented in Section 3.47, three common engineering materials have been identified as having NLC imparted to them by their manufacturing process. These are drawn polymers, carbon fibre laminates and machine paper. This research points to the potential for many more materials with NLC to be identified as any material that has a degree of alignment imparted onto it, is a suitable candidate for consideration. This research also shows that well established manufacturing processes could be tuned for the production and optimisation of NLC. Additionally, the discovery that certain woods can have NLC is an interesting one as it can be added to the list of biological NLC materials and because it is a commonly used engineering material and has numerous applications.

Little attention has so far been paid to the possible applications of NLC materials in the published literature. However as the property has now been identified in common engineering materials the possibility of industrial applications has an increased scope.

Chapter 4

Three-Dimensional NLC Structures

4.1 Introduction

This chapter forms a direct continuation of the work presented in the preceding chapter on two-dimensional framework structures that enable NLC. Similar methods are adopted here to ascertain the properties of beam structures in three-dimensional symmetries.

Three-dimensional symmetries are considered and are analysed using an expansion of the analytical methodology described in Chapter 3. The resulting normalised and absolute linear compressibilities of the beam structures corresponding to tetragonal and orthorhombic symmetries are presented and conclusions are drawn. The work on beam structures within a tetragonal symmetry presented in this chapter has been published in 2012 (Barnes et al., 2012).

4.2 Symmetries Explored

The aim of this chapter is to establish the basis of the mechanism that can allow NLC to be present in a three-dimensional structure. As cubic structures are of the highest symmetry and are, elastically, the simplest three-dimensional symmetry (as they can be described using the fewest number of unique elastic compliances), they are a logical starting point. The compliance matrix for a cubic symmetry is

$$\begin{bmatrix} S_{11} & S_{12} & S_{12} & - & - & - \\ S_{12} & S_{11} & S_{12} & - & - & - \\ S_{12} & S_{12} & S_{11} & - & - & - \\ - & - & - & S_{44} & - & - \\ - & - & - & - & S_{44} & - \\ - & - & - & - & - & S_{44} \end{bmatrix} \quad 4.1$$

Due to the symmetry of the compliance matrix, the compressibility cannot take a negative value. The linear compressibility of a cubic system is isotropic and is equal to $S_{11} +$

$2S_{12}$. A negative value of linear compressibility is not possible within a cubic symmetry as this would create a negative volume expansion.

Tetragonal, trigonal and hexagonal structures are, elastically, the simplest symmetries to allow NLC. This chapter looks at tetragonal frameworks, as they are simpler to derive expressions for and represent a logical progression from the two-dimensional rectangular symmetry analysed in Chapter 3. Following the analysis of tetragonal-based structures, orthorhombic-based structures are also analysed.

4.3 Methodology

Due to the almost exact matching of the results extracted using the finite element and analytical methodologies reported in the previous chapter, this chapter uses only analytical methodologies. Additionally, all of the assumptions listed in Section 3.2 remain in place.

4.4 Tetragonal Structures

4.4.1 Lattice Parameters and Compliance Matrix

A tetragonal unit-cell is a square of side length, A , extruded through a distance of length, C . This geometry is shown in Figure 4.1. This leads to the construction of the tetragonal compliance matrix shown as Equation 4.2.

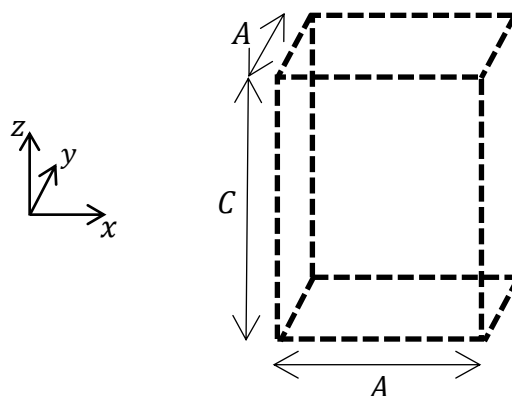


Figure 4.1 Tetragonal lattice parameters

$$\begin{bmatrix} S_{11} & S_{12} & S_{13} & - & - & - \\ S_{12} & S_{11} & S_{13} & - & - & - \\ S_{13} & S_{13} & S_{33} & - & - & - \\ - & - & - & S_{44} & - & - \\ - & - & - & - & S_{44} & - \\ - & - & - & - & - & S_{66} \end{bmatrix} \quad 4.2$$

The linear compressibility of a tetragonal structure with respect to elastic compliances can be described as

$$\beta_L = S_{11} + S_{12} + S_{13} - (S_{11} + S_{12} - S_{13} + S_{33})L_z^2 \quad 4.3$$

where L_z is the z component of a unit vector aligned to the axis on which linear compressibility is to be calculated. Maximum and minimum values of absolute NLC lie on one of the orthogonal axes and as such the extreme values are straightforward to calculate if the elastic compliances are known. The linear compressibilities in the x , y and z directions are described as

$$\beta_x = \beta_y = S_{11} + S_{12} + S_{13} \quad 4.4$$

and

$$\beta_z = S_{33} + 2S_{13} \quad 4.5$$

4.4.2 Unit-Cell

4.4.2.1 Preamble

Similarly to the analysis conducted in the previous chapter, beam structures are considered that correspond to different levels of interaction. Here, nearest (simple tetragonal), second nearest (face-centred tetragonal) and third nearest (body-centred tetragonal) neighbours are considered separately.

4.4.2.2 Beam Types

Similarly to the previous chapter, a simple array made up of type Ia and type Ib beams as illustrated in Figure 4.2 is immediately discounted as compression of the structure will not result in NLC, as hydrostatic pressure will result solely in axially compressive forces being present in the beams locally.

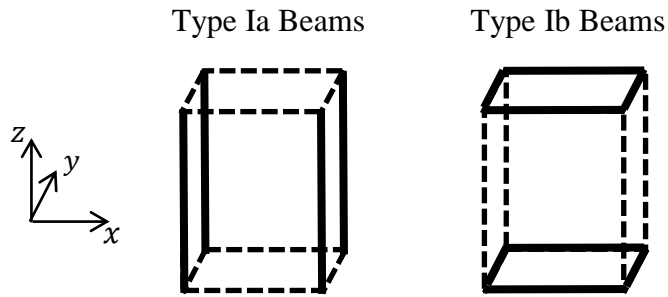


Figure 4.2 Type I beam arrangement within a tetragonal symmetry

A type II beam structure is considered, and represents a face-centred tetragonal structure. The type II beams have been split into two classes; type IIa and type IIb as shown in Figure 4.3.

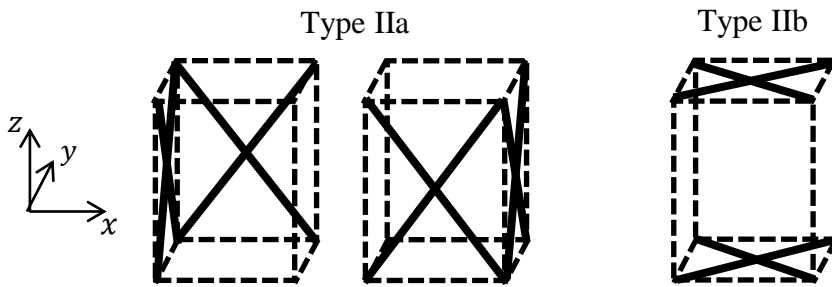


Figure 4.3 Type II beam arrangement within a tetragonal symmetry

A type III structure is also considered and is pictured in Figure 4.4, which is analogous to a body-centred tetragonal arrangement.

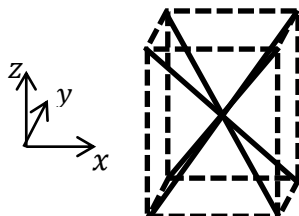


Figure 4.4 Type III beam arrangement within a tetragonal symmetry

4.4.3 Results

4.4.3.1 Initial Findings

Initial analysis of the type II beam structure found that the type IIb beams resist deformation under hydrostatic loading via axial compression and do not bend due to their square arrangement. This stiffens the structure in all directions and for the structure to deform, these beams must be removed. Removal of the type IIb beams from the type II beam structure causes the type II and type III beam structures to become equivalent (one is a 45° rotation of the other around the z direction (see Figure 4.3-4.4)). Results are therefore only presented for the type III structure.

4.4.3.2 Analytical Formulae

The derivation of the analytical formulae defining the linear compressibility of the type III beam structure is documented in Appendix B. The repeatable and primitive unit-cells on which the derivation is based are shown in Figure 4.5(a) and Figure 4.5(b) respectively. The angle that defines the unit-cell, μ , is also shown.

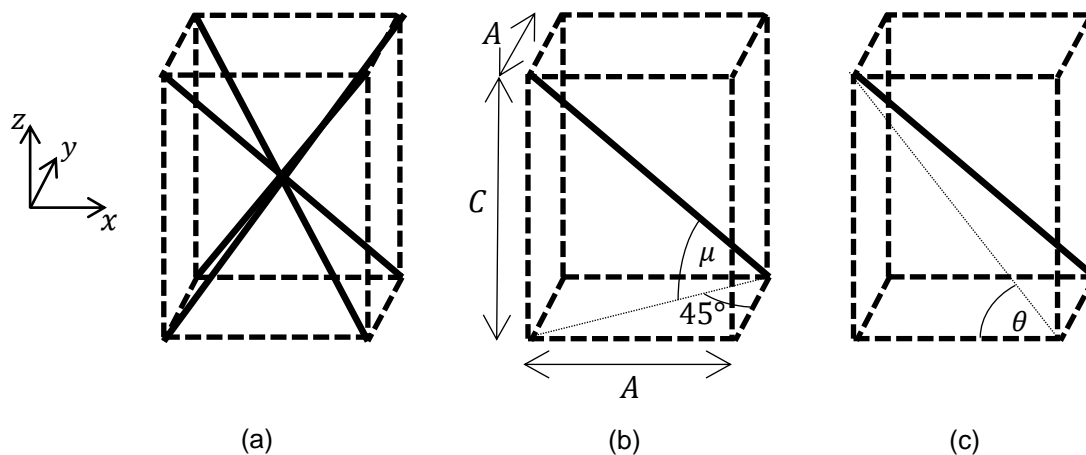


Figure 4.5 Repeating (a) and primitive (b and c) unit-cells for a 3D tetragonal beam structure

The formulae for absolute linear compressibility in the x , y and z directions are

$$\beta_x = \beta_y = -\frac{[3L^2 \sin(\mu) \cos^2(\mu)]}{2E\phi} + \frac{[-L^4 \cos^2(\mu)\sin(\mu) + 2L^4 \sin^2(\mu)]}{24EI} \quad 4.6$$

and

$$\beta_z = -\frac{[3 L^2 \sin(\mu) \cos^2(\mu)]}{2E\phi} + \frac{[-L^4 \cot(\mu) \cos^3(\mu) + 2L^4 \sin(\mu) \cos^2(\mu)]}{24EI} \quad 4.7$$

Results are presented with respect to the angle θ , shown in Figure 4.5(c), which is the angle the beam makes with the xy plane projected on to the xz plane. θ is directly related to μ by $\tan(\theta) = \sqrt{2} \tan(\mu)$. This representation is chosen because this angle is more logically linked to the aspect ratio of the unit-cell and allows easier comparison with the 2D rectangular results.

4.4.3.3 Absolute Linear Compressibility

The absolute linear compressibility for a type III beam structure is plotted in Figure 4.6 and Figure 4.7. The maximum value of β_z occurs as θ approaches 0° . This is partly because the C parameter of the unit-cell (Figure 4.5(b)) becomes very small and also because the resultant hydrostatic force is approaching a state where it is acting almost entirely in the negative z direction. The maximum values of β_x and β_y occur as θ approaches 90° as the beams are becoming closely aligned with the z -axis and similarly the A and B parameters become very small and the hydrostatic force acts to lengthen the unit-cell. The maximum is however much smaller than the maximum for β_z because the resultant hydrostatic force approaches zero as the area of the faces perpendicular to the x and y axes (i.e. the area, AC) approach zero as θ approaches 90° .

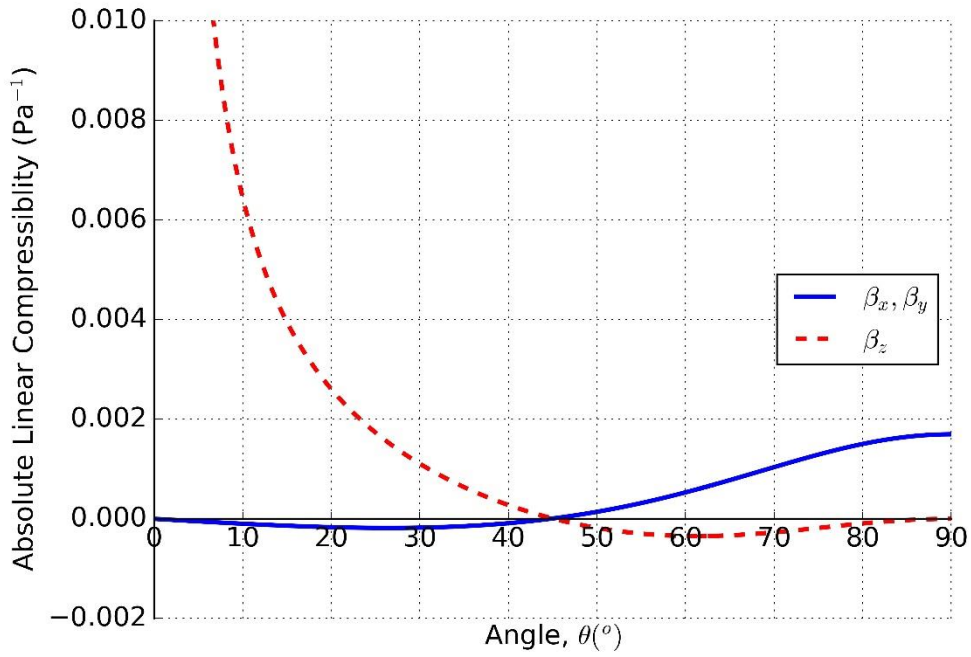


Figure 4.6 Absolute linear compressibility for a type III beam structure in a tetragonal symmetry

Figure 4.7 shows that the absolute linear compressibility is minimum for an internal angle of $\theta = 61.2^\circ$, whereas a local minimum is observed at 26.6° when $\theta < 45^\circ$, i.e. when the unit-cell has an aspect ratio less than 1.

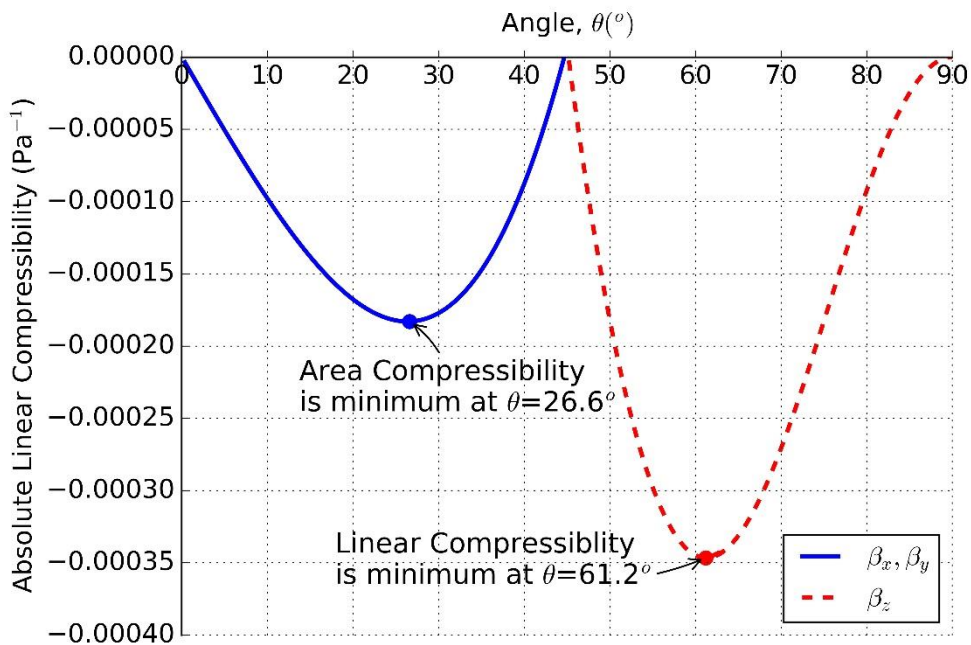


Figure 4.7 Absolute linear compressibility for a type III beam structure in a tetragonal symmetry (vertical scale modified to assist reading of negative values)

This data has been replotted in Figure 4.8 where the linear compressibility has been plotted against the aspect ratio of the unit cell, calculated as C/A (see Figure 4.5(b)). This shows that maximum NAC occurs at an aspect ratio of approximately 0.5 and the maximum NLC occurs at an aspect ratio of approximately 1.8.

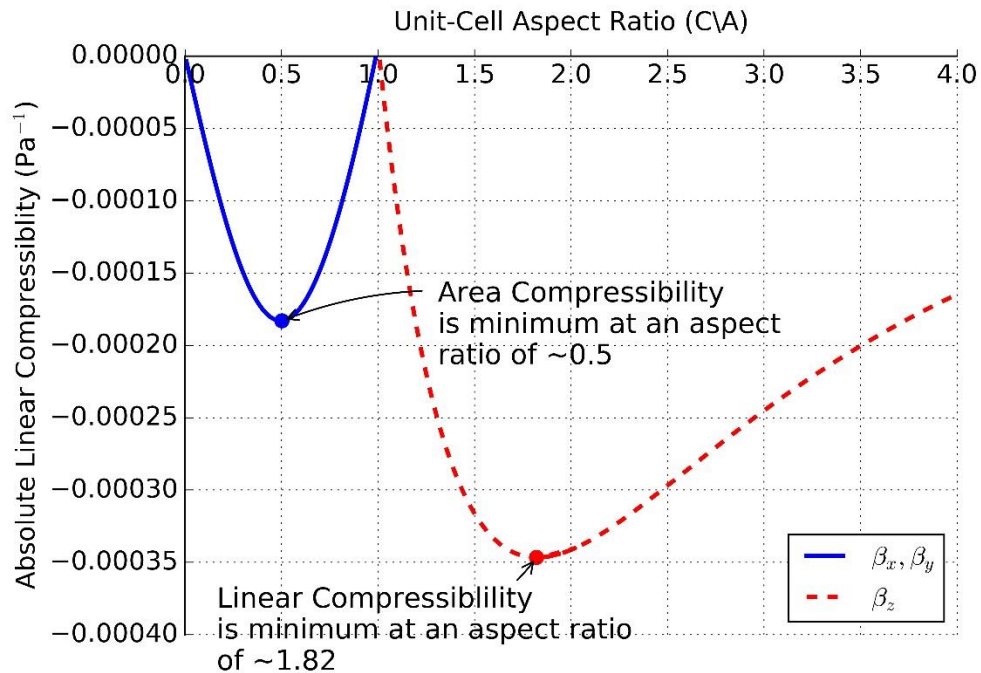


Figure 4.8 Absolute linear compressibility for a type III beam structure in a tetragonal symmetry (vertical scale modified to assist reading of negative values and the horizontal axis changed to show the aspect ratio of the unit-cell)

Also, as $\beta_x = \beta_y$, when $\theta < 45^\circ$, both these values are negative, meaning NAC is observed in the xy -plane as illustrated in Figure 4.9. Conversely, when $\theta > 45^\circ$, NLC acting on the z direction is observed.

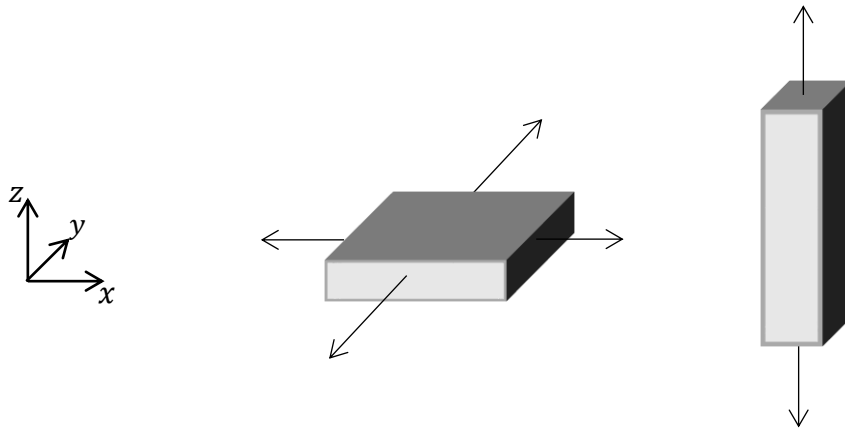


Figure 4.9 Direction of NLC in a tetragonal beam structure for unit-cell aspect ratios below 1 (left) and above 1 (right)

Even though the observed maximum NAC is smaller than the maximum NLC (approximately half) it should be noted that the NAC acts across the xy plane and is also restricted to being less than half the maximum linear compressibility whereas the maximum NLC is restricted to being less than the maximum linear compressibility in order to ensure the unit-cell reduces in volume when hydrostatically compressed. It should also be noted that the β_{Amin} when $\theta = 61.2^\circ$ is approximately $2\beta_{Lmin}$ when $\theta = 26.6^\circ$.

4.4.3.4 Normalised Linear Compressibility

The normalised minimum linear compressibility is shown in Figure 4.10. As expected, a value of $1/3$ is observed for a cubic symmetry ($\theta = 45^\circ$) as the linear compressibility becomes isotropic. Large values of normalised NLC are observed similar to the results shown in Chapter 3 for the two-dimensional beam structure, as $\beta_x + \beta_y + \beta_z \ll \beta_x, \beta_y, \beta_z$ when θ approaches 45° . Normalised linear compressibility is not symmetrical about 45° because the maximum and minimum linear compressibilities are not symmetrical about 45° . Figure 4.6 shows the difference between the maximum and minimum compressibilities and illustrates why the values of normalised compressibility are much larger in magnitude when $\theta > 45^\circ$.

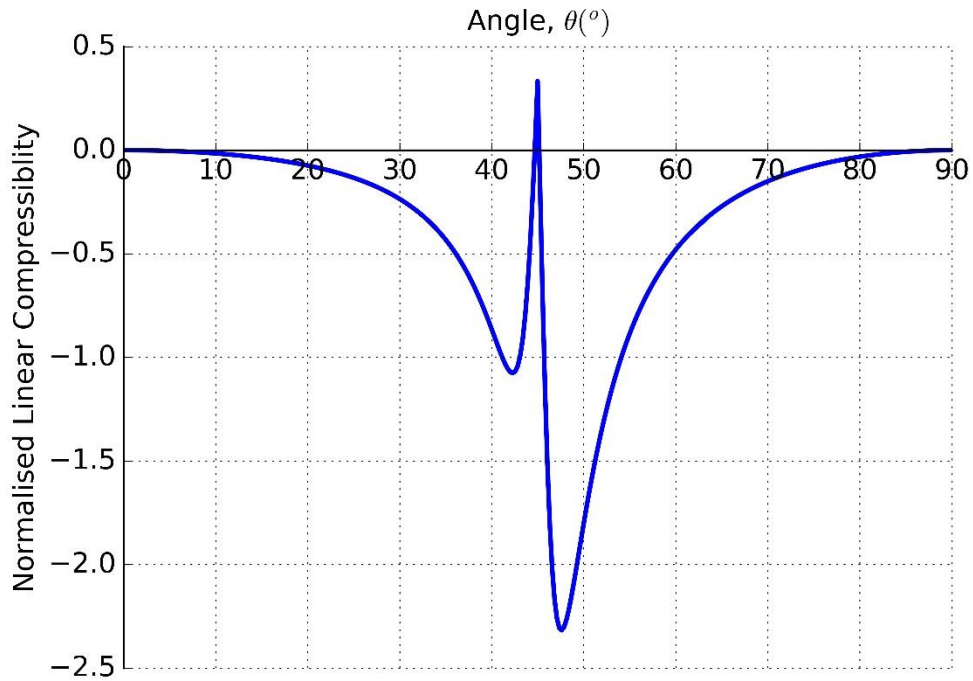


Figure 4.10 Minimum normalised linear compressibility of a type III beam structure in a tetragonal symmetry

4.5 Orthorhombic Structures

4.5.1 Lattice Parameters and Compliance Matrix

An orthorhombic unit-cell is described by three unique parameters as illustrated in Figure 4.11. This increase from the two required to describe a tetragonal unit-cell provides a logical step to increase the complexity of the analysis.

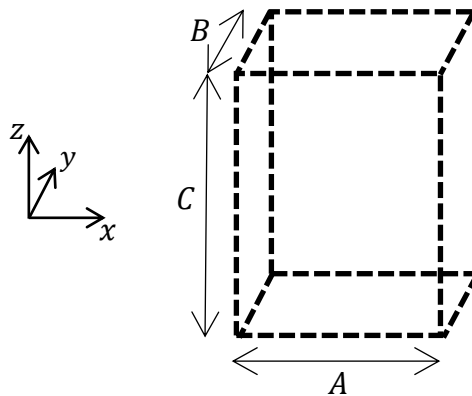


Figure 4.11 Orthorhombic lattice parameters

The orthorhombic compliance matrix is shown as Equation 4.8. The number of unique compliances required to describe the elastic behaviour of the unit-cell has also increased from the six, needed for tetragonal, to nine.

$$\begin{bmatrix} S_{11} & S_{12} & S_{13} & - & - & - \\ S_{12} & S_{22} & S_{23} & - & - & - \\ S_{13} & S_{23} & S_{33} & - & - & - \\ - & - & - & S_{44} & - & - \\ - & - & - & - & S_{55} & - \\ - & - & - & - & - & S_{66} \end{bmatrix} \quad 4.8$$

The presence of these additional constants has made it possible for the linear compressibility to be different in each of the three principal axes. The equation for linear compressibility in the direction of a unit vector of components, L_x , L_y , and L_z , is

$$\beta_L = (S_{11} + S_{12} + S_{13})L_x^2 + (S_{22} + S_{21} + S_{23})L_y^2 + (S_{33} + S_{13} + S_{23})L_z^2 \quad 4.9$$

This results in the following equations for linear compressibility in the three principal directions:

$$\beta_x = S_{11} + S_{12} + S_{13} \quad 4.10$$

$$\beta_y = S_{22} + S_{12} + S_{23} \quad 4.11$$

and

$$\beta_z = S_{33} + S_{13} + S_{23} \quad 4.12$$

4.5.2 Unit-Cell

Due to the equivalence of type IIb and type III structures as shown by the results from the tetragonal symmetry modelling, only type III structures are investigated for orthorhombic symmetries. This arrangement is illustrated in Figure 4.12. The length of the beam is fixed and the dimensions of the unit-cell are varied by altering the angles μ and α .

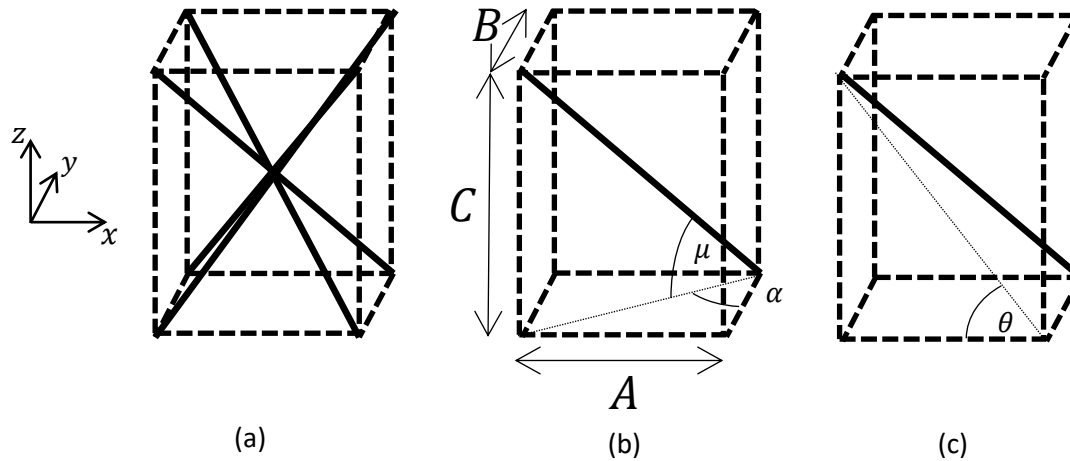


Figure 4.12 (a) Type III beam arrangement in an orthorhombic symmetry (repeatable unit-cell)
 (b) Type III beam arrangement in an orthorhombic symmetry (primitive unit-cell)
 (c) Primitive unit-cell showing the angle θ as a projection of the beam on to the zx plane

4.5.3 Results

4.5.3.1 Analytical Methodology

Due to the increased complexity of the space group analysed, the linear compressibility for an orthorhombic type III beam structure has been derived using a method that differs from those used to derive the formulae for tetragonal and rectangular symmetries. The elastic compliances have instead been determined using the same principle of applying forces to a unit-cell containing an oriented Euler beam although instead of applying a hydrostatic force, axial forces are applied upon each axis separately and the elastic compliances are determined. The linear compressibility is then calculated using

$$\beta_L = (S_{11} + S_{12} + S_{13})L_x^2 + (S_{22} + S_{21} + S_{23})L_y^2 + (S_{33} + S_{13} + S_{23})L_z^2 \quad (4.13) \quad (\text{Nye, 1964})$$

A full explanation of how the elastic compliances are derived is presented in Appendix

C.

4.5.3.2 Absolute Linear Compressibility

Figure 4.13(a) shows the minimum absolute linear compressibility of a type III beam structure within an orthorhombic symmetry as a function of the angles θ and α illustrated in Figure 4.12. The projected angle of the beam onto the zy plane is also a variable but is related to θ and α by $\tan^{-1}\left(\frac{\tan \theta}{\tan \alpha}\right)$. Maximum NLC is observed when two of the angles are 61.1° and the third is 45° therefore demonstrating that the limiting values of NLC are produced within a tetragonal symmetry. To aid visualisation of this, Figure 4.13 (b) shows the absolute NLC of a tetragonal system where $\alpha = 45^\circ$.

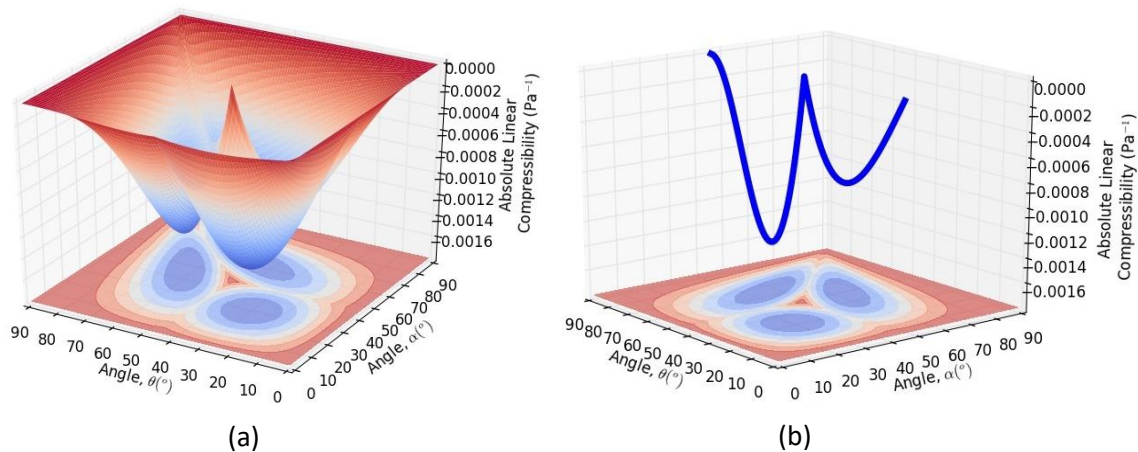


Figure 4.13 Minimum absolute linear compressibility of a type III beam structure in orthorhombic symmetry. (a) Surface plot of minimum absolute linear compressibility as a function of θ and α . (b) Line plot of minimum absolute linear compressibility for a type III beam structure in a tetragonal symmetry where θ is varied and $\alpha = 45^\circ$. Note: both plots include a contour plot to aid visualisation where magnitudes are denoted by shades of blue (low) to red (high).

4.5.3.3 Normalised Linear Compressibility

Figure 4.14(a) displays the minimum normalised values of NLC of a type III beam structure within an orthorhombic symmetry as a function of the angles θ and α that are illustrated in Figure 4.12. The range of values is enveloped by those gained from the tetragonal analysis, the values of which are shown in Figure 4.14(b) where $\alpha = 45^\circ$. Additionally, when

θ and α are both equal to 45° the symmetry becomes cubic and the normalised linear compressibility is $1/3$ due to the isotropic values of absolute linear compressibility.

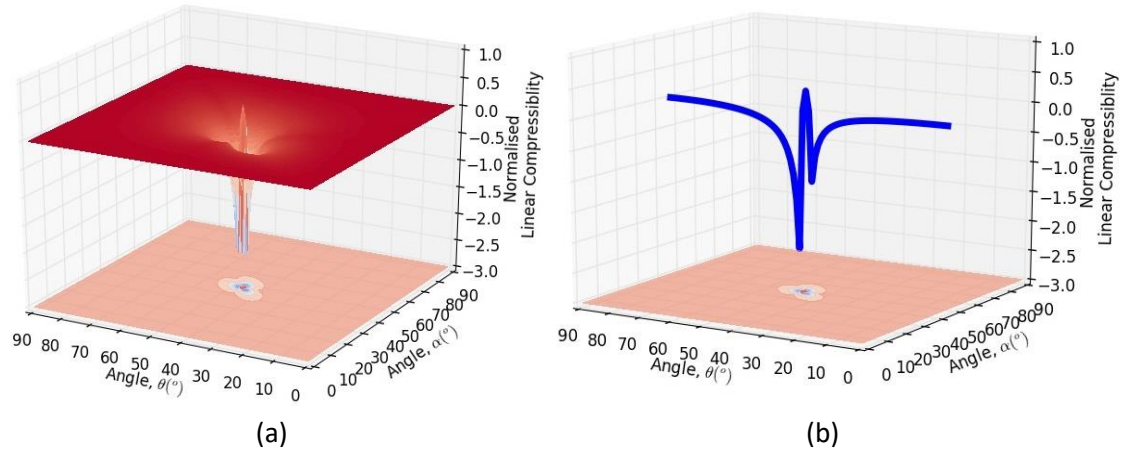


Figure 4.14 Minimum normalised linear compressibility of a type III beam structure in an orthorhombic symmetry. (a) Surface plot of minimum normalised linear compressibility as a function of θ and α . (b) Line plot of minimum normalised linear compressibility for a type III beam structure in a tetragonal symmetry where θ is varied and $\alpha = 45^\circ$. Note: both plots include a contour plot to aid visualisation where magnitudes are denoted by shades of blue (low) to red (high).

4.6 Conclusions

The Chapter has shown similar results to those reported in Chapter 3 with some subtle differences being encountered due to the models being three-dimensional. The modelling of the tetragonal system has shown that NAC could be created when the unit-cell aspect ratio is less than 1. In addition to this, modelling beams within an orthorhombic symmetry has shown that it is possible for the direction and magnitude of the NLC to be tuneable across three orthogonal directions. Additionally, altering the ratio between the constituent beam length and radius can modify the absolute NLC (as reported for two-dimensional structures in Section 3.5.1.2) of all of the structures reported in this chapter, although no in depth analysis was deemed necessary.

Chapter 5

“Spaced” Two- and Three-Dimensional Structures

5.1 Introduction

The effect of including spacers on the previously analysed two-dimensional rectangular and three-dimensional tetragonal structures is investigated as a means of both increasing and fine tuning the attainable values of absolute NLC. Firstly, the reason for including such a modification is explained, and then the resulting effects this modification has on both two- and three-dimensional beam structures is reported.

5.2 Addition of “Spacers”

5.2.1 Preamble

If it is possible to increase the magnitude of the bending force subjected to the beam, and hence increase the bending deflection with respect to the axial compressive displacement, the absolute NLC can be increased in a specific direction. By spacing apart the angled beams and increasing the length of the unit-cell, the ratio between forces acting on different global axes can be changed without changing the beam angle. This section adds this modification to structures previously analysed by adding “spacers” to both two-dimensional rectangular and three-dimensional tetragonal arrangements.

5.2.2 Two-Dimensional Rectangular

5.2.2.1 Spacer Geometry

Figure 5.1 shows the geometry for a two-dimensional beam arrangement, the variables, γ_A and γ_B are introduced and are the spacer length in the x and y directions. The “spacer” is assumed to be rigid for the purposes of these calculations. All other properties and variables assigned to the oriented beam remain the same as those applied in Chapter 2.

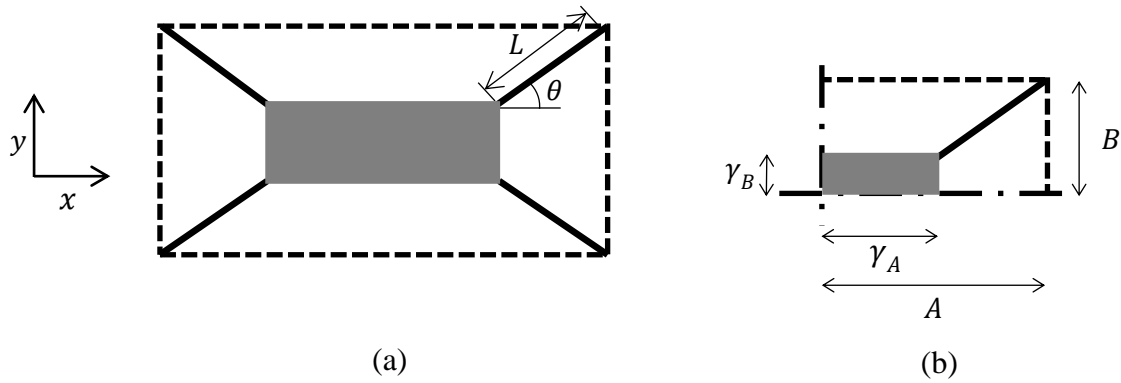


Figure 5.1 Repeating (a) and primitive (b) unit-cells for the two-dimensional rectangular model with inclusion of spacer

5.2.2.2 Results

The derivation of the formulae that predict the linear compressibility of this structure is included in Appendix A. The formulae for the absolute linear compressibility of a spaced rectangular array are

$$\beta_x = -\frac{L^3 \cos(\theta)\sin(\theta)}{3EI} + \frac{[(\sin(\theta)L + \gamma_B)\sin^2(\theta)]L^3}{3EI(\cos(\theta)L + \gamma_A)} + \frac{L \sin(\theta)\cos(\theta)}{E\phi} + \frac{[(\sin(\theta)L + \gamma_B)\cos^2(\theta)]L}{E\phi(\cos(\theta)L + \gamma_A)} \quad 5.1$$

and

$$\beta_y = -\frac{L^3 \sin(\theta)\cos(\theta)}{3EI} + \frac{[(\cos(\theta)L + \gamma_A)\cos^2(\theta)]L^3}{3EI(\sin(\theta)L + \gamma_B)} + \frac{L \sin(\theta)\cos(\theta)}{E\phi} + \frac{[(\cos(\theta)L + \gamma_A)\sin^2(\theta)]L}{E\phi(\sin(\theta)L + \gamma_B)} \quad 5.2$$

These formulae, compared with Equations 3.4 and 3.5, cannot be simplified in the same way, and appear much more complicated. The equations are derived in the same way as those presented in Chapter 3 and the full derivation is shown in Appendix A.

The resulting minimum absolute linear compressibilities are shown in Figure 5.2 for three different lengths of the spacer, γ_A . The minimum values of NLC are increased in magnitude and the angle of θ for which these minimum values occur also changes.

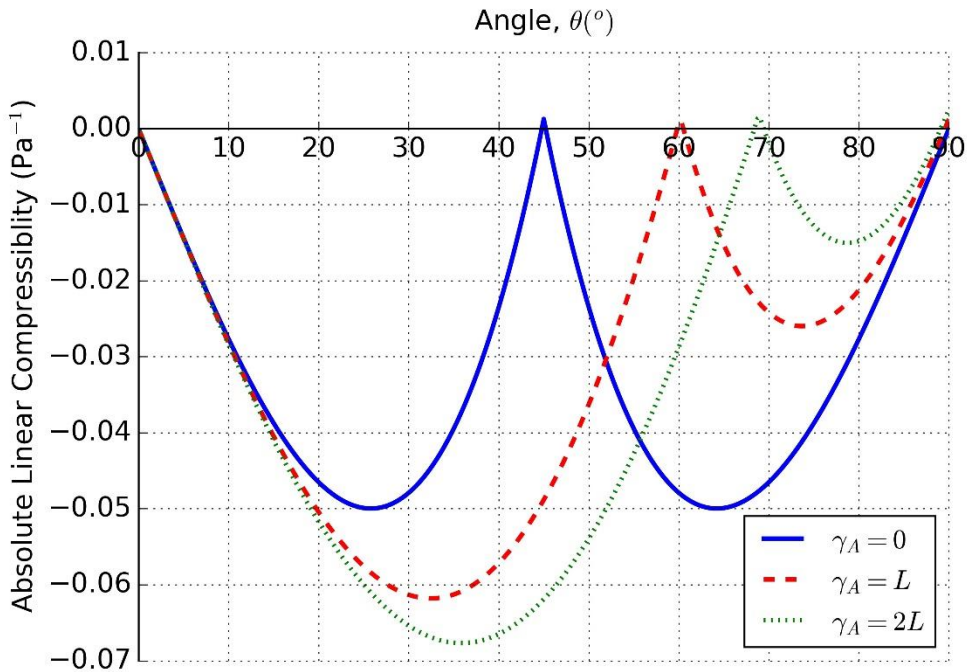


Figure 5.2 Minimum absolute linear compressibilities of a type II beam structure in a rectangular symmetry with spacers of differing lengths.

This change occurs because a new balance is found between the competing factors that contribute toward NLC. Figure 5.3 illustrates that when a spacer, aligned to the x -axis, is introduced, the unit-cell parameter, A , will increase. This causes the ratio of F_y/F_x to become larger, thus increasing the absolute linear compressibility. As γ_A increases, the angle of θ that creates the maximum absolute NLC increases toward a maximum of 45° but will not increase beyond this because at this angle the proportion of the bending deflection of the beam that contributes to lengthening of the unit-cell is at a maximum.

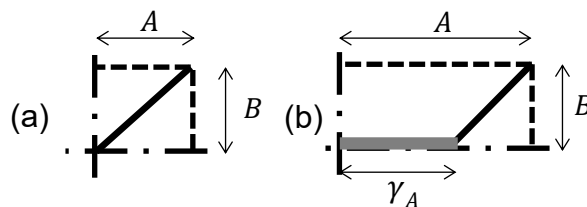


Figure 5.3 (a) Unit-cell parameters of spaced rectangular structure without spacer (b) Unit-cell parameters of spaced rectangular structure with spacer

This change in linear compressibility can also be explained mathematically. Figure 5.4 illustrates the effect that the introduction of the γ_A variable has on each term in Equation 5.1.

In this case, the terms that dominate the calculation of the linear compressibility in the x direction (shown in Figure 5.4(d)), are those relating to flexure of the beam; terms one and two. Of these two terms, term two is the only one that is appreciably affected as the presence of γ_A has lowered the value across the full range of θ and the linear compressibility is consequently reduced.

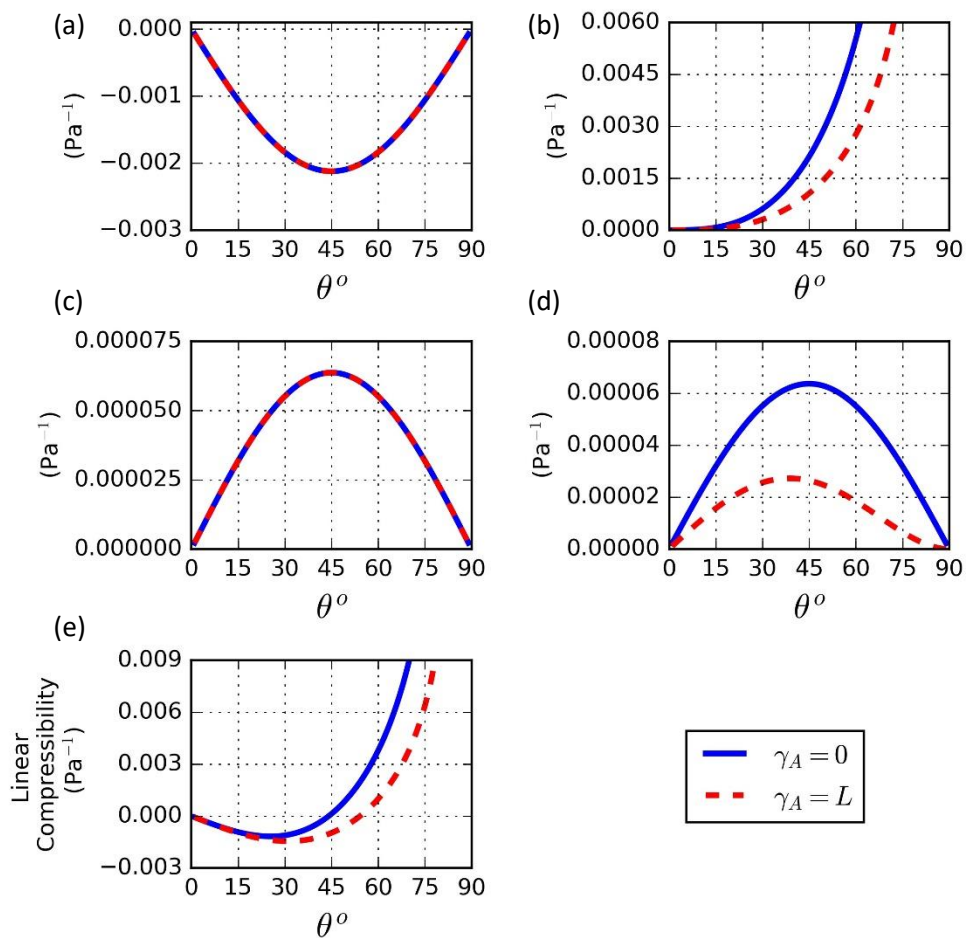


Figure 5.4 (a)-(d) Plots of terms 1-4, respectively, from Equations 5.1-5.2 for different values of γ_A (e) β_x plotted using Equation A1 for different values of γ_A

Although not formally presented, if γ_B were to be introduced, the unit-cell parameter, B , would increase, thus increasing the F_x/F_y ratio. This would have a similar effect to that already discussed but the axes would be reversed.

The resulting minimum normalised linear compressibilities are shown in Figure 5.5 for three different lengths of the spacer, γ_A . The normalised NLC follows a similar relationship with θ to that documented in preceding chapters. The normalised values become 0.5 when the compressibilities in the x and y directions are equal. The angle of θ which creates this angle is, however, increased when a spacer is included. This is due to a spacer increasing the absolute values in the x direction and decreasing them in the y direction such that they become equal at a different angle of θ .

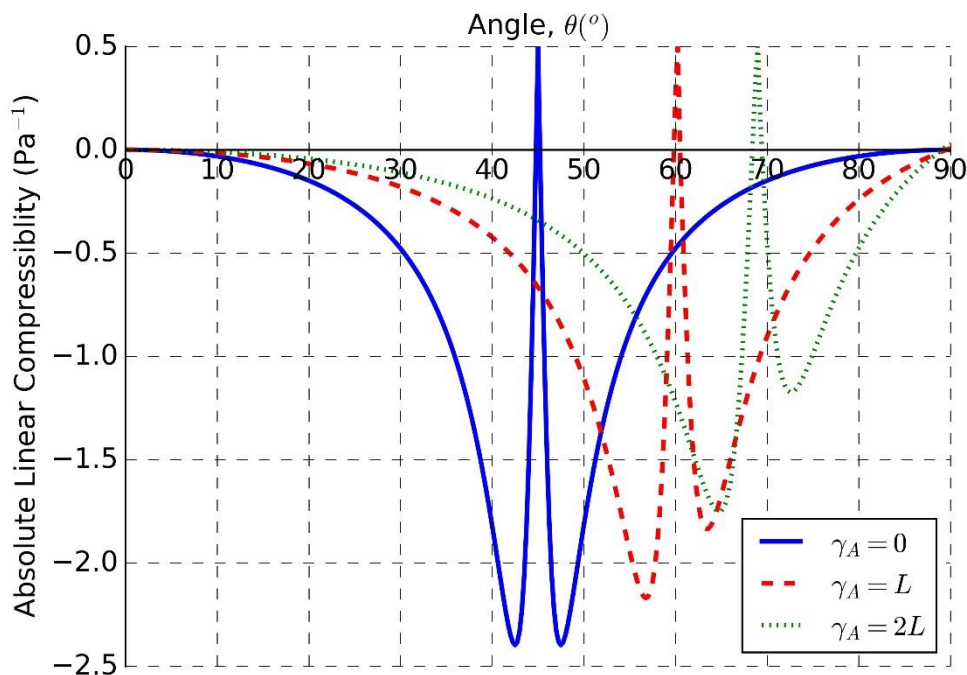


Figure 5.5 Minimum normalised linear compressibilities of a type II beam structure in a rectangular symmetry with spacers of differing lengths.

5.2.3 Three-Dimensional Tetragonal

5.2.3.1 Spacer Geometry

Figure 5.6 shows the addition of a spacer to the type III beam structure within a tetragonal symmetry. Two new variables have been introduced γ_A and γ_C which are the length of the spacers in the x and z directions respectively.

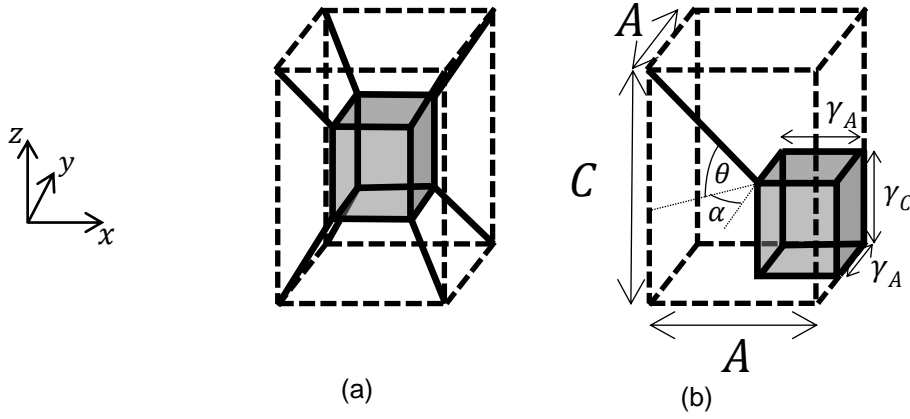


Figure 5.6 (a) Repeating unit-cell of type III beam structure with spacer in a tetragonal symmetry (b) Primitive unit-cell of type III beam structure with spacer in a tetragonal symmetry

5.2.3.2 Results

The resulting formulae for absolute linear compressibility within this system are

$$\beta_x = -\frac{L^2 \left[\sin(\mu) \cos^2(\mu) + \frac{1}{2} \cos^2(\mu) \sin(\mu) \right]}{E\phi} - \frac{L[\gamma_A \sin(\mu) \cos(\mu) \sin(\alpha) + \gamma_C \cos^2(\mu)]}{E\phi} - \frac{L^3 \left[\frac{L}{2} \cos^2(\mu) \sin(\mu) + \gamma_A \cos(\mu) \sin(\mu) \sin(\alpha) \right]}{12EI} + \frac{L^3 [L \sin^3(\mu) + \gamma_C \sin^2(\mu)]}{12EI} \quad 5.3$$

and

$$\beta_z = -\frac{L \sin(\mu) (L \cos(\mu) \sin(\alpha) + \gamma_A)^2}{E\phi (L \sin(\mu) + \gamma_C)} + \frac{[L^2 \cos(\mu) \sin^2(\alpha) \sin(2\mu)]}{E\phi} + \frac{L \gamma_A \cos(\alpha) \sin(2\mu)}{E\phi} - \frac{L^3 \cos(\mu) (L \cos(\mu) \sin(\alpha) + \gamma_A)^2}{12EI (L \sin(\mu) + \gamma_C)} + \frac{L^4 \sin(2\mu) + 4L^3 \gamma_A \cos(\alpha) \sin(\mu)}{24EI} \quad 5.4$$

The derivation of these formulae is included in Appendix B. The minimum absolute and normalised values of linear compressibility are displayed in Figure 5.7 and Figure 5.8 respectively for different values of γ_C . The inclusion of spacers has a similar effect on the linear compressibility as observed for the two-dimensional system, although in this case the maximum NLC is increased and the maximum NAC is reduced. The angle of θ at which these

maxima occur is also altered. Similarly to the two-dimensional model, the angle of θ for which the maximum NLC occurs will tend toward 45° as γ_C is increased further. Similarly the point at which the normalised linear compressibility becomes $1/3$ is illustrated in Figure 5.8.

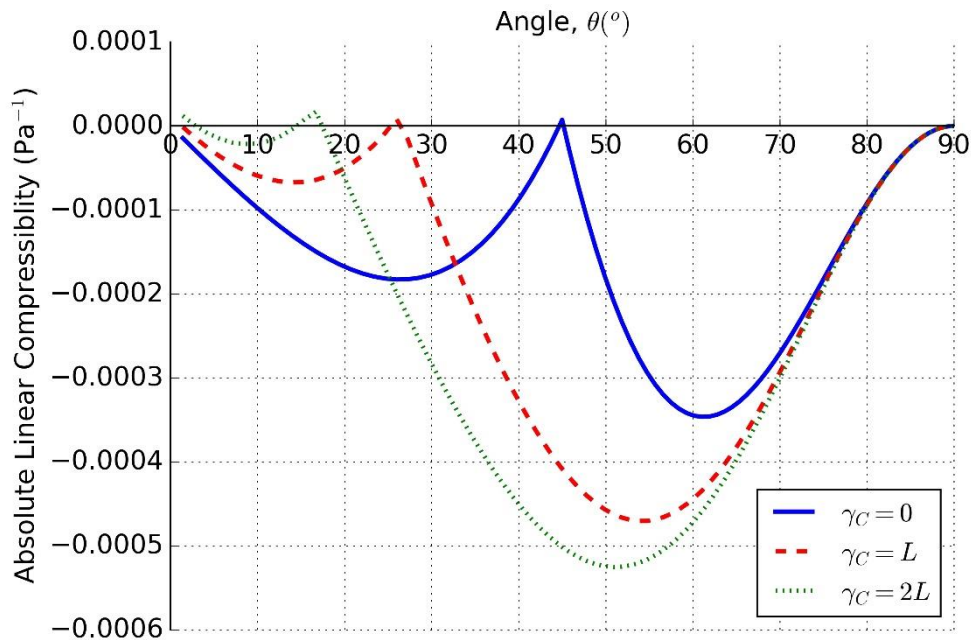


Figure 5.7 Minimum absolute linear compressibility of a type III beam structure in a tetragonal symmetry for three different values of γ_C .

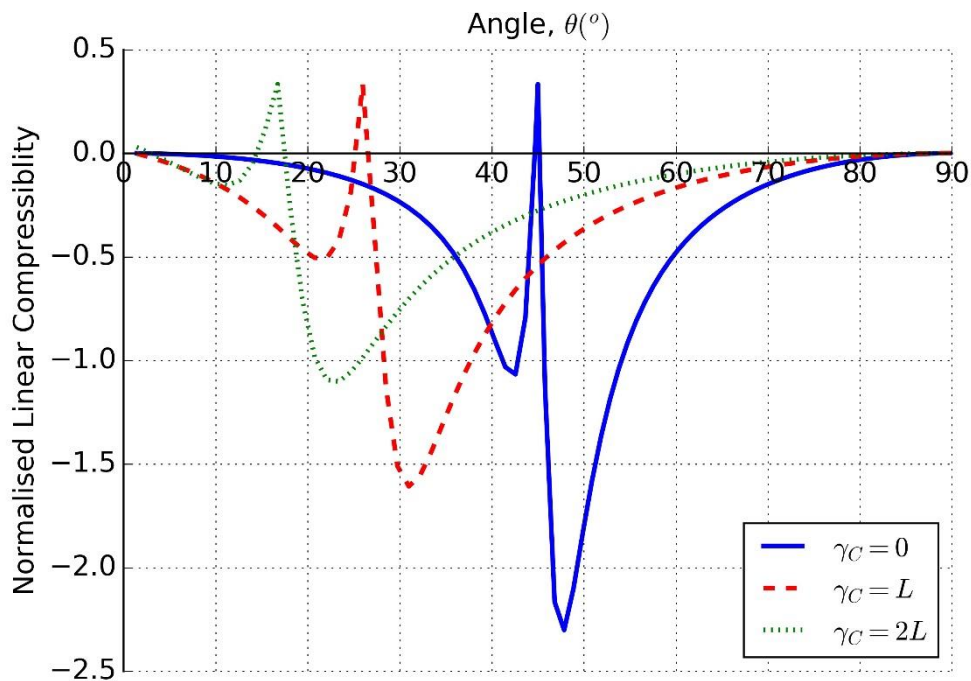


Figure 5.8 Minimum normalised linear compressibility of a type III beam structure in a tetragonal symmetry for three different values of γ_C .

To aid visualisation, Figure 5.8 shows the minimum absolute linear compressibility plotted against the aspect ratio of the unit cell for the three different values of γ_C plotted in Figure 5.7. It should be noted that when a spacer aligned to the z-axis is present the minimum aspect ratio of the unit-cell is $\frac{\gamma_C}{L \sin(45^\circ)}$.

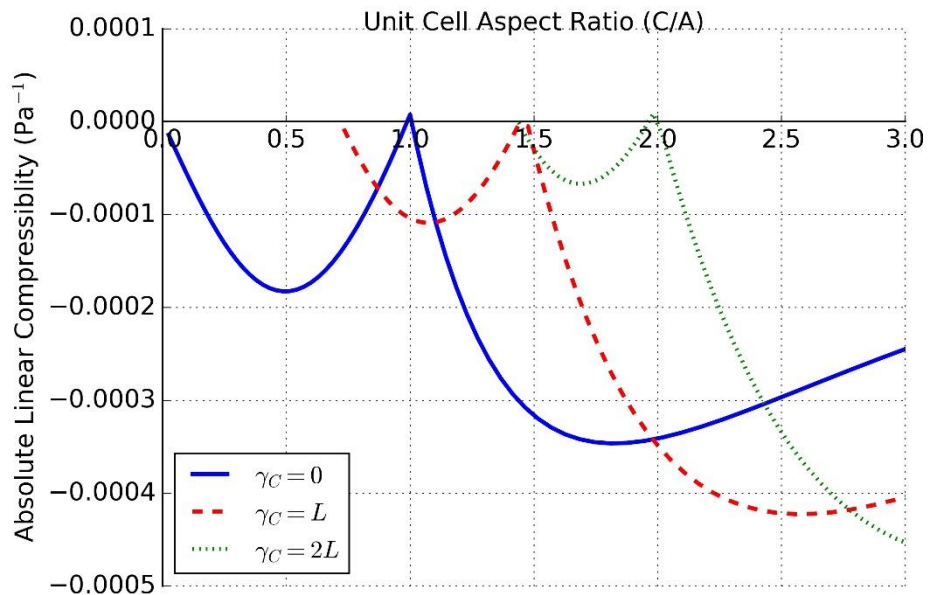


Figure 5.9 Minimum normalised linear compressibility of a type III beam structure in a tetragonal symmetry plotted against the aspect ratio of the unit-cell for three different values of γ_C

Figure 5.9 and Figure 5.11 plot the minimum absolute and normalised linear compressibilities for different values of γ_A . Increasing γ_A has the effect of increasing the range of values of θ for which NAC is present and also increases the maximum NAC. Interestingly the maximum NLC is also increased. This is because the introduction of γ_A increases the pressure acting to lengthen the unit-cell at larger angles of θ .

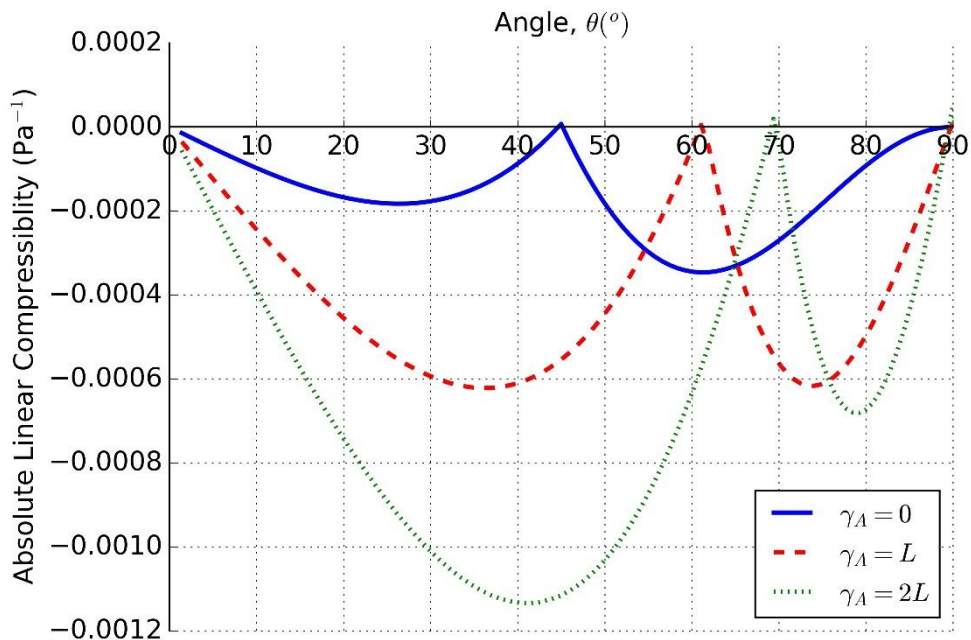


Figure 5.10 Minimum absolute linear compressibility of a type III beam structure in a tetragonal symmetry for three different values of γ_A .

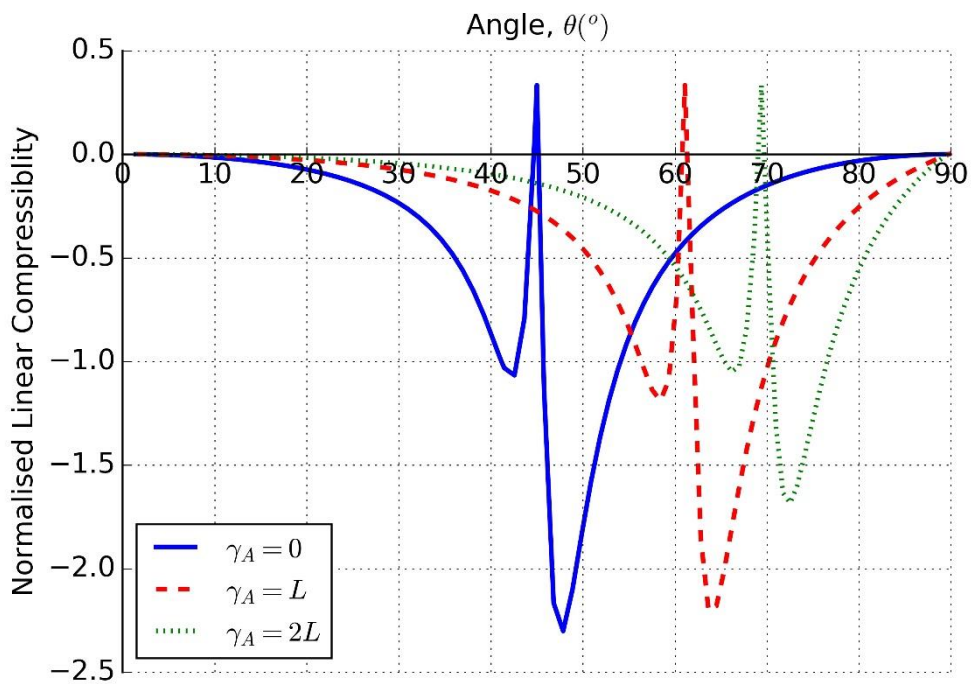


Figure 5.11 Minimum normalised linear compressibility of a type III beam structure in a tetragonal symmetry for three different values of γ_A .

Again, normalised values of NLC peak at angles close to the changeover from NAC acting in the xy plane to NLC acting on the z -axis.

5.3 Conclusions

This chapter has shown that it is possible to increase the magnitude of NLC observed in the framework structures analysed in Chapters 3-4 by introducing a “spacer”. This spacer has the effect of increasing the proportion of the pressure loading acting on/along a particular axis/plane.

The addition of the rigid “spacer” to these structures allows the structure to be comparable with that of MOFs. The rigid spacer beam can be likened to the rigid metallic clusters present within MOFs and the more flexible inorganic linkers that join these clusters can be likened to the flexible angled beam within the structures analysed. Therefore it is possible to see that the simple effect caused by adding a spacer to the structure has already been exploited unknowingly.

It should be stressed that the structures presented in Chapter 3-5 are highly idealised and are not intended to mimic the behaviour of real materials perfectly, as much more complex interactions are often present. The chapters do however present a very robust understanding of the “wine-rack” mechanism and can assist with the discovery of more NLC materials.

In summary, analysis of the investigations reported throughout Chapters 3-5 has shown that NLC is manifested by the tendency of a rigid strand to rotate or bend causing the structure to lengthen in one direction and shorten in the perpendicular direction(s), a two-dimensional illustration of this is shown in Figure 3.17.

Chapter 6

Large Strain Effects in 2D Structures

6.1 Introduction

Chapters 3-5 presented the linear compressibility of beam structures where elastic properties relating to small strains were considered. To fully appreciate the NLC effect of a specific material, a number of different properties must be considered in parallel; the absolute compressibility, the normalised compressibility and the compressibility capacity. The first two properties have already been reported for a number of frameworks in Chapters 3-5 and this chapter focuses on determining the compressibility capacity of some of these frameworks. Compressibility capacity is the maximum strain that the material can undergo along the axis of NLC when subjected to hydrostatic loading (Cairns and Goodwin, 2015). To determine this value it is necessary to predict how these structures behave when large strains are encountered due to large hydrostatic loads.

To understand the behaviour of these structures at high strains, six different two-dimensional beam configurations are considered, all based on the “wine-rack”. Three of these are a cross configuration and three are a spaced-cross with a spacer of length $0.5L$. In each case the initial angle, θ_0 has been modified.

Two approaches are used here to determine how these structures behave when large strains are applied. Firstly, the joints are replaced by hinges in a quasi-elastic analysis of these structures. This produces idealised values of compressibility capacity that can be achieved by these frameworks. Secondly, the flexing nature of the joints is retained, and the behaviour of the structures is modelled with FEA. The compressibility capacities, when calculated using the simplistic hinging analysis method, are slightly larger than those calculated when using the FE methodology that accounts for beam flexure.

6.2 2D Hinging Model

6.2.1 Modelling

The simplest way of considering high strains is to assume a two-dimensional structure where the beams hinge about each other (see Figure 6.1). Analytical methods are used to model this behaviour and the models used are based on those derived in Chapter 3, where the linear elastic response of angled beams to hydrostatic loading is considered. In the case presented here, the beam is permitted to rotate rather than bend, and a rotational stiffness of $\frac{L^2}{12EI}$ (where these constants take the values defined in Section 3.4) has been applied to the beam which represents the ratio of applied force(N):angular rotation(rad). This value is chosen to make the results comparable with those presented in Chapter 2 and those discussed in the latter part of this chapter.

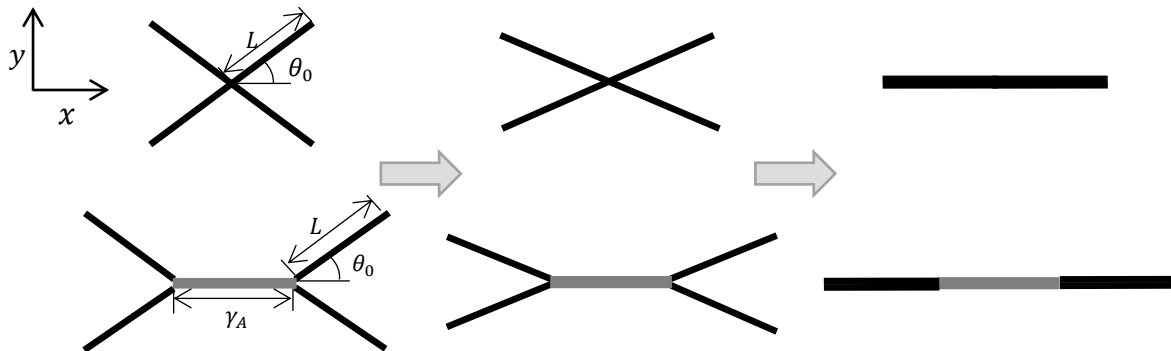


Figure 6.1 Hinging deformation of cross and spaced-cross structures

The expressions for the linear compressibility of the hinging model are derived in a very similar fashion to those presented in Chapter 3 (and later modified in Chapter 5). The main difference is that loads acting on the axis of the beam are disregarded and the beam is considered to rotate rigidly. The equations for the hinging model of the cross configuration are therefore

$$\beta_x = \frac{L^3 \cos(\theta)\sin(\theta)}{12EI} - \frac{\sin^3(\theta)L^4}{12EI(\cos(\theta)L + \gamma_A)} \quad 6.1$$

and

$$\beta_y = \frac{L^3 \sin(\theta) \cos(\theta)}{12EI} - \frac{(\cos(\theta) L + \gamma_A) \cos^2(\theta) L^2}{12EI \sin(\theta)} \quad 6.2$$

The initial angle is not necessary to calculate the linear compressibility of the structure but is used to calculate strain, ε_x , at a given angle θ

$$\varepsilon_x = L \left(\frac{\cos(\theta) - \cos(\theta_0)}{\cos(\theta_0) + \gamma_A} \right) \quad 6.3$$

The compressibility capacity is calculated using this expression when $\theta = 0$. When modelled, the initial angle, θ_0 , is set to 44° in the cross model and 53° in the spaced-cross model. These angles are the maximum (accurate to 1°) at which a resultant force will rotate the beam such that the unit-cell lengthens in the x direction.

6.2.2 Results

The linear compressibilities of the hinging system for increasing strains are shown in Figure 6.2, where ε_x is used as the dependant variable instead of θ . The figure shows that the compressibility capacity of such a system is approximately 0.414 and the compressibility capacity of a spaced-cross structure is roughly 0.370 when $\gamma_A = 0.5L$. The resultant strain of the structure reduces because the introduced spacer does not undergo any strain itself. The maximum and minimum values of compressibility do however increase in magnitude as discussed in Chapter 5, meaning that adding a spacer to the structure affects all three of the constants that measure the NLC effect. Also, these results only differ in detail to those presented in Chapter 3. This is because axial deformation (which is accounted for in Chapter 3) of these beams has only a small effect on the values of compressibility. The solution from these two models will however diverge if the length/radius ratio of the constituent beams is very small, because the axial component of the deformation becomes larger.

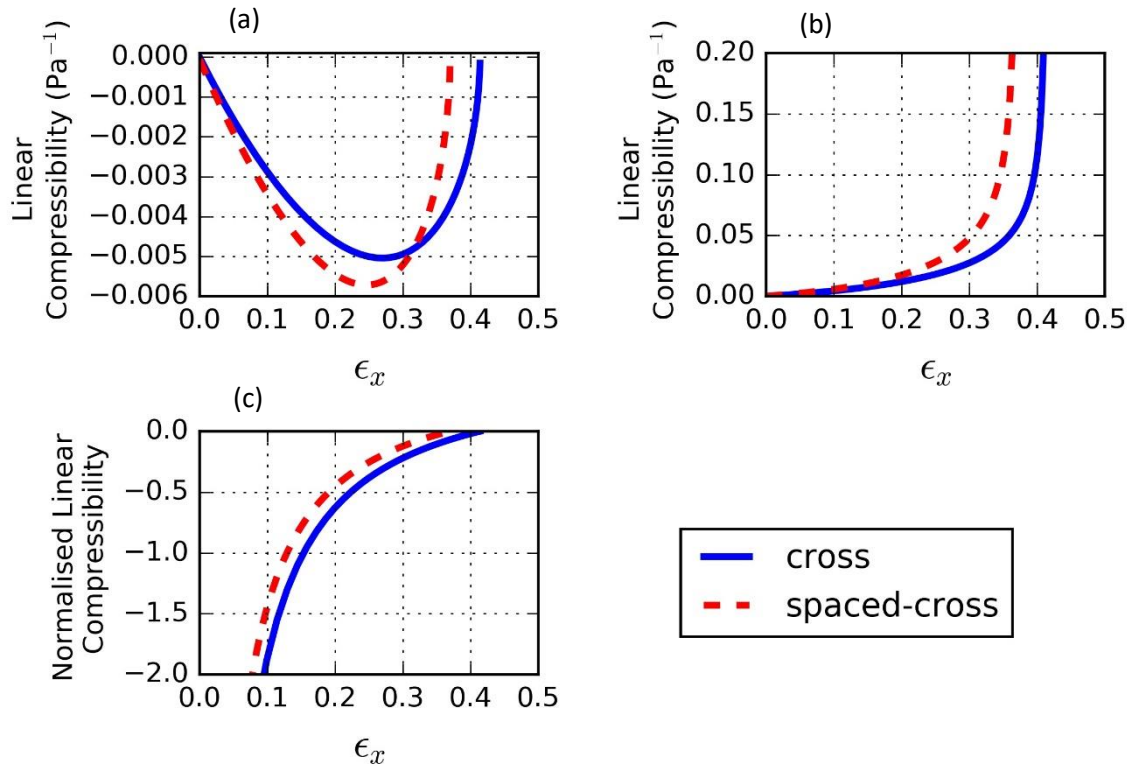


Figure 6.2 (a) Minimum linear compressibility of the hinging cross and spaced-cross structures plotted against strain on the x-axis arising from hydrostatic pressure (b) Maximum linear compressibility of the hinging cross and spaced-cross structures plotted against strain on the x-axis arising from hydrostatic pressure (c) Minimum normalised linear compressibility of the hinging cross and spaced-cross structures plotted against strain on the x-axis arising from hydrostatic pressure

6.3 2D Beam Flexure Model

6.3.1 Preamble

Modelling the structure using beam mechanics instead of hinging provides a more realistic representation of how these structures might deform when large strains are applied. Due to the changing geometry of the constituent beams at large strains, it is difficult to use analytical methods to calculate the compressibility of these structures and FE modelling is used instead.

Six different variations of the two-dimensional beam structure are modelled where the initial value of the internal angle, θ_0 , has been varied to equal 10° , 25° and 40° for the cross-model and 20° , 35° and 50° for the spaced-cross model. These models are then submitted to

hydrostatic loading until the beams can no longer deform via flexure. Single repeatable unit-cells are shown in their initial, partially and fully deformed states in

Figure 6.3. As the beam ends are not permitted to rotate as the structure is loaded, they will remain positioned at their initial angle. This means the beams cannot become completely aligned with the x-axis as predicted by the hinging model, and the compressibility capacity is likely to be lower in these models. When the structure intersects itself, as shown in

Figure 6.3, no further pressure will be applied, as the model is assumed to have reached its full strain range.

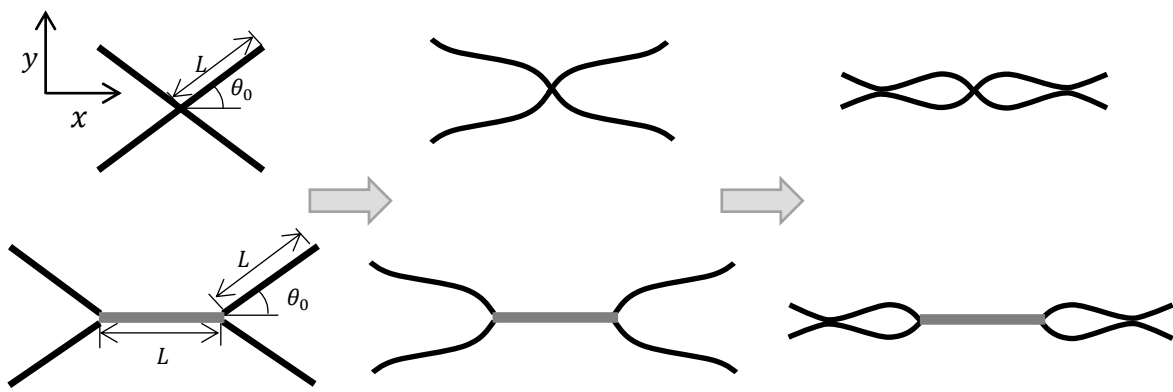


Figure 6.3 Flexing deformation of cross and spaced-cross structures

6.3.2 Modelling

The boundary conditions, input parameters, mesh and element type used are the same as those described in Section 3.6 and similarly an 11×11 array of the repeatable unit-cell is used. However as large scale deformations are being simulated, the models are run with the non-linear geometry feature activated. A separate mesh convergence study has not been conducted for this study although the application of 20 elements per beam (the same as that applied to the structures analysed in Chapter 3) is deemed to be more than sufficient. Applying loads to the model that are proportional to the side length (and representative of a hydrostatic pressure) is not straightforward as the side lengths will change unpredictably as the structure deforms. To ensure that a hydrostatic stress is represented as accurately as possible, the increments of strain and hence the rate at which the forces are recalculated must be high enough to produce only a small error. To reduce this error, a python script was written to import

the deformed geometry into a new input file and then calculate and apply suitable loads as a function of the model dimensions. This cycle is repeated until the model can no longer deform via beam flexure. These loops are performed in 0.001 increments of strain along the x -axis. Stresses in the constituent beams have not been considered and no consideration of yielding or rupture has been included.

6.3.3 Results

The resulting strain-dependent linear compressibility for structures with different initial internal angles is shown in Figure 6.4. An example of a deformed unit-cell at various levels of strain along the x -axis is shown in

Figure 6.5 where $\theta_0 = 40^\circ$. All models exhibited NLC throughout the strain range analysed. In each case the hydrostatic stress was increased until the structure became self-intersecting.

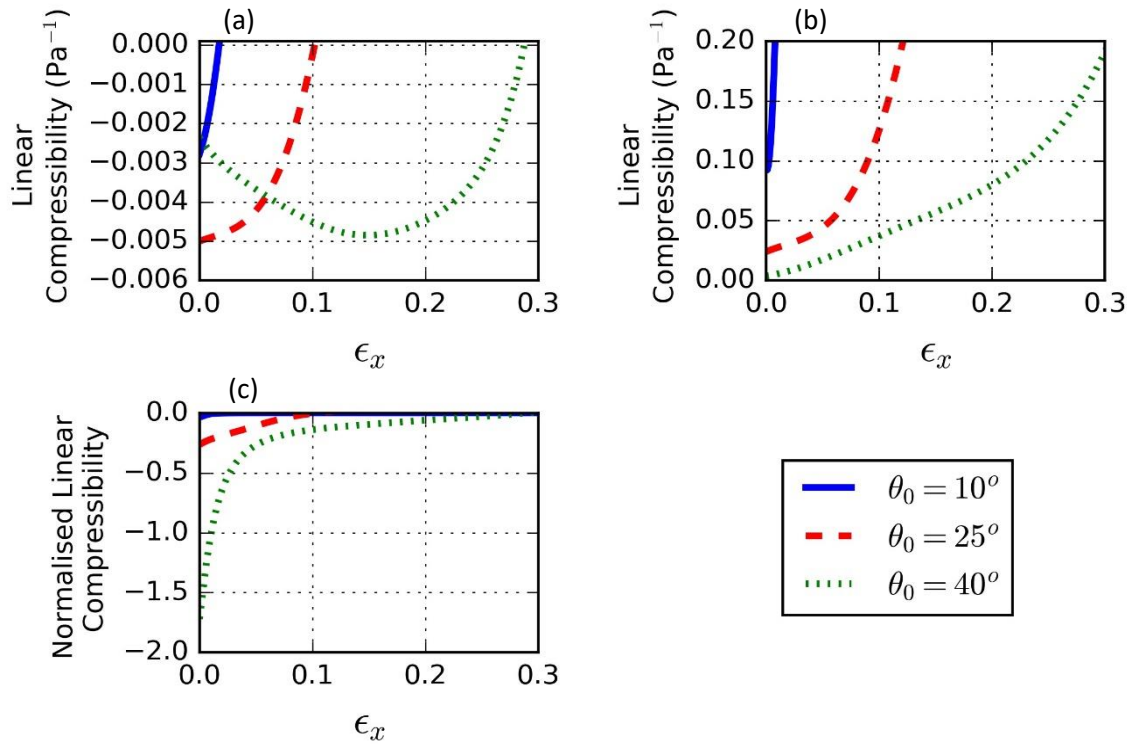


Figure 6.4 (a) Minimum linear compressibility of the cross structure using FE beam modelling where different plots are shown for different values of θ_0 (b) Maximum linear compressibility of the cross structure using FE beam modelling where different plots are shown for different values of θ_0 (c) Minimum normalized linear compressibility of the cross structure using FE beam modelling where different plots are shown for different values of θ_0

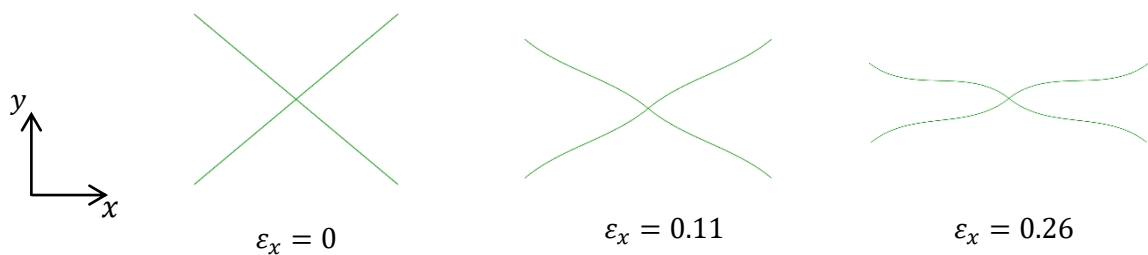


Figure 6.5 Initial and deformed cross geometry of a single repeatable unit-cell where $\theta_0 = 40^\circ$

When $\theta_0 = 40^\circ$, peak NLC is exhibited at $\varepsilon_x = 0.149$. This is because the deformed geometry is approaching that of the case analysed in Chapter 3 where $\theta = 26^\circ$ and the NLC is a maximum for linear geometry cases. The equivalent internal angle for which NLC is a

maximum is approximately 32° (calculated from consideration of its aspect ratio) when $\theta_0 = 40^\circ$. Figure 6.6 illustrates this graphically.

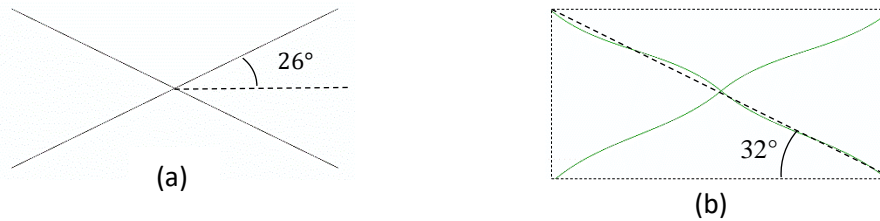


Figure 6.6 (a) Hinging cross where β_x is a minimum ($\theta = 26^\circ$) (b) Beam flexure model where β_x is a minimum (equivalent internal angle is 32° based on unit-cell aspect ratio) and the initial internal angle is 40°

For the other two cases where $\theta_0 < 26^\circ$, the maximum NLC is exhibited by the model in its initial state. The increase in the angle at which maximum NLC is observed can be attributed to non-linear geometry effects. As the angled beam deforms, the bend in the beam increases, which causes the strain in the x direction to be less than if it were straight as the beam is bending in on itself. This effect becomes more pronounced as more deformation is applied. This in turn causes the maximum NLC to be observed at a greater angle than that predicted by the hinging model.

The normalised compressibility in all cases is at a maximum when the strain is zero. This is because this is the point at which the geometries are closest to being isotropic and hence have very large values of normalised compressibility as reported in Chapters 3-5.

The analyses were stopped when no further strain could be applied to the model. Practically this was found to be when the displaced geometry of the model became self-intersecting. Figure 6.7 shows the resulting geometry from the final load increment, where $\theta_0 = 40^\circ$, before the geometry became self-intersecting.



Figure 6.7 Final displaced geometry of cross configuration where $\theta_0 = 40^\circ$

Figure 6.8 displays plots of the minimum, maximum and normalised compressibilities as a function of strain along the x -axis for the spaced-cross framework. An example of a deformed unit-cell at various levels of strain along the x -axis is shown in Figure 6.9 where $\theta_0 = 50^\circ$. For the equivalent spaced-cross analysed here, the maximum NLC occurs when $\theta = 29.8^\circ$ as predicted by the analytical model presented in Chapter 3 and the hinging model described in Section 6.2. For the cases analysed here, NLC is a maximum when the strain is 0.177 and 0.026 for the spaced-cross where $\theta_0 = 50^\circ$ and $\theta_0 = 35^\circ$ respectively. These values of strain are equivalent to an internal angle of $\theta = 32.3^\circ$ and $\theta = 31.4^\circ$ respectively. Maximum NLC occurs at an angle greater than that predicted by the hinging model due to the same effect observed for the cross configuration structure where $\theta_0 = 40^\circ$.

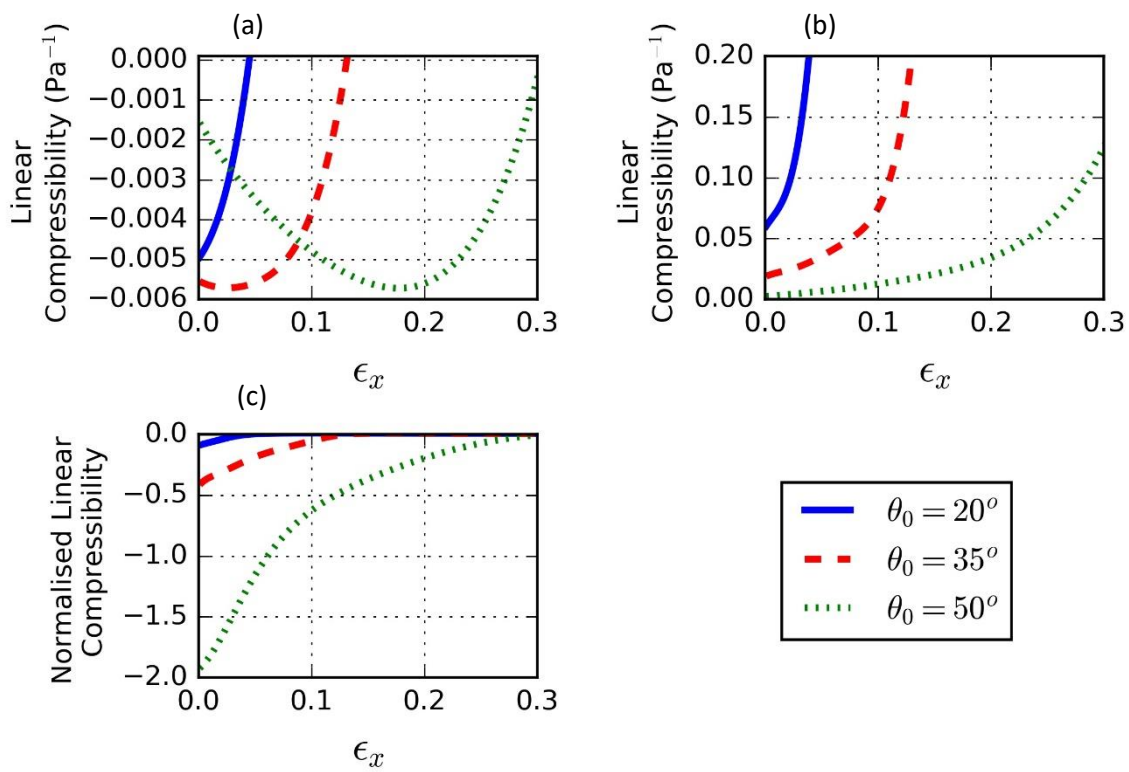


Figure 6.8 (a) Minimum linear compressibility of the spaced-cross structure using FE beam modelling where different plots are shown for different values of θ_0 (b) Maximum linear compressibility of the spaced-cross structure using FE beam modelling where different plots are shown for different values of θ_0 (c) Minimum normalised linear compressibility of the spaced-cross structure using FE beam modelling where different plots are shown for different values of θ_0

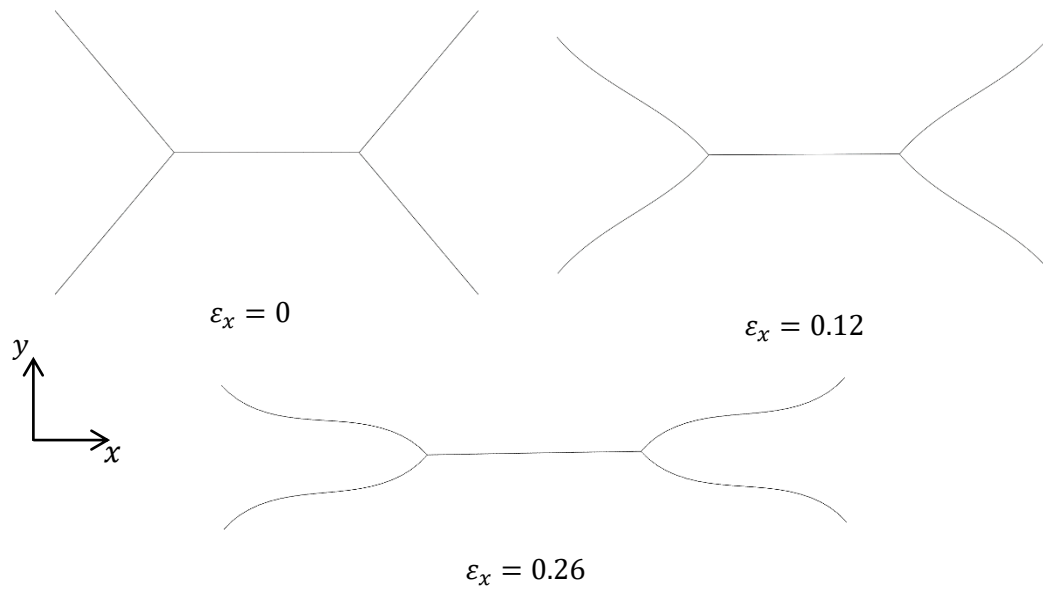


Figure 6.9 Initial and deformed spaced-cross geometry of a single repeatable unit-cell where $\theta_0 = 50^\circ$

6.4 Results Summary

A comparison between the results taken using the two methodologies is illustrated graphically in Figure 6.10 for the cross model where $\theta_0 = 40^\circ$ and in Figure 6.11 for the spaced-cross model where $\theta_0 = 50^\circ$. A close match can be observed in both cases for the minimum linear compressibility although there is a greater disparity in the calculation of the maximum linear compressibility which in turn causes some difference in the calculated minimum normalised linear compressibility. In both cases it is shown that the compressibility capacity (the maximum strain at which an NLC is present) is greater when using the analytical methodology as opposed to the results taken using non-linear FEA.

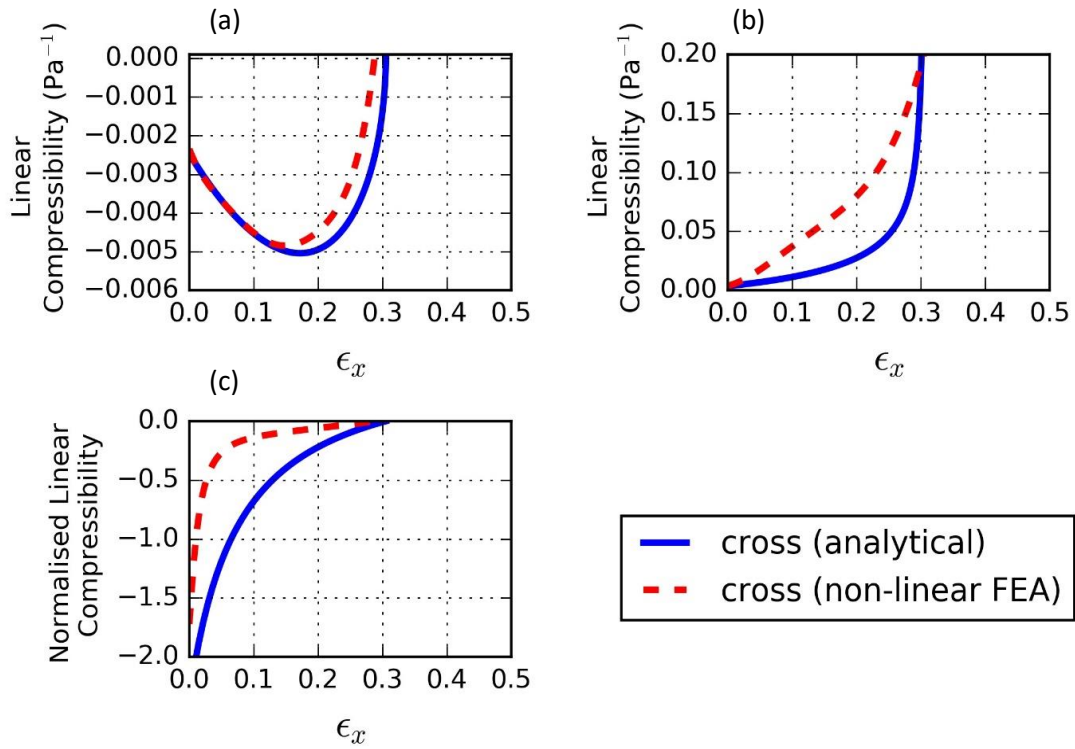


Figure 6.10 Comparison of results using the derived analytical formulae and FEA for the cross model where $\theta_0 = 40^\circ$. (a) minimum linear compressibility (b) maximum linear compressibility (c) minimum normalised linear compressibility

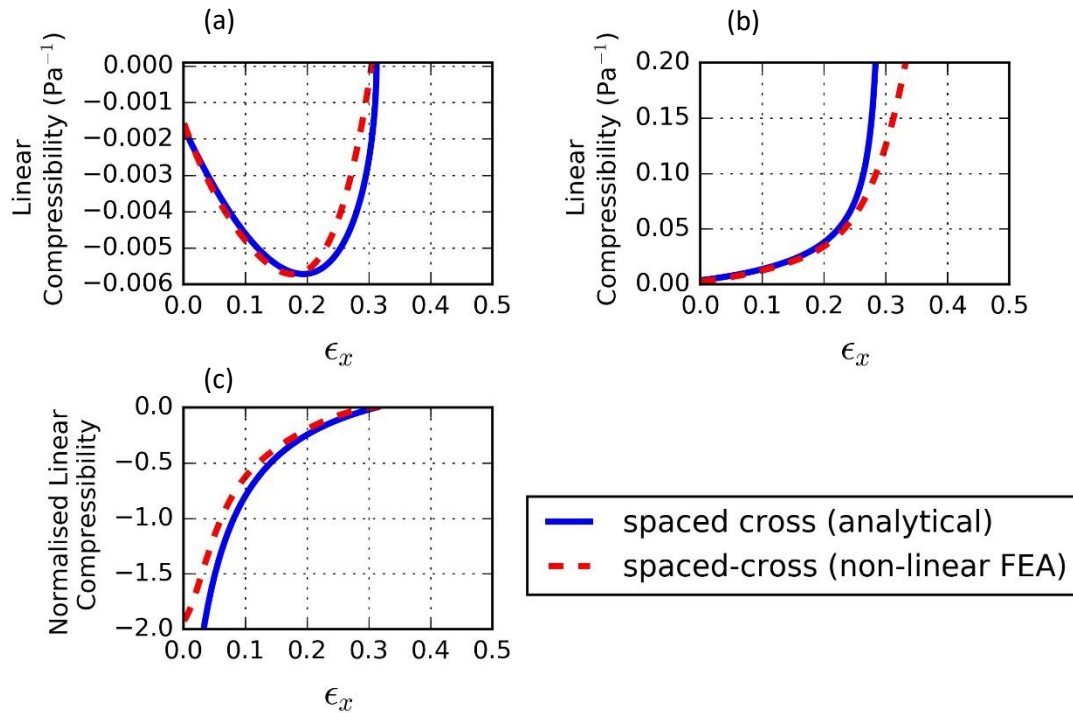


Figure 6.11 Comparison of results using the derived analytical formulae and FEA for the spaced-cross model where $\theta_0 = 50^\circ$. (a) minimum linear compressibility (b) maximum linear compressibility (c) minimum normalised linear compressibility

Table 6-1 lists the key information regarding both the hinging and beam flexure models for the different configurations assessed. The compressibility capacity calculated using the hinge model is a limiting value that can be achieved by a structure of a specific initial angle. The non-linear geometry effects that are accounted for in the FE beam model reduce these values as the beam is no longer straight. Additionally, the strain at which maximum NLC is observed and the magnitude of the maximum NLC is reduced due to the deformed geometry of the beam causing it to be less stiff on its own axis.

Initial Internal Angle θ_0	Cross Configuration			Spaced-Cross Configuration		
	10°	25°	40°	20°	35°	50°
Compressibility Capacity (Hinge Model)	0.015	0.103	0.305	0.042	0.137	0.313
Compressibility Capacity (FE Beam Model)	0.015	0.101	0.286	0.041	0.131	0.302
ε_x at maximum NLC (Hinge Model)	0	0	0.173	0	0.038	0.198
ε_x at maximum NLC (FE Beam Model)	0	0	0.149	0	0.026	0.177
Maximum NLC (Hinge Model)	-0.00268	-0.00503	-0.00504	-0.0049	-0.00572	-0.00572
Maximum NLC (FE Beam Model)	-0.00268	-0.00503	-0.00489	-0.0049	-0.00572	-0.00568

Table 6-1 Compressibility capacity of structures using hinge and beam modelling and the strain at which maximum NLC occurs for different values of θ_0

6.5 Conclusions and Further Work

The high strain behaviour of these structures has been analysed in order to calculate values of compressibility capacity. This represents a key part of understanding the NLC effect present in these structures. Having this understanding is important if research is to be directed toward creating applications. Although only two-dimensional structures have been analysed, it is logical to predict that a similar pattern would be observed if high strains within three-dimensional structures were to be investigated.

Further work could involve applying parent material properties to analyses. In particular it would be useful to gain a more realistic understanding of compressibility capacity by analysing the strain which would cause the material to turn plastic and no longer be functional. The point at which this occurs is likely to be dependent upon the value of θ_0 applied.

Chapter 7

Elliptical Voids

7.1 Introduction

Chapters 3-5 presented an analysis of a different cross structures that could be likened to a diamond shape and showed them to exhibit NLC. An analysis of ellipses is deemed a logical “next step” as this is very close to the shape of a diamond but does not have any corners that could create regions of high stress. Initial conceptual analysis shows that a two-dimensional hollow ellipse (composed of an isotropic and homogenous material) will have NLC, as visualised in Figure 7.1.

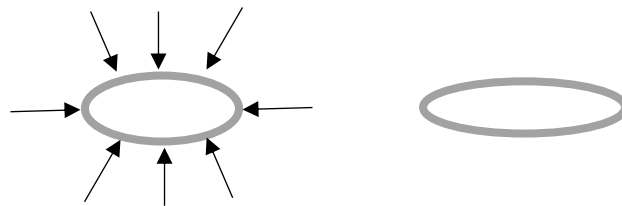


Figure 7.1 Lengthening of a hollow ellipse under hydrostatic pressure

This in itself does not lead to the creation of a continuum material with NLC although a material with an elliptical void will deform in a similar way and therefore a material with an array of elliptical voids that are small in comparison to the overall dimensions of the material could have NLC. Materials with specific arrangements of elliptical voids, different to those investigated in this chapter, have been shown to be auxetic due to elastic instabilities at high strains (Bertoldi et al., 2010).

Illustrating that such structures could have NLC would show that it is possible to manufacture an NLC material from any parent material. An FE analysis of such structures is reported in this chapter. The methodology used is initially described in Section 7.2, methods of arranging these voids are then presented, and are followed by an analysis of the structures in Section 7.3. Finally, conclusions are drawn in Section 7.4.

7.2 Methodology

7.2.1 Calculation of Linear Compressibility

As the modelling considered in this chapter is restricted to two dimensions, the compressibility can be calculated using a similar methodology to that applied in Chapter 3. The elastic compliance matrix for a two-dimensional rectangular symmetry is

$$\begin{bmatrix} S_{11} & S_{12} & - \\ S_{12} & S_{22} & - \\ - & - & S_{33} \end{bmatrix} \quad 7.1$$

The minimum and maximum values of NLC will always lie on the principal axes of the material and can be calculated using $\beta_x = S_{11} + S_{12}$ and $\beta_y = S_{22} + S_{12}$. Because the structures analysed in this chapter are too complicated for analytical calculations to give reliable results, the FE method is used to model how the geometries deform. Again as in Chapters 3-6, no analysis of the shear compliance is necessary. All models presented within this section represent a geometry where the through-thickness dimension is much larger than the dimensions of the unit-cell, hence all units quoted in this chapter are per unit thickness. The Young's modulus and Poisson's ratio assigned to the constituent material are 10MPa and 0.2 respectively and have been chosen arbitrarily.

7.2.2 FE Methodology

All FE models documented in this chapter use CPE8R (continuum element with plane strain condition with 8 nodes and reduced integration) elements. As the method used to derive the linear compressibility requires a number of compliances to be known, two different load cases are required. All models assume small displacement theory and only linear elastic material properties have been applied as it is only the response of the models to small strains that are of interest. Additionally, as the two-dimensional models are built to represent a large through-thickness section, plane strain conditions have been applied to all models.

A single repeatable unit-cell model has been used in all of the analyses presented in this chapter. The boundary conditions for the model being strained in the x direction are shown

in Figure 7.2(a). A strain of 0.02 is applied between the two vertical edges and the bottom horizontal edge is set such that no displacement in the y direction can occur across its length. All the nodes on the top horizontal edge are restricted so that their displacements in the y direction are equal. Boundary conditions for loading the model in the y direction utilise the same approach and are also shown in Figure 7.2(b).

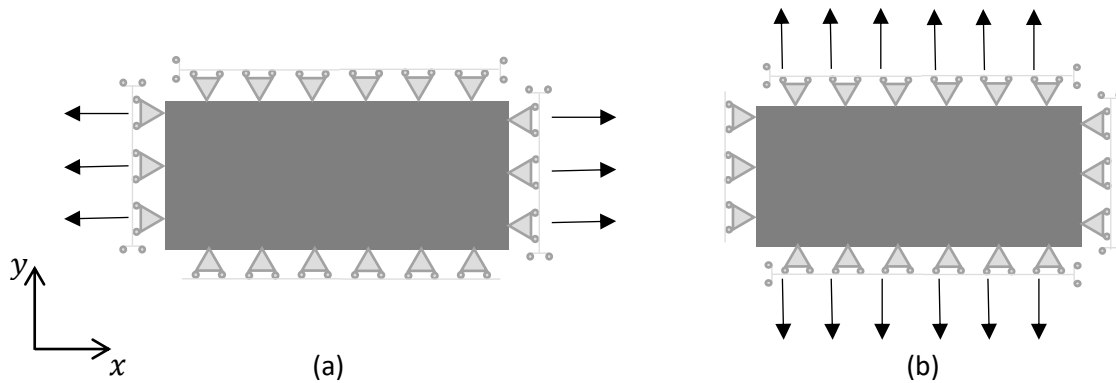


Figure 7.2 Boundary conditions applied to all models for (a) strain applied in the x direction, and (b) strain applied in the y direction.

This method of modelling has been used to reduce the number of elements required. This method has also been validated, in that good agreement has been observed with a 5×5 array model where boundary conditions were only applied to the loaded edges as illustrated in Figure 7.3 and displacements were taken by averaging the displacement across the central unit-cell.

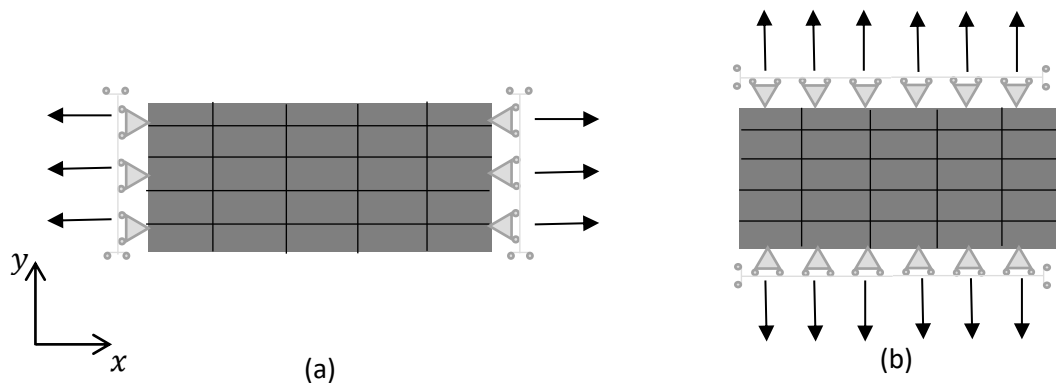


Figure 7.3 Boundary conditions applied to 5×5 unit-cell model for (a) strain applied in the x direction, and (b) strain applied in the y direction.

7.3 Analysis

7.3.1 Increasing Ellipse Aspect Ratio

7.3.1.1 Geometry

This initial study looks at how the linear compressibility is affected by changing the aspect ratio of the elliptical void. The void ratio, $\{(voided\ area) / (total\ area)\}$ is kept constant in order to isolate the effect that changing the aspect ratio of the elliptical void has on linear compressibility. Additionally, the spacing gap between the voids is kept equal in the x and y directions ($g_y = g_x$ in Figure 7.4) and is altered in order to maintain a constant void ratio. In these analyses the void ratio has been fixed arbitrarily at 0.349 and the aspect ratio of the elliptical void has been varied between 1 and 6.25 where the major axis of the elliptical void lies on the global x -axis for all models.

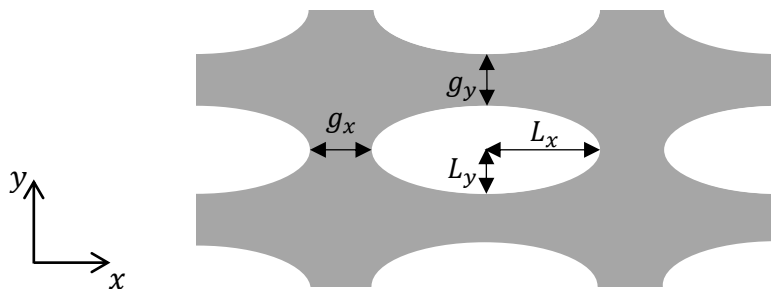


Figure 7.4 Layout of the model used to alter the ellipse aspect ratio

7.3.1.2 Mesh Convergence

The mesh convergence study has been carried out for the largest ellipse aspect ratio modelled, 6.25, as it is this model that has the thinnest wall sections (g_x and g_y in Figure 7.4 are minimum) and will hence require the densest mesh to ensure a converged result. It is assumed that the mesh selected for this geometry is suitable for all models analysed in this section. The number of elements is varied by altering the node spacing applied. As the geometry is relatively simple and the number of elements required to ensure convergence is also small, the spacing is applied uniformly across the model and no areas of the model are

assigned a greater mesh density. In the case analysed, it was found that the calculated linear compressibility was insensitive to the mesh density. The calculated elastic compliances and linear compressibility are shown in Figure 7.6 for different mesh densities and examples of the mesh are shown in Figure 7.5. As there are no thin wall sections in this model a low mesh density has provided converged results. The node spacing applied to the model with 908 elements was applied to all models reported in the following section.

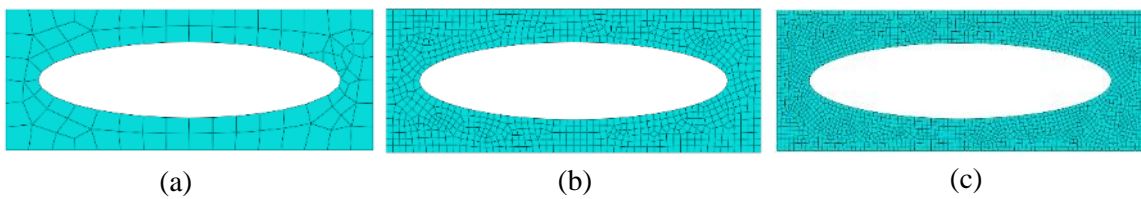


Figure 7.5 Meshes used in convergence study for regularly arranged elliptical voids; (a) 95 elements, (b) 905 elements and (c) 2250 elements

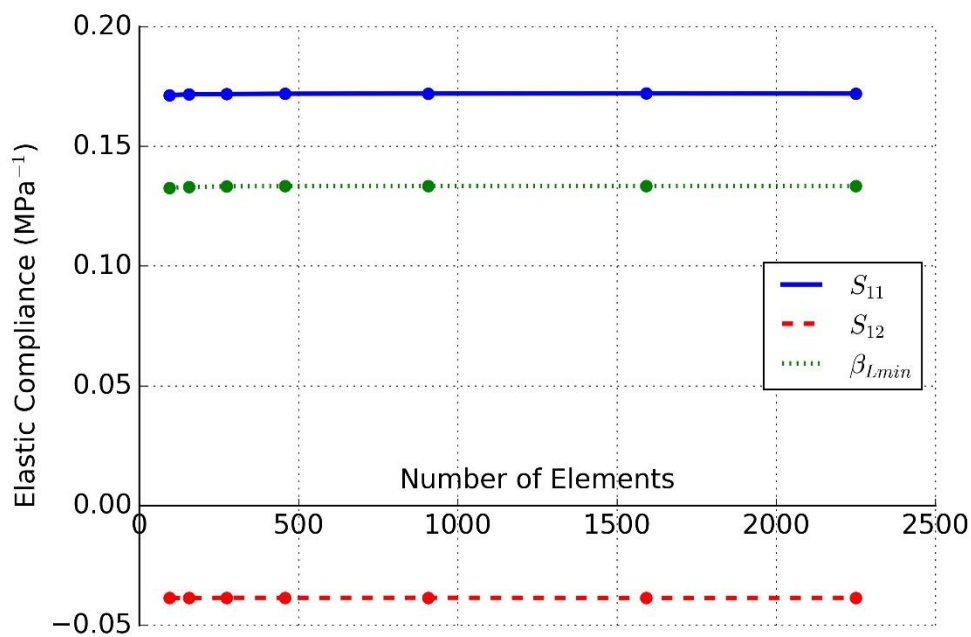


Figure 7.6 Sensitivity of the calculated elastic compliance and linear compressibility to mesh density where ellipse aspect ratio is 6.25

7.3.1.3 Results

The resulting elastic compliances and minimum linear compressibility are shown in Figure 7.7.

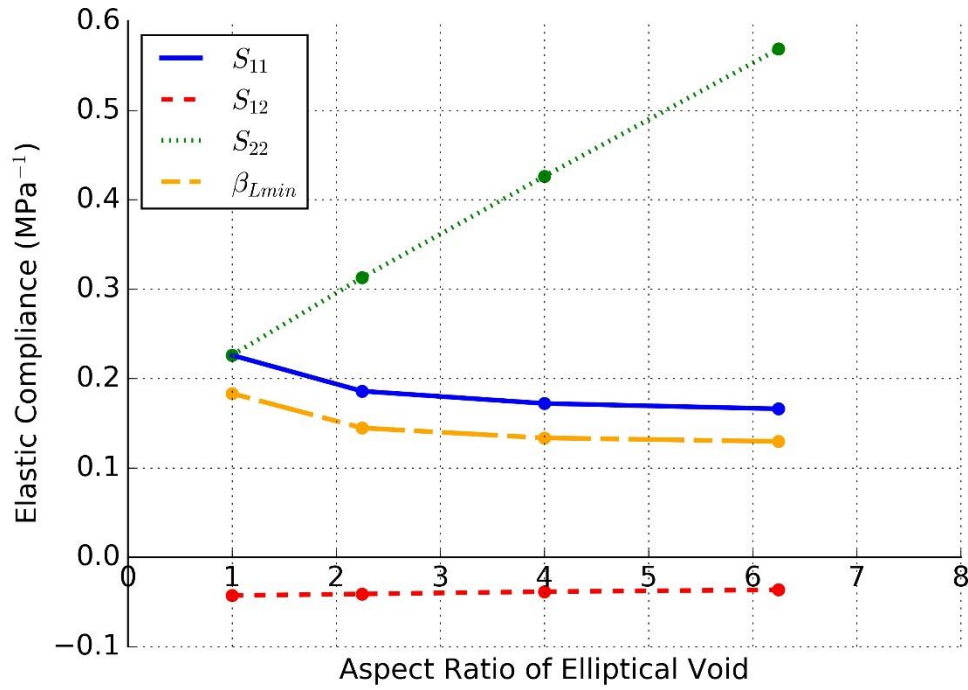


Figure 7.7 Elastic compliance and minimum linear compressibility for increasing elliptical void aspect ratio

Predictably, the stiffness of the material reduces in the y direction and increases in the x direction as the x dimension of the elliptical void increases. This is because the alignment of the remaining material increases in the x direction and this causes the constituent material to deform when loaded rather than the structure deforming via a mechanism. No negative values of linear compressibility have been reported in this study. The Von Mises and σ_{yy} stress plots where strain had been applied in the x direction are shown in Figure 7.8. The relative magnitude of stress is shown to be high in red sections and low in blue sections. It is likely that NLC was not observed in these structures because the large region of material, indicated in Figure 7.8, which is sited between the ellipses and which does not form part of the mechanism, resists compression of the structure in the y direction.

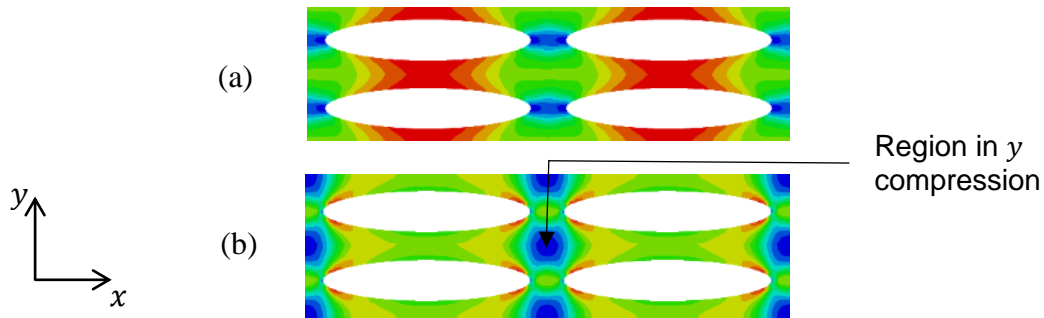


Figure 7.8 Von Mises (a) and σ_{yy} (b) stress contour plots showing four unit-cells of uniformly packed elliptical voids with an aspect ratio of 4 where a strain in the x direction has been applied.

It is plausible that NLC could occur in this structure if the void ratio were reduced as this would reduce the size of the zone that inhibits the NLC mechanism. Similarly, it is also possible that increasing the aspect ratio of the elliptical voids could create NLC. The region of the model that is restricting the formation of NLC can however be removed by altering the arrangement of the elliptical voids.

7.3.2 Alternative Arrangement of Elliptical Voids

7.3.2.1 Geometry

The linear arrangement of the elliptical voids created a region that inhibited the generation of lateral strain when the model was loaded along the major axis of the elliptical void. This section analyses a very similar set of models, although the elliptical voids are arranged hexagonally (see Figure 7.9). An arbitrarily selected value of 6.25 has been applied to the aspect ratio of the elliptical void.

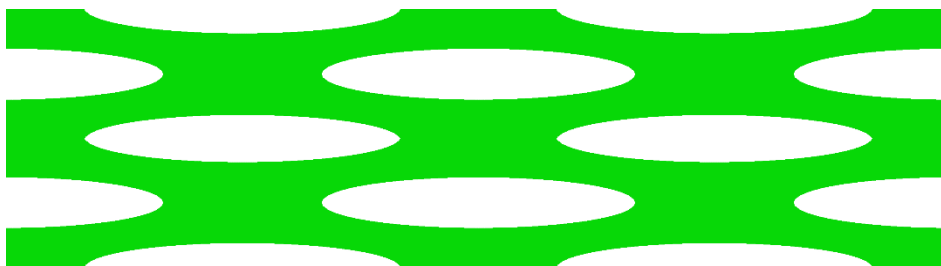


Figure 7.9 Hexagonally arranged elliptical voids

To achieve a suitable patterning, a hexagon has been fitted to the outer surface of the elliptical void. The area of the hexagon has been minimised where the x dimension of the hexagon is kept equal to that of the ellipse in order to create the best possible fit. This hexagonal geometry is shown plotted against the elliptical geometry in Figure 7.10.

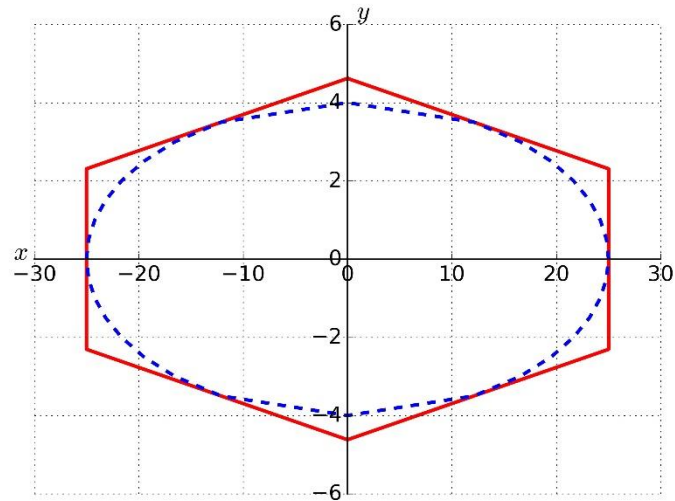


Figure 7.10 Plot of hexagon fitted to ellipse

The models are created by patterning the elliptical void with the hexagon. The void ratio of the model is altered by scaling the size of the hexagons. An example of how the elliptical voids are patterned inside the fitted hexagon is shown in Figure 7.11, where a scale factor of 1.1 is applied which results in a void ratio of 0.75.

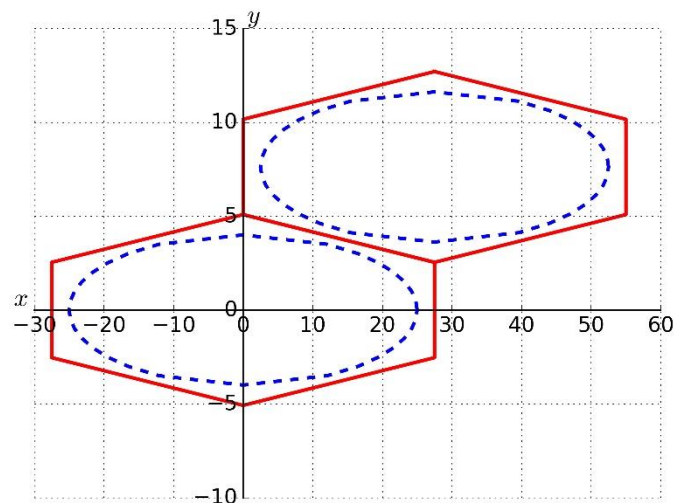


Figure 7.11 Patterned elliptical void (void-ratio = 0.750)

7.3.2.2 Mesh Convergence

As the proposed packing methodology has now changed, it is necessary to reconsider the mesh density required for accurate results to be extracted because the minimum wall thickness is now much smaller. Examples of the mesh are shown in Figure 7.12 and the calculated elastic compliance and linear compressibility of the model for increasing mesh density are shown Figure 7.13.

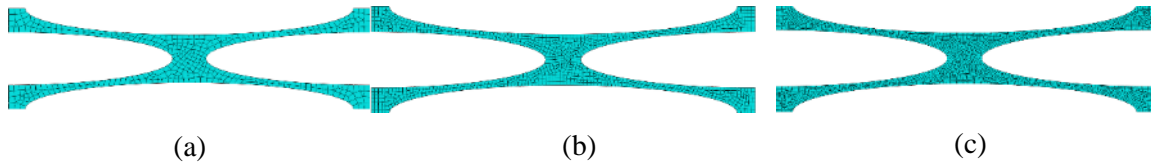


Figure 7.12 Examples of meshes used in convergence study for hexagonally arranged elliptical voids; (a) 408 elements, (b) 960 elements and (c) 2664 elements

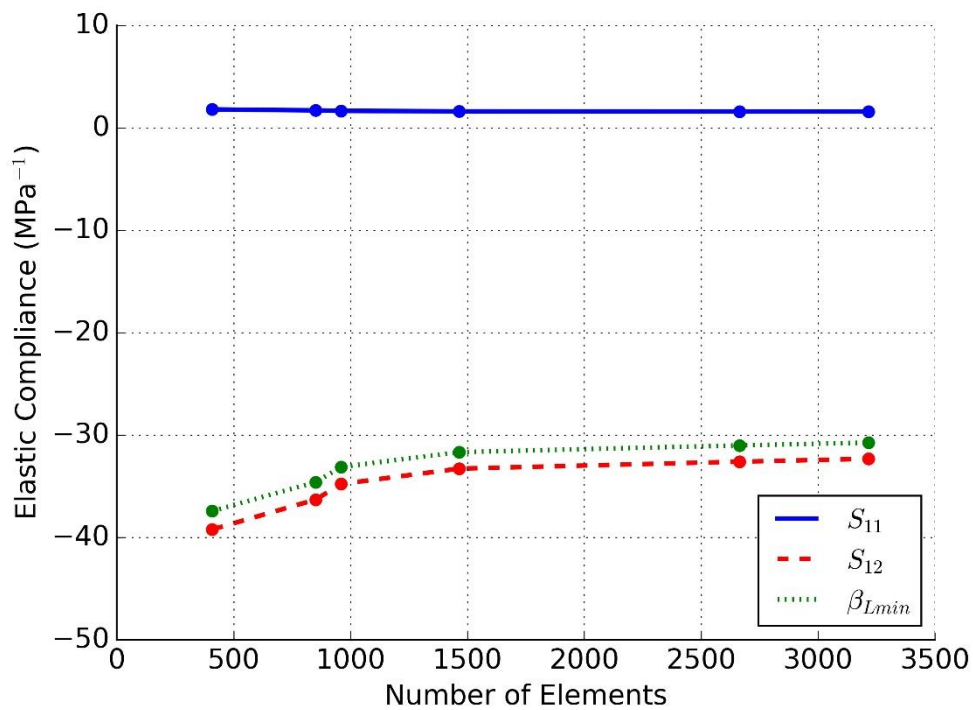


Figure 7.13 Sensitivity of the calculated elastic compliances and linear compressibility to mesh density where an ellipse aspect ratio is 6.25 is applied and the hexagonal spacing is a minimum

Due to the reduced minimum wall thickness in these models, the mesh density required to achieve a converged result has increased. The node spacing used where an element count of 2664 is achieved, is applied to all models analysed in the following section.

7.3.2.3 Results

NLC has been observed in all of the models containing hexagonally arranged elliptical voids and the elastic compliances and linear compressibility for different void ratios are shown in Figure 7.14. The structure becomes more compliant in both the x and the y directions as the void ratio increases. This is partly because there is less material present and partly because the structure deforms via a mechanism rather than having large strains observed within the constituent material. It can be deduced that the NLC mechanism observed in these models is very similar to that reported in Chapters 3-5. It can also be seen that as the elliptical voids come closer together, a) the structure resembles that of a hexagonal honeycomb and b) the NLC effect becomes more pronounced.

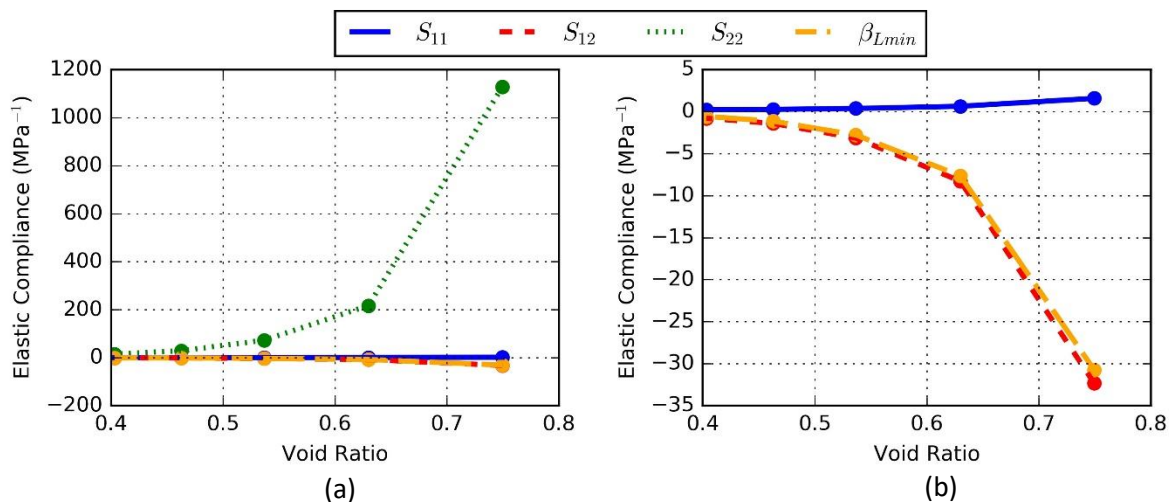


Figure 7.14 Elastic compliance and linear compressibility for various void ratios. S_{22} is plotted in (a) and has been removed in (b) to aid visualisation of the other values.

7.4 Conclusions

Although the NLC mechanism identified in this chapter can be likened to the “wine-rack” mechanism, the work in this chapter has also presented another means by which NLC can be achieved. It proposes that any material could be made into an NLC material if small

elliptical voids were inserted. It is also concluded that a three-dimensional material with NLC could be constructed where ellipsoidal voids were created. This is most likely to be possible in the production of foams. Ellipsoidal voids could be created if the foam were to be strained positively on a given axis and have the stresses relaxed via a tempering process. A very similar process has previously been applied to create auxetic foams successfully (Lakes, 1987).

Chapter 8

Conclusions

8.1 Introduction

The literature review concluded that the vast majority of the papers published on the subject of NLC were concerned with the behaviour of materials at an atomic level and that little work, other than the publication of the postulated “wine-rack” mechanism, had been carried out looking into NLC mechanisms relevant to larger length scales. Furthermore, it was found that very little effort had been directed at developing engineering materials that had NLC and it is logical to believe that while such progress is absent from the literature, industrial applications will not be developed. The work presented in this thesis has begun to remedy this issue. The key findings of this work are discussed in Section 8.2 which is split into two subsections representing the two strands that this thesis has sought to progress: macro NLC mechanisms and the discovery of other engineering materials that exhibit NLC. Following this, Section 8.3 makes recommendations for further work under the same two headings and Section 8.4 discusses possible applications of the property.

8.2 Key Findings

8.2.1 NLC Mechanisms

Two- and three-dimensional analyses of structures based on the “wine-rack” mechanism (Baughman et al., 1998a) have both been shown to exhibit NLC that is variable dependent upon the internal angle of the cross structure. Due to competing effects, the maximum NLC was found to occur when the internal angle was 25.9° in the two-dimensional structure and at 61.2° in the three-dimensional structure within a tetragonal symmetry, and NAC was found to be maximum when this angle was 26.6° . Arranging a similar structure so that it conformed to an orthorhombic symmetry allowed the maximum absolute NLC to be different in three orthogonal directions, although the maximum absolute values of NLC were

gained using a tetragonal symmetry. Further results also showed that these values of absolute linear compressibility could be increased if spacers were added to the structure. The overall conclusion from this idealised study was that the tendency of the beam to rotate rather than compress axially was what drove NLC and furthermore, the angle at which the rigid beams are oriented plays a large part in driving NLC. This understanding could be used to help progress the search for more NLC materials.

The high strain behaviour of these structures was also investigated and results showed that the absolute NLC is reduced because, as the beam becomes more deformed, it will bend inwards, which causes the unit cell to shrink. The compressibility capacity of some of these structures was also assessed. It is also important to realise that the absolute and normalised compressibilities must be considered in parallel as maxima do not occur simultaneously, and a trade-off must be found.

Further analysis of a helically wound braid and elliptically voided material suggested that they displayed a different NLC mechanism (not the wine-rack). However on closer inspection, the underlying mechanism is found to be the same in both instances. The helically woven fibres are rotating in such a way that they become aligned with the tube axis and the elliptically voided structure resembles an elliptical honeycomb (when the voids are positioned closely and arranged hexagonally) and as such, have a similar appearance to the two-dimensional beam structures that have undergone high strains (documented in Chapter 6). It is therefore concluded that although an in-depth analysis of different ways of producing NLC have been investigated, the underlying NLC mechanism is still the “wine-rack” in all cases.

8.2.2 Engineering Materials

Knowledge gained from the analysis of the “wine-rack” mechanism directed a literature search that led to the discovery of a number of materials exhibiting NLC which were previously unknown to the research community. These included two drawn polymers, a number of wood species, machine paper and a theorised carbon fibre reinforced plastic of a specific lay-up

configuration. These discoveries have increased the possible scope for applications to be developed for NLC materials as the manufacturing potential has been increased.

Further to this, the development of an analytical model, coupled with experimental investigation, of helical structures achieved via braiding, has created an understanding of how the high positive Poisson's ratio is achieved in certain configurations of helices. Although the linear compressibility of these structures could not be determined by any means, the presence of NLC has been confirmed. Further investigation has also confirmed, for the first time, that it is possible to create a material with NLC by placing specifically arranged elliptical voids into a sheet of homogenous material. It is hoped that these results have also increased the potential for such structures to be manufactured.

8.3 Further Work

8.3.1 NLC Mechanisms

The work in this thesis constitutes an in-depth analysis of the "wine-rack" and the fundamentals of the mechanism have been carefully examined. Further studies could however build on this work, for instance the structures modelled in Chapter 3-6 could be modelled with solid elements and the effect of plasticity at high strains could also be analysed. Further to this, experimental testing of rapid prototyped structures could be compared with the theoretical results. The possibility of creating NLC materials by carefully creating a structure with an elastic instability should also be investigated. Previous research has shown that such an approach can produce auxetic materials (Bertoldi et al., 2010, Lakes and Drugan, 2002).

8.3.2 Engineering Materials

There is a great deal of scope for further analysis and testing of the materials that have been newly recognised in this thesis as having NLC. As the drawing of polymers can impart NLC to a material, this process should be more thoroughly investigated with the aim of creating NLC and efforts could also be made to optimise the raw polymer structure with respect to creating an axis of NLC. Similar efforts could also be made to develop the NLC properties of

CFRP. The study documented here is only a scoping calculation and the doors have been opened for research to be carried out that could develop CFRP with NLC. The potential for further research into various helical structures has been realised within this thesis. In particular, it is envisaged that composite materials could be constructed whereby braids similar to the ones analysed in this thesis could be embedded within a comparatively compliant matrix in order to create a composite with NLC. Thanks to the analysis of the elliptically voided materials, foams with NLC can also be envisaged, as it is predictable that a material with specifically arranged and sized ellipsoidal voids will have NLC. Therefore if conventional foams were to be loaded axially and then tempered such that the stresses relaxed, it could be possible to produce a foam with partially aligned ellipsoidal voids which therefore has the possibility of exhibiting NLC.

8.4 Applications

Due to NLC research still being in a relatively early stage, industrial applications of the property are yet to be fully realised while the elastically equivalent property, stretch densification, has found several uses (PDQ Lifting, 2015, Allen Medical Systems, 2015). A few recurring suggestions appear in the literature, these include: force amplifiers (Baughman et al., 1998a), shock absorbing materials, acoustic dampeners, pressure sensors (Kang et al., 2015) and artificial muscles (Aliev et al., 2009). In a non-direct application, the overlap between materials exhibiting superconductivity and NLC is also something that could be exploited in the future development and tuning of superconductors.

Aside from this, no immediate applications for NLC materials are envisaged after completion of this thesis. The work documented in this thesis has, however, progressed the field of NLC research along the road to eventual engineering applications. This is evidenced in the greater mechanical understanding of the wine rack mechanism and the number of engineering materials that have been identified as having NLC. The future of NLC applications is still unclear but the knowledge provided here could play a part in the property's eventual application.

Appendix A

Derivation of Analytical Formulae for 2D Beam Structure with Spacer

The inclusion of the spacer in the 2D structure analysed in Chapter 2 is accounted for by altering the expressions for the unit-cell dimensions, A and B , previously defined in Equations 3.4 and 3.5. Figure A1 shows newly introduced parameters γ_A and γ_B , which are the spaced distances in the x and y directions respectively.

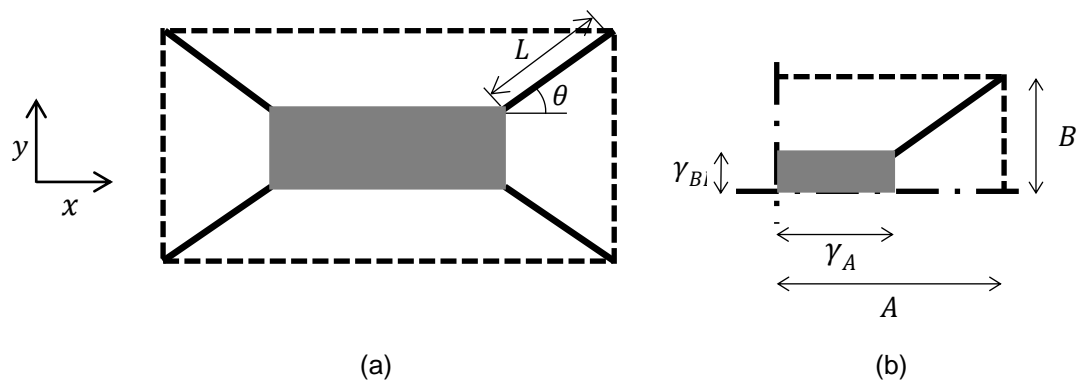


Figure A1 Repeating (a) and primitive (b) unit-cells for a 2D rectangular cross structure with spacer

The unit-cell dimensions, A and B now become

$$B = \sin(\theta) L + \gamma_B \tag{A.1}$$

and

$$A = \cos(\theta) L + \gamma_A. \tag{A.2}$$

The equations for linear compressibility therefore become

$$\beta_x = \frac{L^3 \cos(\theta) \sin(\theta)}{12EI} - \frac{[(\sin(\theta) L + \gamma_B) \sin^2(\theta)] L^3}{12EI(\cos(\theta) L + \gamma_A)} - \frac{L \sin(\theta) \cos(\theta)}{E\phi} - \frac{[(\sin(\theta) L + \gamma_B) \cos^2(\theta)] L}{E\phi(\cos(\theta) L + \gamma_A)} \quad \text{A.3}$$

and

$$\beta_y = \left[\frac{L^3 \sin(\theta) \cos(\theta)}{12EI} - \frac{[(\cos(\theta) L + \gamma_A) \cos^2(\theta)] L^3}{12EI(\sin(\theta) L + \gamma_B)} - \frac{L \sin(\theta) \cos(\theta)}{E\phi} - \frac{[(\cos(\theta) L + \gamma_A) \sin^2(\theta)] L}{E\phi(\sin(\theta) L + \gamma_B)} \right] \quad \text{A.4}$$

Appendix B

Derivation of Analytical Formulae for 3D Beam Structure

B1 Introduction

The derivation of the analytical formulae that calculate the linear compressibility of the three-dimensional tetragonal structures discussed in Chapters 4 and 5 are presented in this appendix. The assumptions and methodology used here are broadly the same as those documented in Appendix A, as the formulae derived here are an expansion of those derived in Appendix A.

Section B2 illustrates how the initial 3D formula was arrived at and Section B3 shows how the formula can be modified to allow for the addition of spacers documented in Chapter 5.

B2 Derivation

Primitive Unit-Cell and Dimensions

The unit-cell is defined using tetragonal symmetry with internal angles μ and α as illustrated in Figure B1. μ is a variable in these derivations and α is fixed at 45° in order for the symmetry to remain tetragonal.

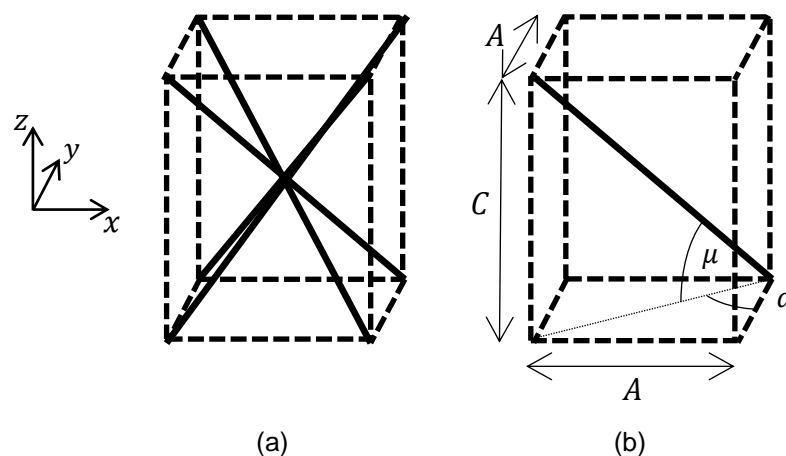


Figure B1 Repeating (a) and primitive (b) unit-cells for 3D tetragonal structure

The dimensions of the primitive unit-cell, A and C , illustrated in Figure B1 are expressed as

$$A = L \cos(\mu) \sin(\alpha) \quad \text{B.1}$$

and

$$C = L \sin(\mu). \quad \text{B.2}$$

Pressure Forces and Boundary Conditions

Similarly to the two-dimensional derivation, the unit-cell is simulated as being in the centre of a large array undergoing hydrostatic pressurisation. The forces acting on the structure are proportional to the areas of the faces of the primitive unit-cell (see Figure B2(a)). The forces are assumed to act on Node K and a cantilever boundary condition is applied to Node J (see Figure B2(b)).

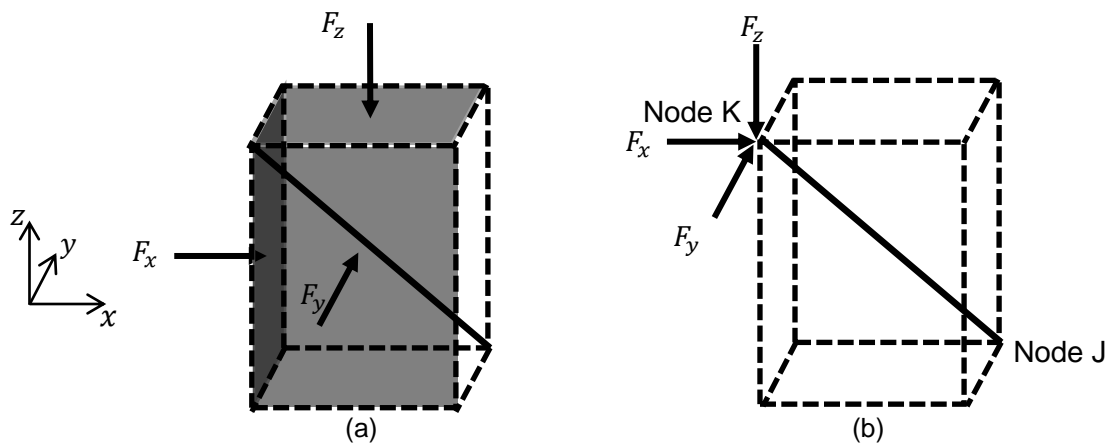


Figure B2 (a) Pressure loading on primitive unit-cell (a) Resulting forces acting on primitive unit-cell

The forces F_x , F_y and F_z acting on the structure shown in Figure B2(b) in the x , y and z -directions respectively are calculated using

$$F_z = A^2 P \quad \text{B.3}$$

and

$$F_x = F_y = CAP$$

B.4

where P is the applied hydrostatic pressure.

Forces Resolved to Beam Axes

The forces acting on the beam can be resolved into a local axis system for the beam. Two forces are resolved, the axial force, F_a , and a force active transverse to the beam, F_T . Both are illustrated in Figure B3.

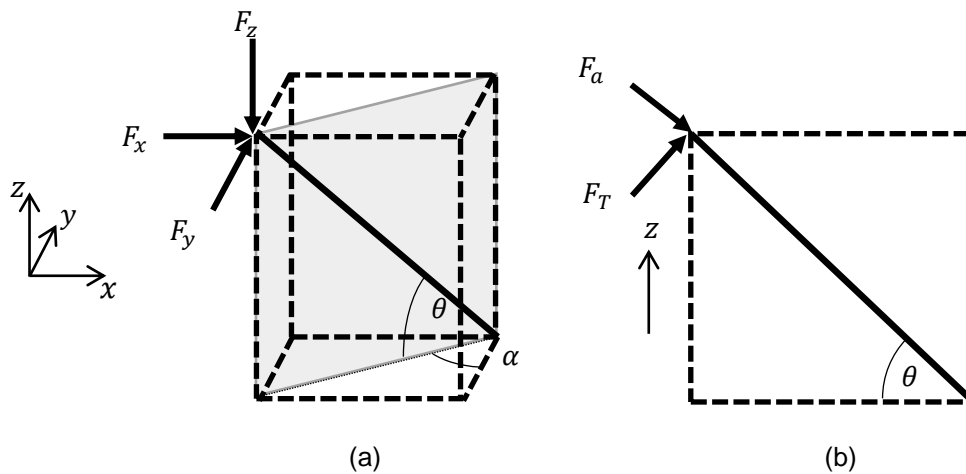


Figure B3 (a) Orthographic illustration of forces acting on beam (b) Illustration of forces acting on beam in plane indicated in (a)

The two forces are defined as

$$F_a = F_z \sin(\mu) + 2F_x \cos(\alpha) \cos(\mu) \quad \text{B.5}$$

and

$$F_T = -F_z \cos(\mu) + 2F_x \cos(\alpha) \sin(\mu) \quad \text{B.6}$$

Local Beam Deflections

Standard formulae and Euler mechanics determine the axial, δ_a and transverse δ_T displacements of the beam which are defined as

$$\delta_a = \frac{F_a L}{E\phi} \quad \text{B.7}$$

and

$$\delta_T = \frac{F_T L^3}{12EI} \quad \text{B.8}$$

Deflections Resolved to Global Coordinate System

Displacements are then resolved back to the global coordinate system. The displacements in the x , y and z directions are defined as

$$\delta_x = -\delta_a \cos(\mu) \sin(\alpha) + \delta_T \sin(\mu) \sin(\alpha) \quad \text{B.9}$$

$$\delta_y = -\delta_a \cos(\mu) \cos(\alpha) + \delta_T \sin(\mu) \cos(\alpha) \quad \text{B.10}$$

and

$$\delta_z = -\delta_x \sin(\mu) + \delta_T \cos(\mu) \quad \text{B.11}$$

respectively.

Strains

Strains in the x and z directions are defined as

$$\varepsilon_x = \varepsilon_y = \frac{\delta_x}{A} \quad \text{B.12}$$

and

$$\varepsilon_z = \frac{\delta_z}{C} \quad \text{B.13}$$

respectively, where the strains in the x and y directions are equal.

Linear Compressibility

Linear compressibilities in the x and z directions are defined as

$$\beta_x = \beta_y = \frac{\varepsilon_x}{P} \quad \text{B.14}$$

and

$$\beta_z = \frac{\varepsilon_z}{P} \quad \text{B.15}$$

respectively, where the linear compressibilities in the x and y directions are equal.

Finally, by rearranging Equations B.1 to B.15, the final equations for linear compressibility are found to be

$$\beta_x = -\frac{[3L^2 \sin(\mu) \cos^2(\mu)]}{2E\phi} + \frac{[-L^4 \cos^2(\mu)\sin(\mu) + 2L^4 \sin^2(\mu)]}{24EI} \quad \text{B.16}$$

and

$$\beta_z = -\frac{[3L^2 \sin(\mu) \cos^2(\mu)]}{2E\phi} + \frac{[-L^4 \cot(\mu) \cos^3(\mu) + 2L^4 \sin(\mu) \cos^2(\mu)]}{24EI} \quad \text{B.17}$$

B3 Spacer Modification

The inclusion of the spacer is accounted for in the analytical derivation by altering the expressions for the unit-cell dimensions, A and C , previously defined in Equations B1 and B2. Figure B4 shows the newly introduced parameters γ_A and γ_C , which are the spaced distances in the x and y , and z directions respectively.

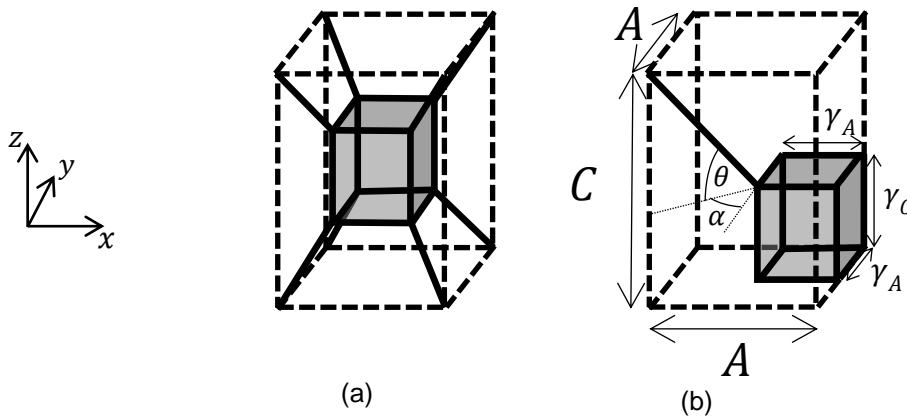


Figure B4 Repeating (a) and primitive (b) unit-cells of 3D tetragonal beam model with spacer

The unit-cell dimensions, A and C now become

$$A = L \cos(\mu)\sin(\alpha) + \gamma_A \quad \text{B.18}$$

and

$$C = L \sin(\mu) + \gamma_C \quad \text{B.19}$$

respectively.

By rearranging the Equation B3 to B19, expressions for linear compressibility therefore become

$$\begin{aligned}
\beta_x = & -\frac{L^2 \left[\sin(\mu) \cos^2(\mu) + \frac{1}{2} \cos^2(\mu) \sin(\mu) \right]}{E\phi} - \frac{L[\gamma_A \sin(\mu) \cos(\mu) \sin(\alpha) + \gamma_C \cos^2(\mu)]}{E\phi} \\
& - \frac{L^3 \left[\frac{L}{2} \cos^2(\mu) \sin(\mu) + \gamma_A \cos(\mu) \sin(\mu) \sin(\alpha) \right]}{12EI} \\
& + \frac{L^3 [L \sin^3(\mu) + \gamma_C \sin^2(\mu)]}{12EI}
\end{aligned} \tag{B.20}$$

and

$$\begin{aligned}
\beta_z = & -\frac{L \sin(\mu) (L \cos(\mu) \sin(\alpha) + \gamma_A)^2}{E\phi (L \sin(\mu) + \gamma_C)} + \frac{[L^2 \cos(\mu) \sin^2(\alpha) \sin(2\mu)]}{E\phi} \\
& + \frac{L \gamma_A \cos(\alpha) \sin(2\mu)}{E\phi} - \frac{L^3 \cos(\mu) (L \cos(\mu) \sin(\alpha) + \gamma_A)^2}{12EI (L \sin(\mu) + \gamma_C)} \\
& + \frac{L^4 \sin(2\mu) + 4L^3 \gamma_A \cos(\alpha) \sin(\mu)}{24EI}
\end{aligned} \tag{B.21}$$

Appendix C

Method for Calculating Linear Compressibility in Orthorhombic Networks

C1 Introduction

The analytical methodology used to calculate the linear compressibility of the three-dimensional orthorhombic structures discussed in Chapter 4 is presented here.

C2 Analytical Methodology

C2.1 Preamble

Due to the increased complexity involved, the methodology used to determine the linear compressibility of orthorhombic structures is different to that used for the two-dimensional rectangular and three-dimensional tetragonal structures. The assumptions applied in Appendices A and B are still applicable, although the linear compressibility is calculated from derived expressions for the elastic compliances.

C2.2 Derivation

Primitive Unit-Cell and Dimensions

An orthorhombic unit-cell of internal angles μ and α is defined as shown in Figure C1 where both μ and α are variable.

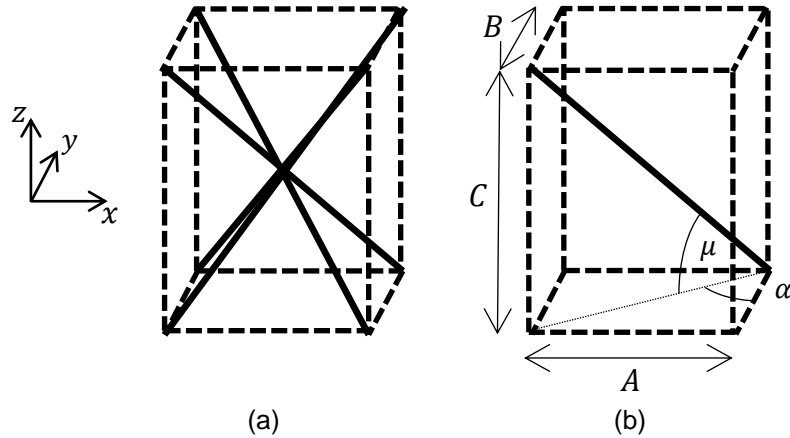


Figure C1 Repeating (a) and primitive (b) unit-cells for a type III beam structure arranged within an orthorhombic symmetry

The dimensions of the unit-cell, A , B and C illustrated in Figure C1 are equal to,

$$A = \cos(\mu)\sin(\alpha) \tag{C.1}$$

$$B = \cos(\mu)\cos(\alpha) \tag{C.2}$$

and

$$C = \sin(\mu) L \tag{C.3}$$

respectively.

Uni-axial Loading

An arbitrary stress, σ_{33} , is applied to the unit-cell in the z direction, as indicated in Figure C2(a). The total force, F_3 assumed to act on the beam as shown in Figure C2(b) is proportional to the area of the face indicated in Figure C2(a) and is equal to

$$F_3 = \sigma_{33}AB \tag{C.4}$$

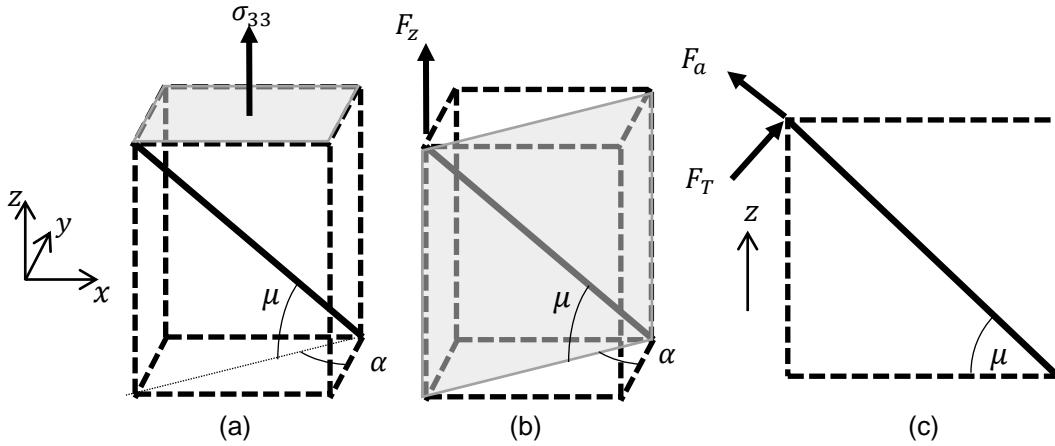


Figure C2 Beam loading and forces resolved to local beam axes

Forces Resolved to Local Beam Axes

The forces acting on the beam are resolved onto the local axes of the beam. Two forces are present, an axial force F_a and a transverse force F_T as indicated in Figure C2(c).

These are equal to

$$F_a = \sin(\mu)F_z \quad \text{C.5}$$

and

$$F_T = \cos(\mu)F_z \quad \text{C.6}$$

Beam Deflections

Beam deflections are calculated using standard formulae and Euler theory. The axial deflection, δ_a , and transverse deflection, δ_T are calculated using

$$\delta_a = \frac{F_a L}{E\phi} \quad \text{C.7}$$

and

$$\delta_T = \frac{F_T L^3}{12EI} \quad \text{C.8}$$

Deflections Resolved to Global Coordinate System

Deflections are resolved to the global coordinate system using appropriate trigonometry functions. The deflections on the x, y and z axes (δ_x , δ_y and δ_z respectively) are

$$\delta_x = \delta_a \cos(\mu) \sin(\alpha) + \delta_T \sin(\mu) \sin(\alpha) \quad \text{C.9}$$

$$\delta_y = \delta_a \cos(\mu) \cos(\alpha) + \delta_T \sin(\mu) \cos(\alpha) \quad \text{C.10}$$

and

$$\delta_z = \delta_A \sin(\mu) + \delta_T \cos(\mu) \quad \text{C.11}$$

respectively.

Strains

Standard formulae are used to calculate strains in the x , y and z directions (ε_x , ε_y and ε_z respectively) and are equal to

$$\varepsilon_x = \frac{\delta_x}{A} \quad \text{C.12}$$

$$\varepsilon_y = \frac{\delta_y}{B} \quad \text{C.13}$$

and

$$\varepsilon_z = \frac{\delta_z}{C} \quad \text{C.14}$$

respectively.

Elastic Compliances

Standard formulae are used to determine the elastic compliances of the model as follows:

$$S_{13} = \frac{\varepsilon_x}{\sigma_z}, \quad \text{C.15}$$

$$S_{23} = \frac{\varepsilon_y}{\sigma_z} \quad \text{C.16}$$

and

$$S_{33} = \frac{\varepsilon_z}{\sigma_z} \quad \text{C.17}$$

Other required elastic compliances are calculated by manipulating the two angles governing the unit-cell, α and μ , (see Figure C1(b)) in order to create unit-cells that are a rotation of the original.

Linear Compressibility

Linear compressibility is then calculated using

$$\beta_L = (S_{11} + S_{12} + S_{13})L_x^2 + (S_{22} + S_{21} + S_{23})L_y^2 + (S_{33} + S_{13} + S_{23})L_z^2,$$

C.18
(Nye,
1964)

as discussed in Chapter 4.

Appendix D

Current NLC materials

Name	Chemical Formula	Symmetry	β_V (TPa ⁻¹)	β_{LMin} (TPa ⁻¹)	β_{LMax} (TPa ⁻¹)	β_{LMin}/β_V	β_{LMax}/β_V	Reference
Baughman Review of Landolt-Borstein Table								
Mercurous iodide	Hg ₂ I ₂	Tetragonal	81.12	-11.39	46.26	-0.14	0.57	
Mercurous bromide	Hg ₂ Br ₂	Tetragonal	64.87	-3.24	34.05	-0.05	0.52	
Selenium	Se	Trigonal	96.84	-19.89	58.36	-0.21	0.6	
Tellurium	Te	Trigonal	48.42	-4.03	26.22	-0.08	0.54	
3-Methyl 4-nitropyridine 1-oxide	C ₆ N ₂ O ₃ H ₆	Orthorhombic	259.3	-112.3	213.3	-0.43	0.82	
m-Dihydroxybenzene	C ₆ H ₄ (OH) ₂	Orthorhombic	112.4	-22.78	116.3	-0.19	0.95	
Cadmium formate	Cd(COOH) ₂	Orthorhombic	53.73	-13.83	56.64	-0.26	1.05	
Caesium biphthalate	C ₆ H ₄ COOHCOOCs	Orthorhombic	97.99	-9.28	55.22	-0.09	0.56	
Calcium formate	Ca(COOH) ₂	Orthorhombic	48.45	-8.04	38.41	-0.17	0.79	
Tris-sarcosine calcium chloride	(CH ₃ NHCH ₂ COOH) ₃ CaCl ₂	Orthorhombic	62.7	-3.95	43.64	-0.06	0.7	
Cesium dihydrogen phosphate	CsH ₂ PO ₄	Monoclinic	189.5	-262.9	430.2	-1.39	2.27	(Prawer et al., 1985)
Lanthanum niobate	LaNbO ₄	Monoclinic	10.32	-23.27	32.74	-2.25	3.17	
Ethylene Diamine Tartrate	C ₆ H ₁₄ N ₂ O ₆	Monoclinic	62.71	-6.04	53.42	-0.1	0.85	
Taken From Landolt-Borstein Tables								
Urea	CH ₄ N ₂ O	Tetragonal	86.15	-36.56	61.35	-0.42	0.71	
Arsenic	As	Trigonal	17.97	-4.91	27.79	-0.27	1.55	
Silver thallium selenide	AgTlSe ₂	Orthorhombic	24.42	-16.85	22.29	-0.69	0.91	
Sodium ammonium tartrate tetrahydrate	NaNH ₄ C ₄ H ₄ O ₆ * 4H ₂ O	Orthorhombic	34.17	-1.78	23.77	-0.05	0.7	
Rubidium biphthalate	C ₆ H ₄ (COOH) (COORb)	Orthorhombic	89.07	-1.3	51.37	-0.01	0.53	

Betaine phosphate	C ₅ H ₁₄ NO ₆ P	Monoclinic	102.7	-9.35	78.05	-0.09	0.76	
Aegirite-Augite	(Ca,Na)(Mg,Fe,Al,Ti)(Si,Al) ₂ O ₆	Monoclinic	11.71	-0.47	7.05	-0.04	0.6	
Bismuth vanadate	BiO ₄ V	Monoclinic	16.23	-0.25	9.11	-0.02	0.56	
Ammonium tetroxalate dihydrate	(NH ₄)H ₃ (C ₂ O ₄) ₂ .2H ₂ O	Triclinic	83.08	-9.78	81.19	-0.12	0.98	
Potassium tetroxalate dihydrate	C ₄ H ₇ KO ₁₀	Triclinic	74.93	-7.63	72.47	-0.1	0.97	
Materials Found within Literature								
Europium iron arsenide	EuFe ₂ As ₂	Tetragonal	25.4	-12	35	-0.47	1.38	(Uhoya et al., 2010)
Platinum sulphide	PtS	Tetragonal	6.9	-0.15	3.52	-0.02	0.51	(Marmier et al., 2010b)
Selenium	Se	Trigonal	39.7	-14.3	31.9	-0.36	0.8	(McCann and Cartz, 1972)
Silver hexacyanocobaltate-I	Ag ₃ [Co(CN) ₆]-I	Trigonal	154	-76	115	-0.49	0.75	(Goodwin et al., 2008)
Silver hexacyanocobaltate-II	Ag ₃ [Co(CN) ₆]-II	Monoclinic	19.5	-5.3	15.2	-0.27	0.78	(Goodwin et al., 2008)
-	KMn[Ag(CN) ₂] ₃	Trigonal	78	-12	33.2	-0.15	0.43	(Cairns et al., 2012)
zinc dicyanoaurate-I	Zn[Au(CN) ₂] ₂ -I	Hexagonal	62	-42	52	-0.68	0.84	(Cairns et al., 2013)
zinc dicyanoaurate-II	Zn[Au(CN) ₂] ₂ -II	Hexagonal	26	-6	16	-0.23	0.62	(Cairns et al., 2013)
Methanol monohydrates	CH ₃ OH.H ₂ O	Orthorhombic	266	-3.8	205	-0.01	0.77	(Fortes et al., 2011)
Lanthanum niobate	LaNbO ₄	Monoclinic	9	-10	70	-1.11	7.78	(Mariathasan et al., 1985)
Selenium	Se	Trigonal	7.00	-2.50	12.00	-0.36	1.71	(McCann and Cartz, 1972)
Tellurium	Te	Trigonal	25.40	-1.80	13.60	0.54	-0.07	(Jamieson and McWhan, 1965)
MIL-140A	ZrO(O ₂ C-C ₅ H ₄ -CO ₂)	Monoclinic	-	-3.0	27.8	-	-	(Ryder et al., 2016)
MIL-140C	ZrO(O ₂ C-C ₁₂ H ₈ -CO ₂)	Monoclinic	-	-10	52.5	-	-	(Ryder et al., 2016)
Silver tricyanomethanide (NAC)	Ag[C(CN) ₃]	Orthorhombic	51	-7.5	66	-0.15	1.29	(Hodgson et al., 2014)
TiGaSe ₂ (NAC)	TiGaSe ₂	Orthorhombic	43.26	4.99	33.28	0.12	0.77	(Seyidov and Suleymanov, 2010)
Materials Documented in Chapter 6								
Drawn PP	-	Hexagonal	590.9	-42.37	316.63	-0.07	0.54	(Chan et al., 1978)
Drawn PVC	-	Hexagonal	190.5	-15.15	105.3	-0.08	0.54	(Rawson and Rider, 1974)
Machine Paper	-	Orthorhombic	1490	-175	1520	-0.01	1.02	(Mann et al., 1979)
Ash	-	Orthorhombic	745.4	-11.9	585.2	-0.02	0.79	(Earmon, 1948)

Aspen	-	Orthorhombic	1668.1	-424.7	2049.5	-0.25	1.23	(Bodig, 1973)
Oak	-	Orthorhombic	631.4	-5.1	505.7	-0.01	0.80	(Guitard, 1987)
Walnut	-	Orthorhombic	1106.7	-10.8	926	-0.01	0.84	(Earmon, 1948)

Bibliography

- ADAMSKA, A., HAVELA, L., SURBLE, S., HEATHMAN, S., POSPÍŠIL, J. & DANIŠ, S. 2010. Pressure effect on the crystal lattice of unconventional superconductor UCoGe. *Journal of Physics: Condensed Matter*, 22, 275603.
- ALDERSON, A. 1999. A Triumph of Lateral Thought. *Chemistry & Industry*, 17, 384-391.
- ALDERSON, A., DAVIES, WILLIAMS, EVANS, ALDERSON, K. L. & GRIMA 2005a. Modelling of the mechanical and mass transport properties of auxetic molecular sieves: an idealised organic (polymeric honeycomb) host-guest system. *Molecular Simulation*, 897-905.
- ALDERSON, A. & EVANS, K. 2001. Rotation and dilation deformation mechanisms for auxetic behaviour in the alpha-cristobalite tetrahedral framework structure. *Physics and Chemistry of Minerals*, 711-718.
- ALDERSON, A., P.DAVIES, K.EVANS, K.L.ALDERSON & GRIMA 2005b. Modelling of the mechanical and mass transport properties of auxetic molecular sieves: an idealised inorganic (zeolitic) host-guest system. *Molecular Simulation*, 889-896.
- ALDERSON, K. L., FITZGERALD, A. & EVANS, K. E. 2000a. The strain dependent indentation resilience of auxetic microporous polyethylene. *Journal of Materials Science*, 35, 4039-4047.
- ALDERSON, K. L., PICKLES, A. P., NEALE, P. J. & EVANS, K. E. 1994. Auxetic polyethylene: The effect of a negative poisson's ratio on hardness. *Acta Metallurgica et Materialia*, 42, 2261-2266.
- ALDERSON, K. L., SIMKINS, V. R., COENEN, V. L., DAVIES, P. J., ALDERSON, A. & EVANS, K. E. 2005c. How to make auxetic fibre reinforced composites. *physica status solidi (b)*, 242, 509-518.
- ALDERSON, K. L., WEBBER, R. S. & EVANS, K. E. 2000b. Novel variations in the microstructure of auxetic ultra-high molecular weight polyethylene. Part 2: Mechanical properties. *Polymer Engineering & Science*, 40, 1906-1914.

- ALDERSON, K. L., WEBBER, R. S., MOHAMMED, U. F., MURPHY, E. & EVANS, K. E. 1997. An experimental study of ultrasonic attenuation in microporous polyethylene. *Applied Acoustics*, 50, 23-33.
- ALIEV, A. E., OH, J., KOZLOV, M. E., KUZNETSOV, A. A., FANG, S., FONSECA, A. F., OVALLE, R., LIMA, M. D., HAQUE, M. H., GARTSTEIN, Y. N., ZHANG, M., ZAKHIDOV, A. A. & BAUGHMAN, R. H. 2009. Giant-Stroke, Superelastic Carbon Nanotube Aerogel Muscles. *Science*, 323, 1575-1578.
- ALLEN MEDICAL SYSTEMS, I. 2015. Available: <http://www.allenmedical.com/>.
- AVELLANEDA, M. & SWART, P. J. 1998. Calculating the performance of 1–3 piezoelectric composites for hydrophone applications: An effective medium approach. *The Journal of the Acoustical Society of America*, 103, 1449-1467.
- BARNES, D., MILLER, W., EVANS, K. E. & MARMIER, A. 2012. Modelling negative linear compressibility in tetragonal beam structures. *Mechanics of Materials*, 46, 123-128.
- BAUGHMAN, STAFSTROM, CUI & DANTAS 1998a. Materials with Negative Compressibilities in One or More Directions. *phys. stat. sol*, 2, 236-238.
- BAUGHMAN, R., J.SHACKLETTE, A.ZAKHIDOV & STAFSTROM, S. 1998b. Negative Poisson's ratios as a common feature of cubic metals. *Nature*, 362-365.
- BERTOLDI, K., REIS, P. M., WILLSHAW, S. & MULLIN, T. 2010. Negative Poisson's ratio behavior induced by an elastic instability. *Advanced Materials*, 22, 361-366.
- BINNS, J., KAMENEV, K., MARRIOTT, K., MCINTYRE, G., MOGGACH, S., MURRIE, M. & PARSONS, S. 2016. A Non-Topological Mechanism for Negative Linear Compressibility. *Chemical Communications*.
- BODIG, J. 1973. Prediction of elastic parameters for wood. *Wood Science*, 5, 249-264.
- BRAGANZA L.F., W. D. L. 1986. Structural Changes in Lipid Bilayers and Biological Membranes Caused by Hydrostatic Pressure, *Biochemistry*, 25, 7484-7488.
- BRIDGMAN, P. W. 1922. The compressibility of metals at high temperatures. *Physics*.

- BRIDGMAN, P. W. Compressibilities and pressure coefficients of resistance of elements, compounds, and alloys, many of them anomalous. *Proceedings of the American Academy of Arts and Sciences*, 1933. JSTOR, 27-93.
- CADDOCK, B. D. & EVANS, K. E. 1989. Microporous materials with negative Poisson's ratios. I. Microstructure and mechanical properties. *Journal of Physics D: Applied Physics*, 22, 1877.
- CAIRNS, A. B., CATAFESTA, J., LEVELUT, C., ROUQUETTE, J., VAN DER LEE, A., PETERS, L., THOMPSON, A. L., DMITRIEV, V., HAINES, J. & GOODWIN, A. L. 2013. Giant negative linear compressibility in zinc dicyanoaurate. *Nat Mater*, 12, 212-216.
- CAIRNS, A. B. & GOODWIN, A. L. 2015. Negative linear compressibility. *Physical Chemistry Chemical Physics*, 17, 20449-20465.
- CAIRNS, A. B., THOMPSON, A. L., TUCKER, M. G., HAINES, J. & GOODWIN, A. L. 2012. Rational Design of Materials with Extreme Negative Compressibility: Selective Soft-Mode Frustration in $\text{KMn}[\text{Ag}(\text{CN})_2]_3$. *Journal of the American Chemical Society*, 134, 4454-4456.
- CHAN, N. & EVANS, K. E. 1997. Fabrication methods for auxetic foams. *Journal of Materials Science*, 32, 5945-5953.
- CHAN, O., CHEN, F., CHOY, C. & WARD, I. 1978. The elastic constants of extruded polypropylene and polyethylene terephthalate. *Journal of Physics D: Applied Physics*, 11, 617.
- CHOI, J. B. & LAKES, R. S. 1995. Nonlinear Analysis of the Poisson's Ratio of Negative Poisson's Ratio Foams. *Journal of Composite Materials*, 29, 113-128.
- CLIFFORD, B. 2016. Available: www.turningtools.co.uk.
- COLUCI, V. R., HALL, L. J., KOZLOV, M. E., ZHANG, M., DANTAS, S. O., GALVÃO, D. S. & BAUGHMAN, R. H. 2008. Modeling the auxetic transition for carbon nanotube sheets. *Physical Review B*, 78, 115408.
- COUDERT, F.-X. 2013. Systematic investigation of the mechanical properties of pure silica zeolites: stiffness, anisotropy, and negative linear compressibility. *Physical Chemistry Chemical Physics*, 15, 16012-16018.

- COUDERT, F.-X. & FUCHS, A. H. 2016. Computational characterization and prediction of metal–organic framework properties. *Coordination Chemistry Reviews*, 307, Part 2, 211-236.
- DASSAULT 2009. ABAQUS. DASSAULT.
- DAVIS, M. E. & LOBO, R. F. 1992. Zeolite and molecular sieve synthesis. *Chemistry of Materials*, 4, 756-768.
- DIMITROV, D., KLUSHIN, L., SKVORTSOV, A., MILCHEV, A. & BINDER, K. 2009. The escape transition of a polymer: A unique case of non-equivalence between statistical ensembles. *The European Physical Journal E*, 29, 9-25.
- DUYKER, S. G., PETERSON, V. K., KEARLEY, G. J., STUDER, A. J. & KEPERT, C. J. 2016. Extreme compressibility in LnFe (CN) 6 coordination framework materials via molecular gears and torsion springs. *Nature chemistry*.
- EARMON, R. F. S. 1948. *The elasticity of wood and plywood*, London, HM Stationery Office.
- EVANS, K. & ALDERSON, A. 2000. Auxetic materials: functional materials and structures from lateral thinking! *Advanced Materials*, 617-628.
- EVANS, K. E. & CADDOCK, B. D. 1989. Microporous materials with negative Poisson's ratios. II. Mechanisms and interpretation. *Journal of Physics D: Applied Physics*, 22, 1883.
- EVERY, A. G. & MCCURDY, A. K. 1993. Group III: Crystal and Solid State Physics. *Landolt-Börnstein Tables*, 29.
- FORMOSA, J. P., CAUCHI, R. & GRIMA, J. N. 2015. Carbon allotropes exhibiting negative linear compressibility. *physica status solidi (b)*, 252, 1656-1663.
- FORTES, A. D., SUARD, E. & KNIGHT, K. S. 2011. Negative Linear Compressibility and Massive Anisotropic Thermal Expansion in Methanol Monohydrate. *Science*, 331, 742-746.
- GAGNON, K. J., BEAVERS, C. M. & CLEARFIELD, A. 2013. MOFs Under Pressure: The Reversible Compression of a Single Crystal. *Journal of the American Chemical Society*, 135, 1252-1255.
- GATT, R., ATTARD, D. & GRIMA, J. N. 2009. On the behaviour of bi-material strips when subjected to changes in external hydrostatic pressure. *Scripta Materialia*, 60, 65-67.

- GATT, R. & GRIMA, J. N. 2008. Negative compressibility. *physica status solidi (RRL) – Rapid Research Letters*, 2, 236-238.
- GERE & TIMOSHENKO 1996. *Mechanics of Materials*, Nelson Engineering.
- GHOSH, A. K. & KUMAR, M. R. 1997. Dynamic analysis of supporting structure of mobile antenna. *Computers & Structures*, 63, 633-637.
- GIBSON & ASHBY 1999. *Cellular Solids: Structures and Properties*, Cambridge, Cambridge University Press.
- GOODWIN, A. L., KEEN, D. A. & TUCKER, M. G. 2008. Large negative linear compressibility of Ag₃[Co(CN)₆]. *Proceedings of the National Academy of Sciences*, 105, 18708-18713.
- GREGORY, A. R. 1976. FLUID SATURATION EFFECTS ON DYNAMIC ELASTIC PROPERTIES OF SEDIMENTARY ROCKS. *GEOPHYSICS*, 41, 895-921.
- GRIMA, J. & EVANS, K. 2000. Auxetic behavior from rotating squares. *Journal of Materials Science Letters*, 19, 1563-1565.
- GRIMA J.N ATTARD D., G. R. 2008. Truss-type systems exhibiting negative compressibility. *phys stat sol(b)*, 245.
- GRIMA, J. N. & EVANS, K. E. 2006. Auxetic behavior from rotating triangles. *Journal of materials science*, 41, 3193-3196.
- GRIMA, J. N., GATT, R. & FARRUGIA, P. S. 2008. On the properties of auxetic meta-tetrachiral structures. *physica status solidi (b)*, 245, 511-520.
- GUITARD, D. 1987. *Mécanique du matériau bois et composites*, Cépaduès.
- HALL, L. J., COLUCI, V. R., GALVÃO, D. S., KOZLOV, M. E., ZHANG, M., DANTAS, S. O. & BAUGHMAN, R. H. 2008. Sign Change of Poisson's Ratio for Carbon Nanotube Sheets. *Science*, 320, 504-507.
- HODGSON, S. A., ADAMSON, J., HUNT, S. J., CLIFFE, M. J., CAIRNS, A. B., THOMPSON, A. L., TUCKER, M. G., FUNNELL, N. P. & GOODWIN, A. L. 2014. Negative area compressibility in silver (I) tricyanomethanide. *Chemical Communications*, 50, 5264-5266.

- HORRIGAN, E. J., SMITH, C. W., SCARPA, F. L., GASPAR, N., JAVADI, A. A., BERGER, M. A. & EVANS, K. E. 2009. Simulated optimisation of disordered structures with negative Poisson's ratios. *Mechanics of Materials*, 41, 919-927.
- HOWELL, B., PRENDERGAST, P. & HANSEN, L. 1994. Examination of acoustic behavior of negative poisson's ratio materials. *Applied Acoustics*, 43, 141-148.
- HSUEH H.C., L. C. C., WANK C.W. 2000. Compression mechanisms in the anisotropically bonded elements Se and Te. *Physical Review B*, 61.
- HUGHES, T., MARMIER, A. & EVANS, K. 2010. Auxetic frameworks inspired by cubic crystals. *International Journal of Solids and Structures*, 47, 1469-1476.
- JAMIESON, J. & MCWHAN, D. 1965. Crystal structure of tellurium at high pressures. *The Journal of Chemical Physics*, 43, 1149-1152.
- JU, J. & SUMMERS, J. D. 2011. Compliant hexagonal periodic lattice structures having both high shear strength and high shear strain. *Materials & Design*, 32, 512-524.
- KANG, L., JIANG, X., LUO, S., GONG, P., LI, W., WU, X., LI, Y., LI, X., CHEN, C. & LIN, Z. 2015. Negative linear compressibility in a crystal of α -BiB₃O₆. *Scientific reports*, 5.
- KIER, W, S. K. 1985. Tongues, Tentacles and Trunks; the biomechanics of movement in muscular-hydrostats. *Zoological Journal of the Linnean Society*, 83, 307-324.
- LAKES, R. 1987. Foam Structures with a Negative Poisson's Ratio. *Science*, 235, 1038-1040.
- LAKES, R. 2007. Cellular solids with tunable positive or negative thermal expansion of unbounded magnitude. *Applied physics letters*, 90, 221905.
- LAKES, R. S. & DRUGAN, W. J. 2002. Dramatically stiffer elastic composite materials due to a negative stiffness phase? *Journal of the Mechanics and Physics of Solids*, 50, 979-1009.
- LAKES, R. S. & ELMS, K. 1993. Indentability of Conventional and Negative Poisson's Ratio Foams. *Journal of Composite Materials*, 27, 1193-1202.
- LAKES, R. S. & WITT, R. 2002. Making and Characterizing Negative Poisson's Ratio Materials. *International Journal of Mechanical Engineering Education*, 30, 50-58.

- LEE, J., CHOI, J. B. & CHOI, K. 1996. Application of homogenization FEM analysis to regular and re-entrant honeycomb structures. *Journal of Materials Science*, 31, 4105-4110.
- LEE, Y., VOGT, T., HRILJAC, J. A., PARISE, J. B. & ARTIOLI, G. 2002. Pressure-Induced Volume Expansion of Zeolites in the Natrolite Family. *Journal of the American Chemical Society*, 124, 5466-5475.
- LIFSHITZ, I. 1952. Thermal properties of chain and layered structures at low temperatures. *Zh. Eksp. Teor. Fiz*, 22, 475-486.
- LOA, I., SYASSEN, K. & KREMER, R. 1999. Vibrational properties of NaV₂O₅ under high pressure studied by Raman spectroscopy. *Solid state communications*, 112, 681-685.
- LOVE, A. E. H. 1944. *A Treatise on the Mathematical Theory of Elasticity*, Dover.
- MACDONALD, A. G. & FRASER, P. J. 1999. The transduction of very small hydrostatic pressures. *Comparative Biochemistry and Physiology Part A: Molecular & Integrative Physiology*, 122, 13-36.
- MAGOS-PALASYUK, E., FIJALKOWSKI, K. J. & PALASYUK, T. 2016. Chemically driven negative linear compressibility in sodium amidoborane, Na(NH₂BH₃). *Scientific Reports*, 6.
- MANN, R. W., BAUM, G. A. & HABEGER JR, C. C. 1979. Determination of all nine orthotropic elastic constants for machine-made paper.
- MARIATHASAN, J., FINGER, L. & HAZEN, R. 1985. High-pressure behavior of LaNbO₄. *Acta Crystallographica Section B: Structural Science*, 41, 179-184.
- MARMIER, A., LETHBRIDGE, Z. A., WALTON, R. I., SMITH, C. W., PARKER, S. C. & EVANS, K. E. 2010a. EIAM: A computer program for the analysis and representation of anisotropic elastic properties. *Computer Physics Communications*, 181, 2102-2115.
- MARMIER, A., NTOAHAE, P. S., NGOEPE, P. E., PETTIFOR, D. G. & PARKER, S. C. 2010b. Negative compressibility in platinum sulfide using density-functional theory. *Physical Review B*, 81, 172102.

- MCCANN, D. & CARTZ, L. 1972. Bond distances and chain angle of hexagonal selenium at high pressure. *Journal of Applied Physics*, 43, 4473-4477.
- MCCANN, D., CARTZ, L., SCHMUNK, R. & HARKER, Y. 1972. Compressibility of Hexagonal Selenium by X-Ray and Neutron Diffraction. *Journal of Applied Physics*, 43, 1432-1436.
- MILLER, W., EVANS, K. E. & MARMIER, A. 2015. Negative linear compressibility in common materials. *Applied Physics Letters*, 106, 231903.
- MUNN, R. 1972. Role of the elastic constants in negative thermal expansion of axial solids. *Journal of Physics C: Solid State Physics*, 5, 535.
- NAKAO, H., OHWADA, K., TAKESUE, N., FUJII, Y., ISOBE, M., UEDA, Y., SAWA, H., KAWADA, H., MURAKAMI, Y. & DAVID, W. 1997. Lattice dimerization and strain in inorganic spin-Peierls compound NaV₂O₅. *Physica B: Condensed Matter*, 241, 534-536.
- NYE 1964. *Physical Properties of Crystals* Oxford, Oxford University Press
- NYE 1985. *Physical Properties of Crystals: Their Representation by Tensors and Matrices*, Oxford University Press.
- O'REILLY, J. C., RITTER, D. A. & CARRIER, D. R. 1997. Hydrostatic locomotion in a limbless tetrapod. *Nature*, 386, 269-272.
- ORTIZ, A. L. U., BOUTIN, A., GAGNON, K. J., CLEARFIELD, A. & COUDERT, F. O.-X. 2014. Remarkable Pressure Responses of Metal–Organic Frameworks: Proton Transfer and Linker Coiling in Zinc Alkyl Gates. *Journal of the American Chemical Society*, 136, 11540-11545.
- ORTIZ, A. U., BOUTIN, A., FUCHS, A. H. & COUDERT, F.-X. 2012. Anisotropic Elastic Properties of Flexible Metal-Organic Frameworks: How Soft are Soft Porous Crystals? *Physical review letters*, 109, 195502.
- ORTIZ, A. U., BOUTIN, A., FUCHS, A. H. & COUDERT, F.-X. 2013. Metal–organic frameworks with wine-rack motif: What determines their flexibility and elastic properties? *The Journal of chemical physics*, 138, 174703.
- PDQ LIFTING, L. 2015. Available: www.pdqlifting.co.uk.

- PRAWER, S., SMITH, T. & FINLAYSON, T. 1985. The room temperature elastic behaviour of CsH₂PO₄. *Australian Journal of Physics*, 38, 63-84.
- RAWSON, F. & RIDER, J. 1974. The elastic constants of oriented polyvinyl chloride. *Journal of Physics D: Applied Physics*, 7, 41.
- REN W., Y. J., SHI W., TANG Z., CHAN C.T., SHENG P 2009. Negative compressibility of Selenium chains confined in the channels of zeolite single crystals. *New Open journal of Physics*, 11.
- ROVATI, M. 2004. Directions of auxeticity for monoclinic crystals. *Scripta materialia*, 51, 1087-1091.
- ROYLANCE, D. 1996. Available: <http://web.mit.edu/course/3/3.11/www/modules/plate.html>.
- RYDER, M. R., CIVALLERI, B. & TAN, J.-C. 2016. Isoreticular zirconium-based metal-organic frameworks: discovering mechanical trends and elastic anomalies controlling chemical structure stability. *Physical Chemistry Chemical Physics*, 18, 9079-9087.
- SCARPA, F., CIFFO, L. G. & YATES, J. R. 2004. Dynamic properties of high structural integrity auxetic open cell foam. *Smart Materials and Structures*, 13, 49.
- SERRA-CRESPO, P., DIKHTIARENKO, A., STAVITSKI, E., JUAN-ALCAÑIZ, J., KAPTEIJN, F., COUDERT, F.-X. & GASCON, J. 2015. Experimental Evidence of Negative Linear Compressibility in the MIL-53 Metal-Organic Framework Family. *CrystEngComm / RSC*, 17, 276-280.
- SEYIDOV, M. Y. & SULEYMANOV, R. A. 2010. Negative thermal expansion due to negative area compressibility in TlGaSe₂ semiconductor with layered crystalline structure. *Journal of Applied Physics*, 108, 063540.
- SKELTON E.F., F. J. L. 1976. Study of the pressure induced phase transition in paratellurite. *Physical Review B*, Vol 13.
- SKVORTSOV A.M., K. L. I., LEERMAKER F.A.M. 2007. Negative compressibility and nonequivalence of two statistical ensembles in the escape transition of a polymer chain. *The Journal of chemical Physics*, 126.
- STRAUMANIS, M. 1949. The precision determination of lattice constants by the powder and rotating crystal methods and applications. *Journal of Applied Physics*, 20, 726-734.

- TAN, J. C. & CHEETHAM, A. K. 2011. Mechanical properties of hybrid inorganic–organic framework materials: establishing fundamental structure–property relationships. *Chemical Society Reviews*, 40, 1059-1080.
- TIMOSHENKO & GOODIER 1970. *Theory of Elasticity*, McGraw-Hill.
- TING, T. C. T. & CHEN, T. 2005. Poisson's ratio for anisotropic elastic materials can have no bounds. *The Quarterly Journal of Mechanics and Applied Mathematics*, 58, 73-82.
- UHOYA, W., TSOI, G., VOHRA, Y. K., MCGUIRE, M. A., SEFAT, A. S., SALES, B. C., MANDRUS, D. & WEIR, S. T. 2010. Anomalous compressibility effects and superconductivity of EuFe_2As_2 under high pressures. *Journal of Physics: Condensed Matter*, 22, 292202.
- VERONDA, D. & WESTMANN, R. 1970. Mechanical characterization of skin—finite deformations. *Journal of biomechanics*, 3, 111-124.
- WENG, C., WANG, K. & CHEN, T. Design of microstructures and structures with negative linear compressibility in certain directions. *Advanced Materials Research*, 2008. Trans Tech Publ, 807-814.
- WHITE, S. H. & KING, G. I. 1985. Molecular packing and area compressibility of lipid bilayers. *Proceedings of the National Academy of Sciences*, 82, 6532-6536.
- WILLIAMS, J. & LEWIS, J. 1982. Properties and an anisotropic model of cancellous bone from the proximal tibial epiphysis. *Journal of Biomechanical Engineering*, 104, 50-56.
- ZHOU, W., WU, H., YILDIRIM, T., SIMPSON, J. R. & WALKER, A. H. 2008. Origin of the exceptional negative thermal expansion in metal-organic framework-5 $\text{Zn}_4\text{O}(\text{1,4-benzenedicarboxylate})_3$. *Physical Review B*, 78, 054114.